$$F_{AR} = \cos\left(\frac{\varphi}{2}\right) \cdot \left(1 - \sin\left(\frac{\varphi}{2}\right)\right) \tag{7}$$

where the angle φ is defined in Figure 2.

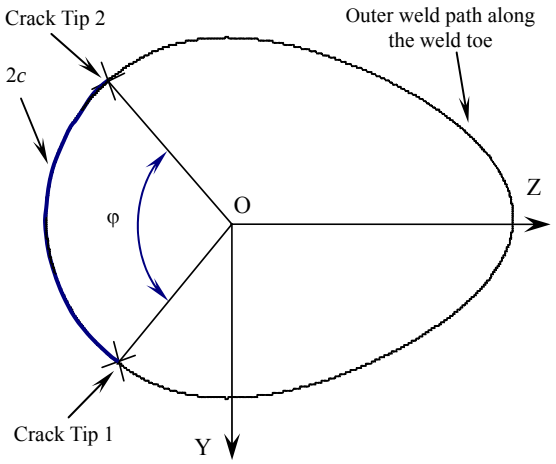

Figure 2. Definition of the Angle φ Used in Equation 7

In Annex B of BS7910 [1], the L_r parameter for any tubular joint subjected under combined loads is given by the following equation:

$$L_r = \left(\frac{\sigma_F}{\sigma_Y}\right)\left\{\left|\frac{P_a}{P_c}\right| + \left(\frac{M_{ai}}{M_{ci}}\right)^2 + \left(\frac{M_{ao}}{M_{co}}\right)\right\} \tag{8}$$

where σ_F and σ_Y are the flow and yield stresses; P_a, M_{ai} and M_{ao} are the applied axial load, in-plane bending and out-of-plane bending; and P_c, M_{ci} and M_{co} are the plastic collapse load in the cracked condition for axial load, in-plane bending and out-of-plane bending respectively. The plastic collapse load is obtained by reducing the plastic collapse load of the corresponding uncracked geometry on the basis of the net load-bearing area for axial load and the effect of the flaw area on the plastic collapse modulus for bending moments.

3. FRACTURE ASSESSMENT OF A CRACKED k-JOINT

3.1 Specimen Dimensions

A full-scale cracked tubular K-joint shown in Figure 3 containing fatigue cracks will be assessed in this paper. In the fatigue test carried out earlier (Lie et al. [11]), an axial (AX) and an in-plane bending (IPB) were applied at the brace end. As the hot spot stress was located at the crown of the chord, and the applied loads were symmetrical, the crack was found to initiate and propagate symmetrically from this position.

The notations used to describe the joint parameters, namely $\alpha = 2L/D$, $\beta = d/D$, $\gamma = D/2T$, $\tau = t/T$ and $2\varsigma = g/D$ are given in Figure 4, and the overall dimensions are tabulated in Table 1.

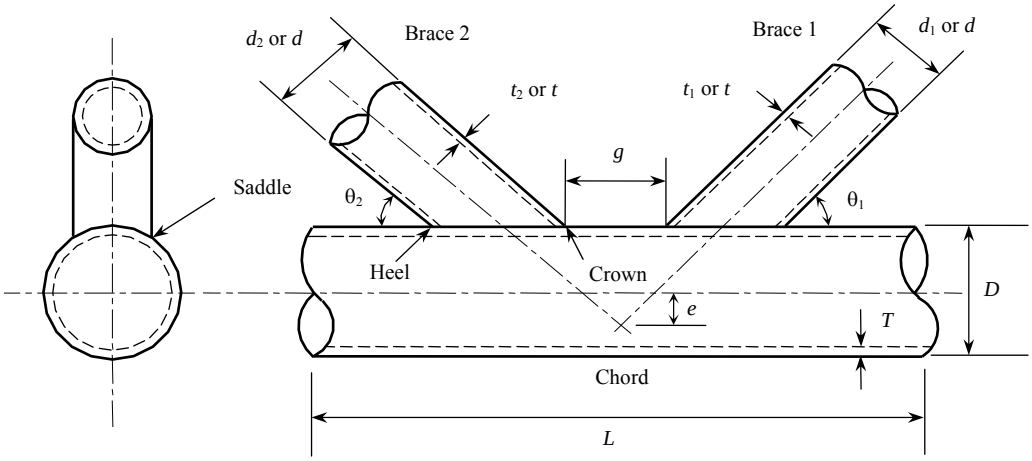

Figure 4. Parameters of the K-joint Specimen

Table 1. Overall Dimensions of the K-joint Specimen

Specimen	D (mm)	d (mm)	T (mm)	t (mm)	g (mm)	θ_1, θ_2	L (mm)	α	β	γ	ς
K-joint	273.1	141.3	25.4	19.1	102	45°	5395.82	39.52	0.52	5.38	0.37

To capture the crack details during the earlier test (Lie et al., [11]), an alternating current potential drop (ACPD) technique shown in Figure 5 was used in the fatigue test (Dover et al. [12]). The results showed that the captured crack profile by the ACPD technique agreed quite well with the actual crack shape. It is especially so at the deepest points where the ACPD measurements are capable of providing accurate and useful information such as the stress intensity factors. The measured crack depth a and the corresponding crack length $2c$ are tabulated in Tables 2 and 3 respectively.

Figure 5. ACPD Test Set-up and Location of the Crack

The crack shapes at different propagation stages were plotted from the ACPD readings, and they were compared with the actual crack shape measured by manual method. The two types of crack shapes were then compared with a semi-elliptical shape having the same depth and length (Figure 6). From the earlier fatigue test (Lie et al. [11]), it can be seen that it is reasonable to assume a semi-elliptical crack shape in the numerical model.

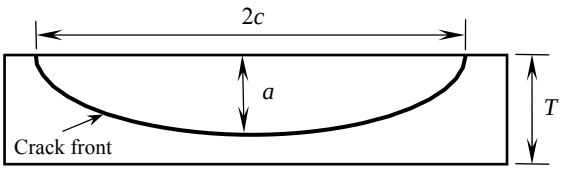

Figure 6. Semi-elliptical 3D Surface Crack

3.2 Mesh Generation of Cracked K-joint

To generate the mesh of the completed tubular K-joint model with a surface crack which can be located at any position with any length and depth, five types of elements are used in the present mesh generation procedure. Quarter-point crack tip elements are used along the crack front to simulate the displacements singularity. For these elements, the mid-side nodes are moved to the quarter point for the edge connected to the crack front. Prism elements are employed to model the transition zone between the region near the crack surface and the far field region. Tetrahedral elements are used to link the quarter-point crack tip elements and other types of elements which enclose the crack front. Pyramid elements are used to connect the prism elements with tetrahedral elements around the crack front. In the fields far away from the crack, hexahedral elements are used to model the remaining part of the members. The locations of these different types of elements are illustrated in Figure 7.

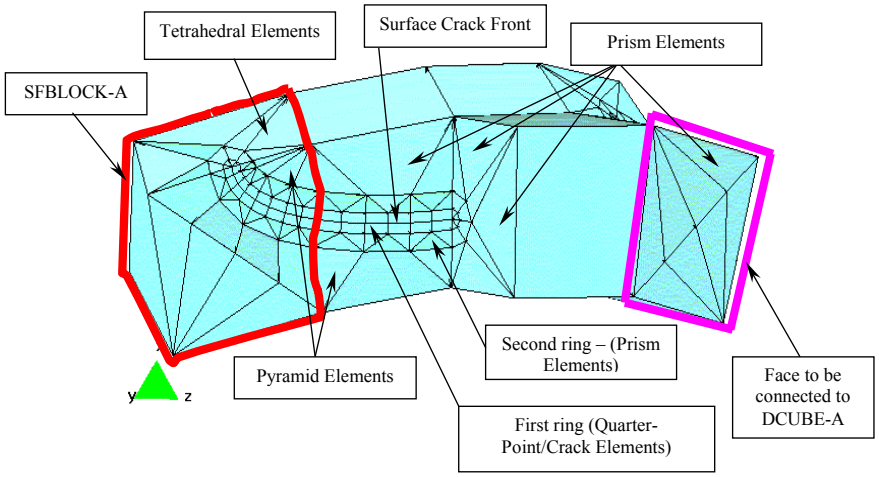

Figure 7. Detailed Mesh Along the Crack Front

In the mesh generation, all the zones are classified into three main types: refined (Zone CF, Zone CF1 and Zone CRBLOCK), coarse zones (Zone A, Zone ER, Zone EL, EXTENCHL, EXTENCHR and Zone H) and transition zones (Zone B, Zone D, Zone G1 and Zone G2) as shown in Figure 8. In the zones with refined mesh, three layers of elements are generated in the thickness direction so as to model the crack depths. The mesh of the surface crack is extracted from Zone CF1. In the coarse mesh zones, only one layer of elements is generated in thickness direction. In the transition zones, Zone B connects Zone A and Zone CF or Zone CF1.

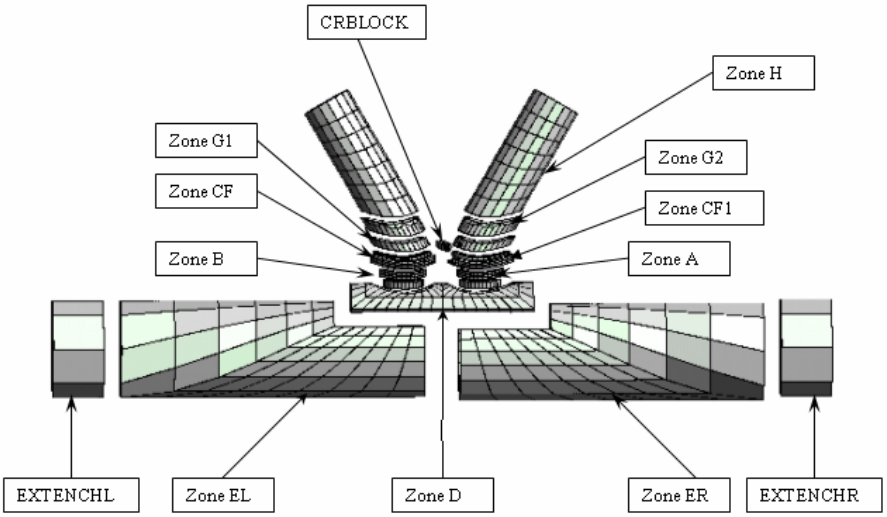

Figure 8. Mesh Generation of the Tubular K-joint

Figure 9 shows the mesh of CRBLOCK in a detailed view. CRBLOCK is extracted from Zone CF1. It should be emphasized that the number and location of elements extracted from Zone CF1 will depend on the crack length and position. Once the crack length and the crack position are determined, the number of elements to be extracted will be calculated automatically. Therefore, a surface crack with any length at any fixed position can be generated automatically.

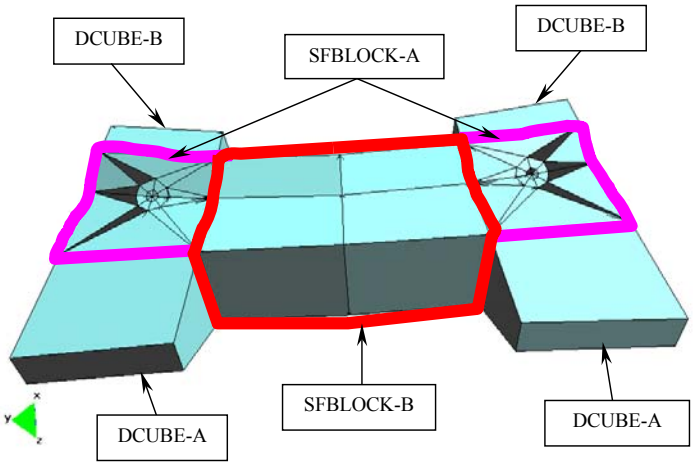

Figure 9. CRBLOCK Extracted from Zone CF1 and Zone D

After extracting CRBLOCK from Zone CF1, all the elements used in Zone CF1 are hexahedral elements since no crack in this zone. The mesh in details of Zone CF1 after extracting CRBLOCK is shown in Figure 10.

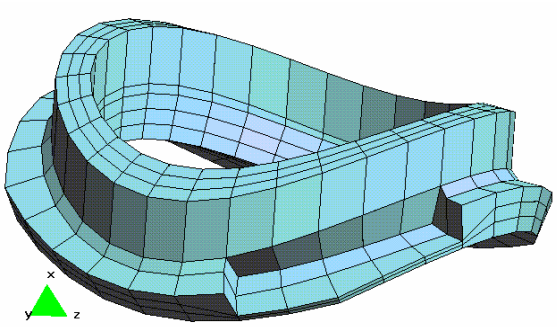

Figure 10. Mesh of Zone CF1 After Extracting CRBLOCK

After the mesh of all the zones has been completed, they are then merged together to form the mesh of the entire structure. Figure 11 shows the mesh of a K-joint after merging the mesh of all the zones.

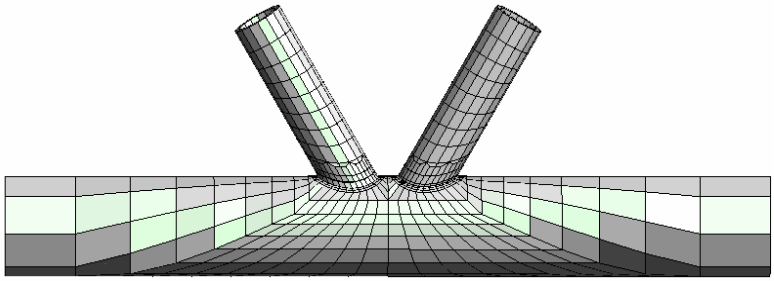

Figure 11. Mesh of Tubular K-joint After Merging All the Zones

According to the joint dimensions and the 3D crack size, a finite element model shown in Figure 12 is generated automatically (Lie at al. [7]) to calculate the stress intensity factors at the critical locations, namely, at the deepest point and at the crack tips. The K-joint specimen is subjected with an axial load (AX) of 150 kN and an in-plane bending (IPB) of 38 kNm (13.5 kN × 2.815 m) respectively.

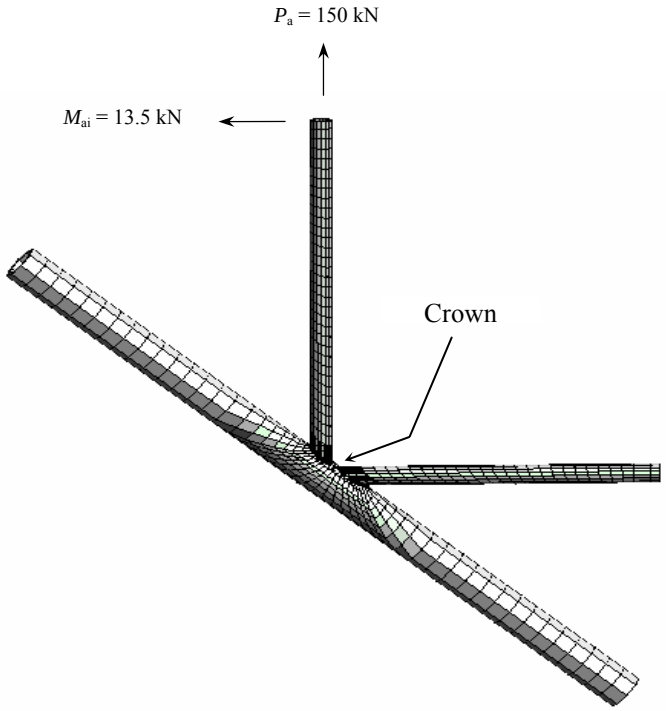

Figure 12. Finite Element Mesh and Loading Conditions

3.3 Stress Intensity Factors

To estimate the remaining life of tubular K-joints, the fracture parameter called the stress intensity factor (SIF) is frequently used by many researchers. There are several methods which can be used to evaluate this fracture parameter. In practice, the two most commonly used methods are the *J*-integral and the displacement extrapolation. The *J*-integral has been found to be insensitive to mesh refinement, but it can not be used directly in the mixed mode problems. However, the Mode-I, II & III SIFs can still be obtained from the *J*-integral using an indirect way by introducing an interaction integral method (Shih and Asaro [13]). It is also noted that *J*-integral lacks path independence in the region where the crack meets the weld toe because the stress at the toe and the crack tip is singular. On the other hand, displacement extrapolation method is based on Westergaard's equations which relate the displacements in the vicinity of the crack front to the stress intensity factors. This method is not applicable for inelastic behaviour.

3.3.1 J-integral method

J-integral method is then used to obtain the stress intensity factors along the crack front and at the two crack tips. Although this method can not be used directly for the mixed mode problems, it can still be able to produce the Mode-I, II & III stress intensity factors through an indirect way by introducing an interaction integral method as proposed by Shih and Asaro [13]. The relationship between the *J*-integral and the SIFs can be written as

$$\mathbf{J} = \frac{1}{8\pi}\mathbf{K}^{\mathbf{T}} \cdot \mathbf{B} \cdot \mathbf{K} \tag{9}$$

where $\mathbf{K} = [K_{\mathrm{I}}, K_{\mathrm{II}}, K_{\mathrm{III}}]^{\mathbf{T}}$ and $\mathbf{B}$ is called the pre-logarithmic energy factor matrix.

Shih and Asaro [13] gave the relationship between the SIF and the interaction *J*-integral, $\mathbf{J}_{\mathrm{int}}$, as follow:

$$\mathbf{K} = 4\,\pi\,\mathbf{B} \cdot \mathbf{J}_{\mathbf{int}} \tag{10}$$

where $\mathbf{J}_{\mathrm{int}} = [J_{\mathrm{int}}^{\mathrm{I}}, J_{\mathrm{int}}^{\mathrm{II}}, J_{\mathrm{int}}^{\mathrm{III}}]^{\mathbf{T}}$.

Therefore, once $\mathbf{J}_{\mathrm{int}}$ is obtained, $\mathbf{K}$ can be easily calculated from Eq. 10. The detailed calculations of $\mathbf{J}_{\mathrm{int}}$ can be found in the paper published by Shih and Asaro [13], and this method has been implemented in the ABAQUS [14] general finite element software. The values of Mode-I stress intensity factors K_{I} corresponding to the crack depth *a* and crack length 2*c* at the deepest point and the crack tips are tabulated in Tables 2 and 3 respectively.

4. ASSESSMENT POINTS OF K_{r} AND L_{r}

In order to assess the safety and integrity of this cracked tubular K-joint subjected under the combined loads, BS7910 [1] Level 2A failure assessment diagram (FAD) method is employed in this study. FADs are used to consider failure by linear elastic fractures as one limiting criteria and failure by plastic collapse as the second criteria. When performing a structural integrity assessment of a flaw in a stressed structure, an assessment point is derived from two different calculations and

REFERENCES

[1] BS7910, "Guide to Methods for Assessing the Acceptability of Flaws in Fusion Welded Structures", British Standards Institution, London, UK, 2005.

[2] API RP579, "Fitness-for-Service", American Petroleum Institute, Washington, USA, 2000.

[3] CEGB R6, "Assessment of the Integrity of Structures Containing Defects", Revision 4, British Energy, Gloucester, UK, 2001.

[4] Dowling, A.B. and Townley, C.H.A., "The Effect of Defect on Structural Failure: A Two-Criteria Approach", International Journal of Pressure Vessels and Piping, 1975, Vol. 3, No. 2, pp. 77-107.

[5] Wiesner, C.S., Maddox, S.J., Xu, W., Webster, G.A., Burdekin, F.M., Andrews, R.M. and Harrison, J.D., "Engineering Critical Analyses to BS7910 – the UK Guide on Methods for Assessing the Acceptability of Flaws in Metallic Structures", International Journal of Pressure Vessels and Piping, 2000, Vol. 77, No. 14-15, pp. 883-893.

[6] Dawes, M.G. and Denys, R., "BS 5500 Appendix D: An Assessment Based on Wide Plate Brittle Fracture Test Data", International Journal of Pressure Vessels and Pipings, 1984, Vol. 15, pp. 161-192.

[7] Lie, S.T., Lee, C.K., Chiew S.P. and Shao, Y.B., "Mesh Modelling and Analysis of Cracked Uni-planar Tubular K-joints", Journal of Constructional Steel Research, 2005, Vol. 61, No. 2, pp. 235-264.

[8] BS7448-1, "Fracture Mechanics Toughness Tests – Part 1: Method for Determination of K_{IC}, Critical CTOD and Critical J Values of Metallic Structures", British Standards Institution, London, UK, 1991.

[9] Lie, S.T., Lee, C.K., Chiew, S.P. and Shao, Y.B., "Estimation of Stress Intensity Factors of Weld Toe Surface Cracks in Tubular K-joints", Proceedings of the 10th International Symposium on Tubular Structures, Madrid, Spain, 2003, pp. 347-355.

[10] Health and Safety Executive (HSE), "Offshore Installation: Guidance on Design, Construction and Certification", 4th Edition, Third Amendment, Her Majesty's Stationary Office, London, UK, 1995.

[11] Lie S.T., Chiew S.P., Lee C.K. and Shao, Y.B., "Validation of a Surface Crack Stress Intensity Factors of a Tubular K-joint", International Journal of Pressure Vessels and Piping, 2005, Vol. 82, No. 8, pp. 610-617.

[12] Dover, W.D., Dharmavasan, S., Brennan, F.P. and Marsh, K.J., "Fatigue Crack Growth in Offshore Structures", Engineering Materials Advisory Services (EMAS) Ltd., Chameleon Press, London, UK, 1995.

[13] Shih, C.F. and Asaro, R.J., "Elastic –Plastic Analysis of Cracks on Bimaterial Interface: Part I-Small Scale Yielding", Journal of Applied Mechanics, ASME, 1998, Vol. 51, pp. 299-316.

[14] ABAQUS, "User's Manual", Version 6.5, Hibbit, Karlsson and Sorensen Inc., Providence, USA, 2005.

[15] Somerday, B.P., "Technical Reference on Hydrogen Compatibility of Materials – Carbon Steel: C-Mn Alloys (Code 1100)", Sandia National Laboratory, Livermore, California, USA, 2007.

THE STUDY ON SEMIRIGID JOINT OF STEEL-CONCRETE COMPOSITE BEAM TO CFST COLUMN

Zhan Wang [1,*] , Jianrong Pan[1] and Jixong Yuan[2]

[1] *State Key Laboratory of Subtropical Building Science, South China University of Technology, Guangzhou, China*
[2] *Department of Civil Engineering, Shantou University, Shantou, China*
**(Corresponding author: E-mail: wangzhan@scut.edu.cn)*

Received: 21 March 2008; Revised: 18 July 2008; Accepted: 29 July 2008

ABSTRACT: The paper focused on the study on semirigid joint of steel-concrete composite beam to CFST column with stiffening ring. Two specimens were tested by incremental loading and cyclic loading. The finite element package ABAQUS was used to study the nonlinear behavior of such specimens. Shell elements were used to simulate the behavior of steel girder and steel tube. Continuum elements were used to simulate the behavior of concrete slab. The model was validated by comparing the computed values with experimental results. Based on the model, some factors, such as the dimensions of beam and column, were verified to influence on semirigid composite joint. A $M-\theta_r$ model for the composite joint was proposed.

Keywords: Finite element method, ABAQUS, semirigid joints, CFST column, Steel-concrete composite beam

1. INTRODUCTION

In the recent years, CFST (concrete-filled steel tubular) structures have been popularly applied in civil engineering. Because of the special formation of CFST column, the study on beam to column joint in high and high-rise building construction has been carried out all over the world.

The subject is a sub-item of the project, which is the study on restraining stiffness of joints of CFST frame. The previous researchers have done a lot of study on the project. Joint of steel beam to CFST column with stiffening ring, continuous web plate joint of steel beam to CFST column, and joint of steel beam to CFST column in frame structure have been researched. Some conclusions have been attained.

The first research was the stiffness of joint of steel beam to CFST column with stiffening ring. Chen et al. [1] used the finite element package ANSYS, created and analyzed the solid model of the joints, manufactured seven joints with stiffening ring to process joint test, and then verified the applicability of the finite element models with the experimental results. Base on the models, changed its dimension to confirm each factor influence on joint stiffness and created the joint's $M-\theta_r$ model, applied the joint's $M-\theta_r$ model to analyze the influence of both semirigid connection and joint stiffness on frame structure.

Wang et al. [2] made four continuous web plate joints of steel beam to CFST column. The joints were tested by using static test method. Experimental results showed the semirigid characteristic and transmutation state of connection areas of continuous web plate joint. Also the moment-rotation curve was gained.

Two CFST frames were tested by Chen and Wang [3]. The result was compared with the finite element analysis. The flexibility of connections and the rigid zones were considered in the member-bar model of the CFST frame.

The paper put forward a joint, which is steel-concrete composite beam to CFST column with stiffening ring. The specimens were tested by monotonic loading and cyclic loading. The finite element package ABAQUS [5] has been used to simulate the behavior of such specimens. The finite element model has been validated by comparing the computed values with available experimental results. The analysis of joint of steel-concrete composite beam to CFST column is useful to designer for predicting the behavior of composite joint.

2. FINITE ELEMENT ANALYSIS

2.1 Finite Element Model

A three-dimensional finite element model with the following characteristics had been used in the study:

(1) Concrete slab and the core concrete of CFST – modeled with continuum element C3D8R (8-node linear brick, reduced integration with hourglass control).

(2) Steel beam and steel tube – modeled with shell element S8R5 (8-node doubly curved thin shell, reduced integration, five degrees of freedom per node).

(3) Steel reinforcement – modeled with truss element T3D2 (2-node linear displacement) embedded in the concrete slab.

Full composite action between steel beam and concrete slab was assumed. This is based on the assumption that there is no slip at both ends between the concrete slab and steel girder. The shear connectors were omitted in the finite element analysis, tie constraints in ABAQUS [4] were used to attach concrete slab to steel flange. Surface-to-surface contact (ABAQUS/Standard) was used to simulate the contact between steel tube and concrete filled in the tube. A typical three-dimensional model used in the study is shown in Figure 1.

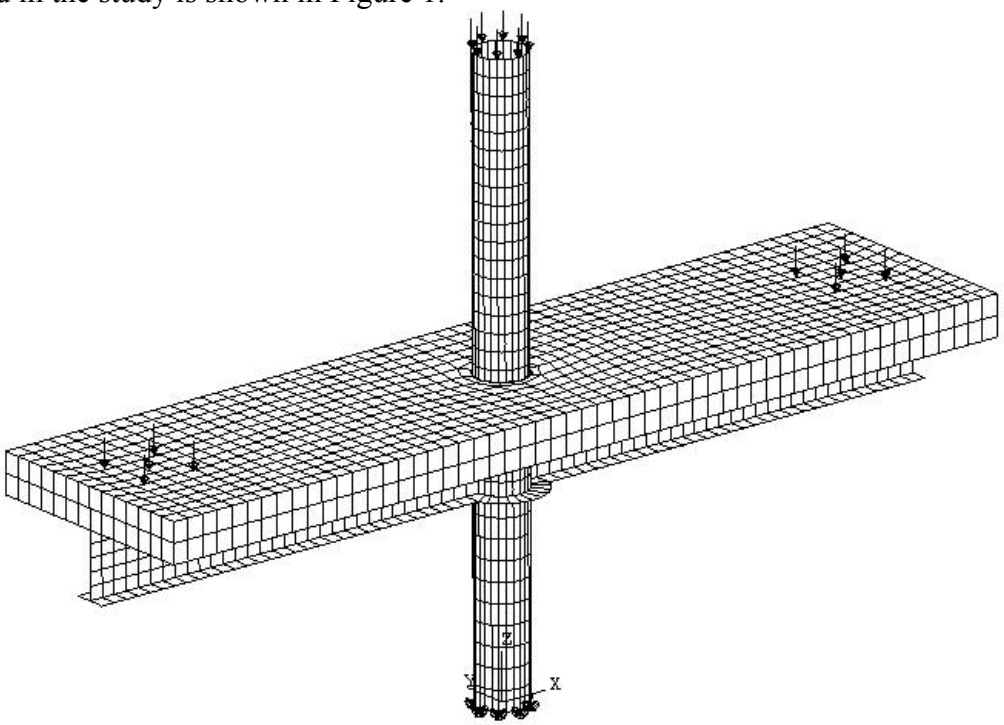

Figure 1. Finite Element Mesh

2.2 Material Modeling

Steel was assumed to behave as an elastic-plastic material with strain hardening in both tension and compression. Strain hardening had been modeled based on incremental plasticity theory. The idealized stress-strain curve used in the numerical analysis is shown in Figure 2. Material properties of steel are specified using the elastic-plastic with strain hardening options. For this purpose, ABAQUS [4] requires the input of the Young's modulus, E_s; Poisson's ratio, γ_s; yield stress, f_{sy}; and the ultimate stress, f_{su}, shown in Table 1.

Table 1. Parameters of Steel Material

Material		Yield strength (MPa)	Ultimate strength (MPa)	Young's modulus (MPa)	Poisson's ratio
Steel tube		350.0	460.0	2.06 E+5	0.30
Steel girder	Flange	270.0	370.0	2.06 E+5	0.30
	Web	290.0	390.0	2.06 E+5	

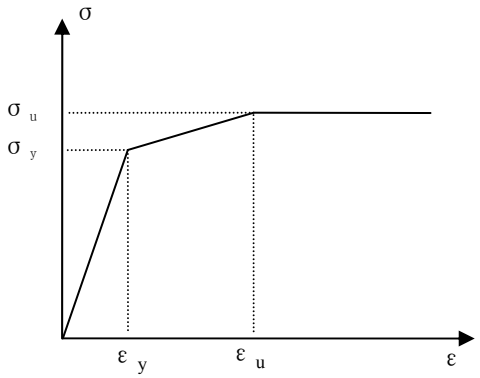

Figure 2. Stress-Strain Relationships for Steel

There are three concrete material models in ABAQUS [4]: concrete smeared cracking, cracking model for concrete, and concrete damaged plasticity. Among these models, the concrete damaged plasticity model is designed for applications with concrete subjected to monotonic and cyclic loadings and has good convergence characteristics. The concrete damaged plasticity was used to simulate concrete slab. The extended Drucker-Prager model was used to simulate the core concrete of CFST.

For concrete, the elastic properties are defined by the elastic option and its compressive stress-strain relationship outside the elastic range is specified using the concrete option. The values of Young's modulus, E_c; Poisson's ratio, γ_c; and the values of f_c for several values of ε_c and the corresponding values given by (ε-f_c/E_c) are required as input. The material properties of concrete are specified in Table 2.

Table 2. Parameters of Concrete Material

Material	Uniaxial ultimate compressive strength (MPa)	Uniaxial ultimate tensile strength (MPa)	Young's modulus (MPa)	Poisson's ratio
Concrete	25.50	2.32	3.20 E+4	0.20

2.3 Analysis of FEM Results

While solving equation, implicit solution (ABAQUS/Standard) was adopted. The initial and final load increments as well as the allowable minimum and maximum load increments are required in input file. The program iterates to reach the equilibrium condition for the initial load increment and all the subsequent increments automatically.

The ABAQUS analysis results include all stress and strain components, equivalent stress and total deformation. Through particular analysis, the details under loading were understood, and the information contributed to comprehend the mechanics behavior of joints. Analysis result of finite element offers guidance for design and measure of joint test.

3. THE EXPERIMENT OF JOINT

3.1 Design of Experiment

Two one-third scale joint specimens were manufactured according to Zhong [5]. The section of steel tube was Φ159×5, and the section of steel beam was HN200×100×5.5×8. The thickness of concrete slab was 120mm, and the width of concrete slab was 700mm. Longitudinal reinforcements were Φ12-120. Lateral reinforcements were Φ6-70. Shear connectors were Φ16×90, yield strength, 390MPa; ultimate strength, 440MPa. The cross-section of the composite beam is shown in Figure 3. The two specimens were tested by incremental loading and cyclic loading. Loading system is shown in Table 3, Figure 4, and Figure 5.

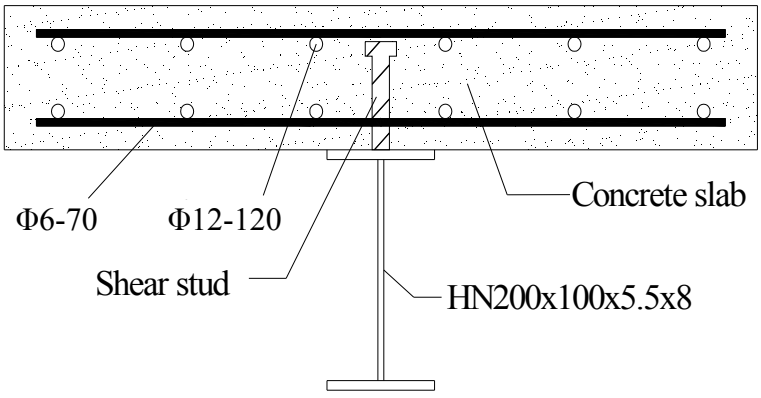

Figure 3. Cross-Section of Composite Beam

Table 3. Loading System

Number	CFST (kN)	Composite beam (kN)
HN200A	0→400	0→10→20→30→40→50→60→65→70→75→80→85→90→95
HN200B	0→400	0→20，0→40，0→60，0→80，0→95

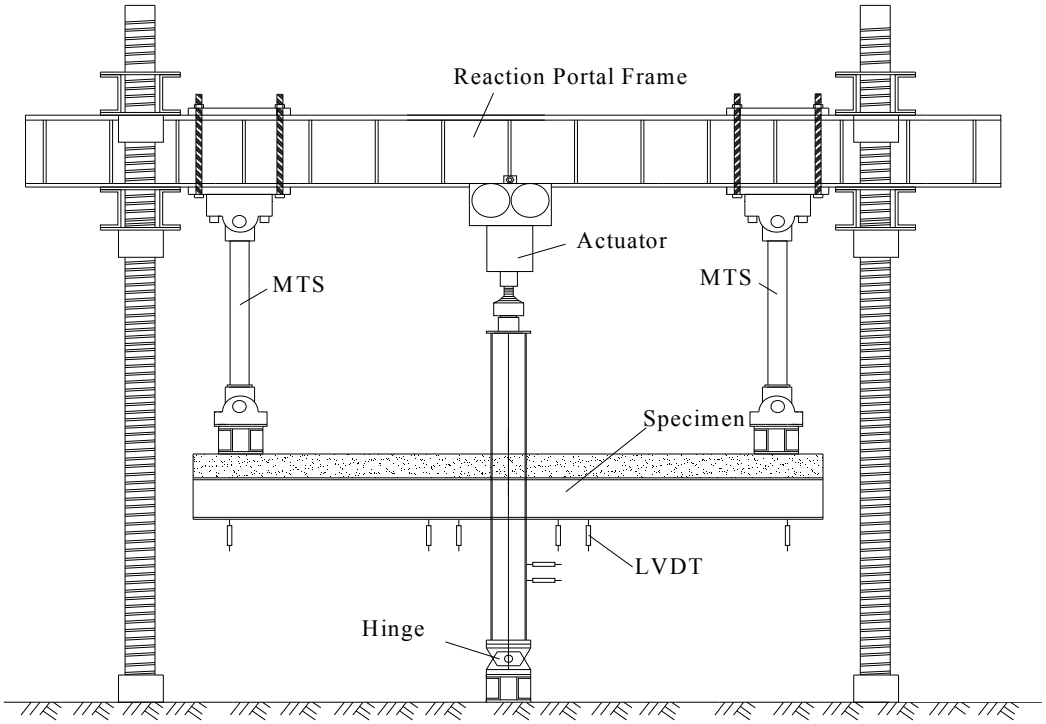

Figure 4. Sketch of Loading System

Figure 5. Specimen Loading

3.2 Analysis of Experiment Results

In area of negative moment of the joint, there was no obvious stress concentration in the top flange of steel beam. Elastic neutral axis and plastic neutral axis were close to top flange. The joint was damaged owing to the lower flange buckling firstly. The concrete slab was tensioned and cracked in the region about 300mm from the joint.

Load-strain curves of the steel beam section are shown in Figure 8. From zero point to 200mm (the height of steel beam) of the y-axis, strains of gauge 44#, 3#, 2#, 1#, 33# (see Figure 6) are specified. From the figures we can see that plane cross-section is acceptable in design of the joint. Figure 9 is load-strain of longitudinal rebar 20#, 19#, 7#, 8# and 9# (see Figure 7). At the same load value, the strain values of rebar 20#, 19#, 7#, 8# are increasing, while 9# is smaller. It may be due to that rebar end was weld end plate. The cyclic load-deflection curves of specimen HN200B are shown in Figure 10. Precise values of the specimen HN200B were not attained from experiments. However, all curves are approximately linear.

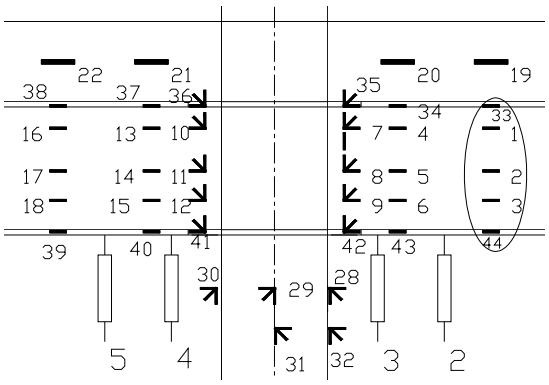

Figure 6. Gauges Layout of Joint

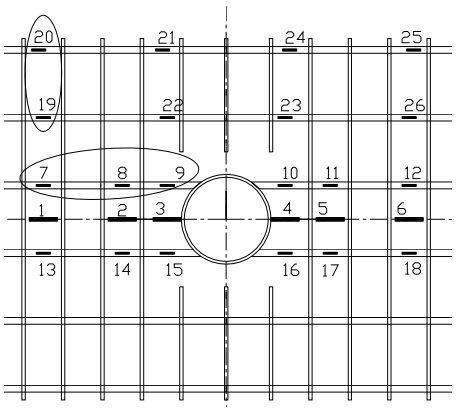

Figure 7. Gauges Layout of Rebar

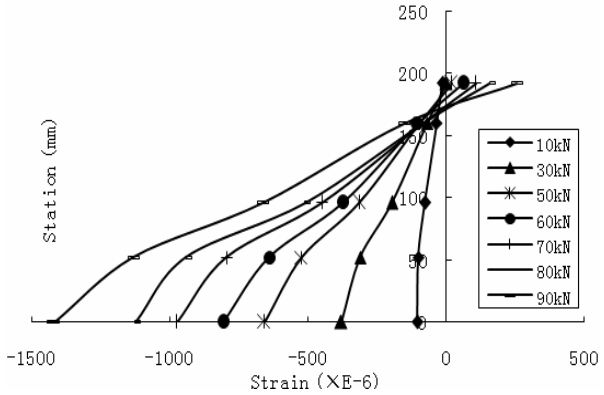

Figure 8. Load-strain of Cross-Section

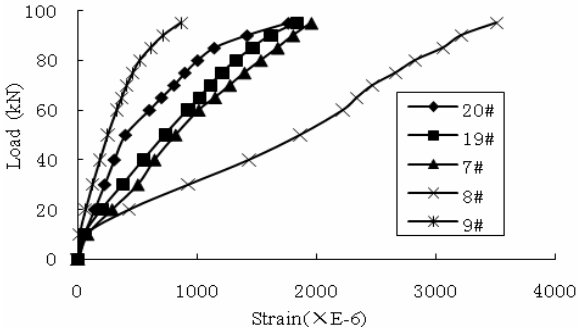

Figure 9. Load-strain of Longitudinal Rebar

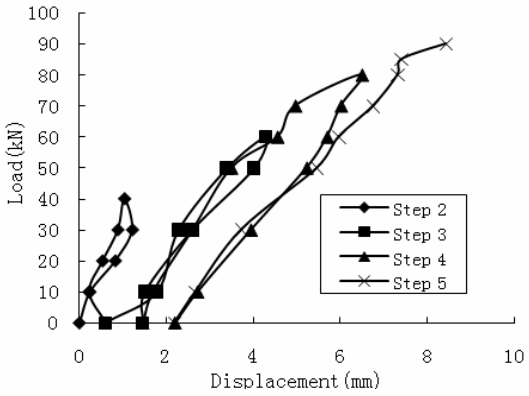

Figure 10. Load-displacement Curves for Specimen HN200B

4. COMPARISONS OF EXPERIMENT AND FEM RESULTS

Strain at each direction, stress at each direction, ultimate load and total deformation were obtained from the finite element analysis. These results have been compared with the corresponding experimental results. The comparison of strains of steel beam section (see Figure 6) is presented in Figure 11 and the comparison of strains of rebar 7# (see Figure 7) in Figure 12. The values of finite element analysis are similar to those of experimental results. The load-deflection curves are shown in Figure 13. Close agreement between the finite element and experimental results can be observed. However, there seems to be some deviation between the results. The discrepancy may be due to the inadequacy in concrete modeling. The concrete is not a homogeneous material and the concrete material model used in the analysis significantly simplifies the actual behavior. Constitutive calculations are performed independently at each integration point in the finite element model. However, when a crack developed in the concrete during the experiment, the moment of inertia of the whole section decreased and the ratio of the deformation to loading increased considerably.

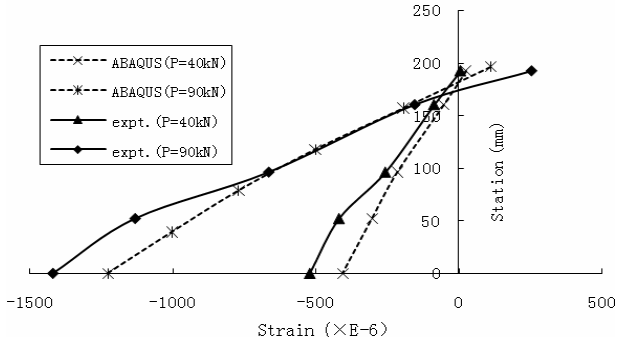

Figure 11. Load-strain of Cross-Section

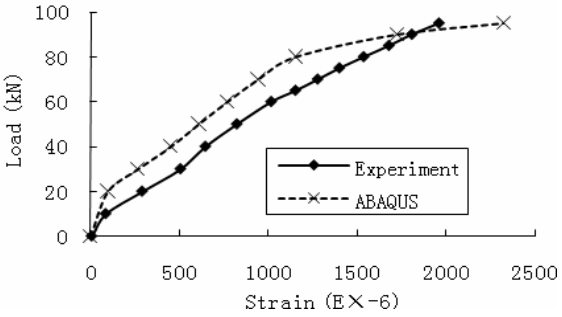

Figure 12. Load-strain of Rebar 7#

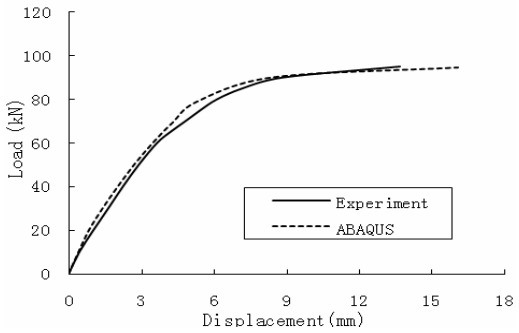

Figure 13. Load-displacement Curves for HN200A

5. RIGIDITY OF COMPOSITE JOINT

The connection of beam to column transfers a set of generalized force components including axial force, shear, moment, and torsion. The influence of torsion can be neglected in plane problem. For most connections, axial deformation and shearing deformation are relatively very small and cal also be neglected. Therefore, only rotational deformation is considered generally. The relative rotation may be defined as shown in Figure 14.

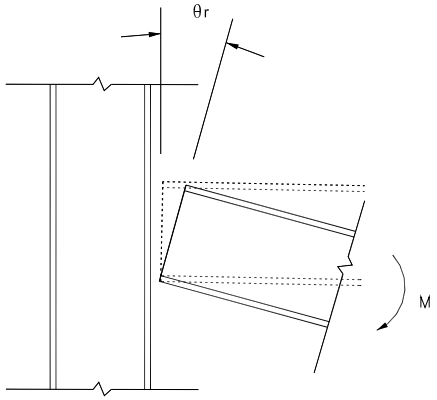

Figure 14. Relative Rotation between Beam and Column

The moment-rotation curves are shown in Figure 15. The experimental results illustrated that the composite joint is semirigid, not fixed. The finite element results are in relatively close agreement with the corresponding experimental results. The finite element model for the joint is valid and acceptable, although there are still some differences between experimental results and finite element analysis.

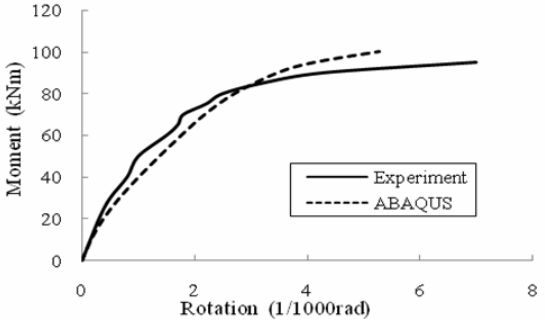

Figure 15. Moment-rotation Curves for HN200A

5.1 Analysis of Influence Factors

For a typical joint, influencing factors on its rigidity include geometrical and mechanical properties. Different joint must account for the contribution of the different components. In this paper, mainly geometrical factors are considered. Influencing factors are shown in Figures 16-20, including height of steel beam, width of steel beam flange, diameter of steel tube, equivalent width of concrete slab and height of concrete slab. Others are not ploted here because of their little influence. According to the analysis, height and equivalent width of concrete slab and height of steel beam are the major factors. More details were provided by Pan [6].

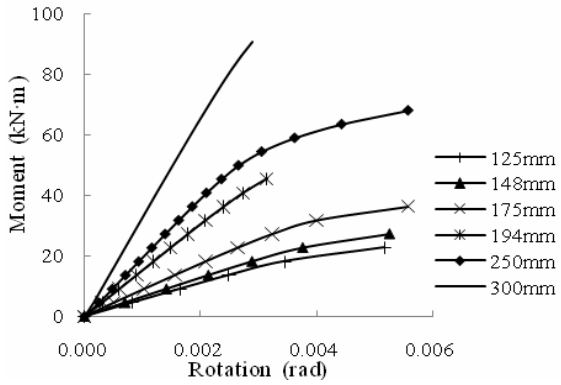

Figure 16. M - θ_r Curves on the Height

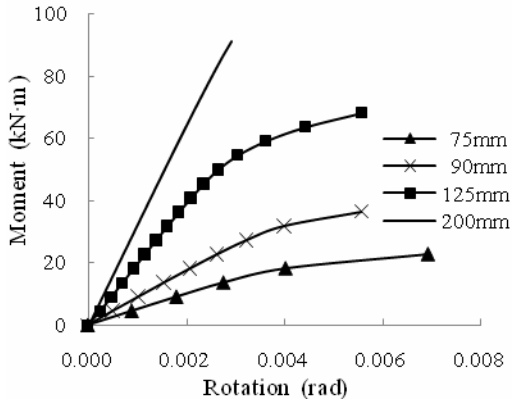

Figure 17. M - θ_r Curves on Width of of Steel Beam Web Steel Beam Flange

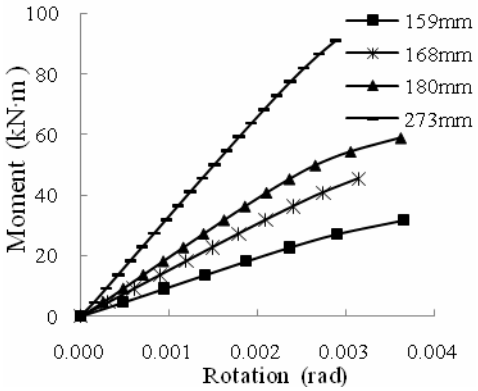

Figure 18. M-θ_r Curves on Diameter

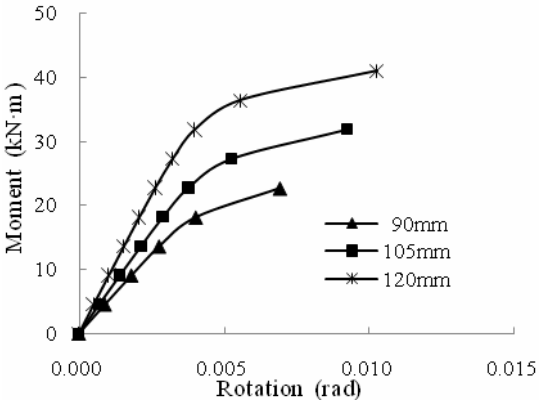

Figure 19. M-θ_r Curves on Equivalent of Steel Tube width of Concrete Slab

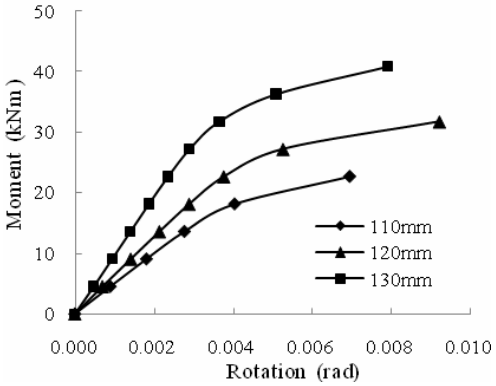

Figure 20. M-θ_r Curves on Thickness of Concrete Slab

5.2 M-θ_r Model

According to the analytical theory of semirigid steel frame in reference Chen and Lui [7] that introduced Colson-Louveau and Kishi-Chen models, and the achievements that the previous researchers had been attained, a power function is used as the $M-\theta_r$ model for the composite joint in Eq. 1. Because of the assumption of full composite action between the concrete slab and steel beam in the analysis, the influencing factors, such as shear studs and reinforcement, are ignored. Only geometrical factors are considered. In Colson-Louveau and Kishi-Chen models, M_u is the ultimate moment of connection, which is obtained by analytical method generally. Considering that the failure may happen in beam for the joint, therefore, let M_u be ultimate moment of beam.

$$\theta_r = \frac{M}{K[1-(M/M_u)^C]} \tag{1}$$

Where M (N·m) is the beam moment of joint, θ_r (rad) is the relative rotation between beam and column, C is a fitting parameter, C=4.118; K is a standard constant, and is determined by Eq. 2.

$$K = d_s^{0.434} t_s^{0.048} b_j^{0.364} h_s^{0.612} b_s^{0.398} h_c^{0.981} b_c^{0.913} \tag{2}$$

Where d_s (mm) is the diameter of steel tube, t_s (mm) is the thickness of steel tube, b_j (mm) is the width of stiffening ring, h_s (mm) is the height of steel beam, b_s (mm) is the width of steel beam flange, h_c (mm) is the thickness of concrete slab, b_c (mm) is the equivalent width of concrete slab.

6. CONCLUSION

A numerical study was carried out by using the software package ABAQUS. The finite element analysis was validated by experimental results. There are still some discrepancies between finite element and experimental values. More vigorous modeling especially for concrete material is essential in order to achieve better accuracy in theoretical prediction.

The joint between steel-concrete composite beam and CFST column with stiffening ring is semirigid. Height and equivalent width of concrete slab and height of steel beam are the major influence factors on semirigid composite joint. A $M-\theta_r$ model of such joint was proposed.

The development of such an analytical model will be useful to designers as it will reduce the need of carrying out expensive and time consuming full-scale tests to predict the behavior of the joints.

ACKNOWLEDGEMENTS

The authors gratefully acknowledge the research grant (50378053) provided by National Natural Science Foundation of China. Main research work was carried out in Shantou University and South China University of Technology in China.

REFERENCES

[1] Chen, J., Wang, Z. and Yuan, J.X., "The Study on the Stiffness of Joint of Steel Beam to CFT Column with Stiffening Ring", Journal of Building Structures, 2004, Vol. 25, No. 4, pp. 43-49.

[2] Wang, Z., Yuan, J.X., Pan, J.R. and Chen, J., "The Study on Semirigid Joint of CFST Frame", Advanced Steel Construction, 2006, Vol. 2, No. 4, pp. 389-399.

[3] Chen, X. and Wang, Z., "Research on the Rigidity of the Joint in Concrete-filled Steel Tubular Frame", Journal of Harbin Institute of Technology, 2007, Vol. 39 (SUPPL. 2), pp. 381-384.

[4] ABAQUS Theory Manual, ABAQUS User's Manual, Hibbit, Karlsson and Sorensen, Inc., USA.

[5] Zhong, S.T., "The Concrete-Filled Steel Tubular Structures (Third Edition)", Tsinghua University Press, 2004.

[6] Pan, J.R., "The Study on Joint Performance of Steel-Concrete Composite Beam to CFT Column", Shantou University Press, 2006.

[7] Chen, W.F. and Lui, E.M., "Stability Design of Steel Frames", CRC Press, 1991.

INVESTIGATIONS ON THE BEHAVIOUR OF SEMI-RIGID ENDPLATE CONNECTIONS

Arul Jayachandran S.*, Marimuthu V., Prabha P., Seetharaman S. and Pandian N.

Scientists, Structural Engineering Research Centre, CSIR campus, Taramani, Chennai-600 113, India
**(Corresponding author: E-mail: arulsteel@yahoo.com)*

Received: 31 March 2008; Revised: 25 July 2008; Accepted: 29 July 2008

ABSTRACT: The present paper describes experimental and numerical evaluation of moment-rotation behaviour of semi-rigid bolted endplate connections. In the experimental programme of research, eight specimens of endplate connections which have end plates extended in the tension side alone are investigated. The column webs are stiffened at the beam flange column interface. Numerical studies are conducted using ABAQUS finite element program for all the eight specimens. The finite element model is validated through a comparison of moment-rotation curves and failure loads obtained from the experimental results. Further, the results of the experimental analysis are used in reassessing the Frye-Morris [4] polynomial model which is recommended in the Indian limit state code for structural steel design, the IS:800 [17].

Keywords: *Semi-rigid connection; moment-rotation behaviour; endplate connection; Frye-Morris model*

1. INTRODUCTION

Connections play an important role in the design of any steel structure. In the past two decades the incorporation of semi-rigid behaviour of steel connection in the design has attracted attention of researchers since the consideration of real behaviour of the connections leads to simpler, reliable designs and better economy in construction. In recent years, endplate connections have gained popularity in steel building construction due to its simplicity of fabrication, and good ductile performance under static and dynamic loadings. A simple endplate connection consists of a rectangular steel plate welded at shop to the beam end, and bolted to the column flange at site, either snug tight or fully pre tensioned. Adjustments can be made to a simple endplate connection to meet the requirements of different situations. For example, stiffeners can be added to maintain the stiffness of a connection while reducing the endplate thickness. A 3D view of an endplate connection is shown in Figure 1. This semi-rigid connection comes in the upper end of the semi-rigid connection moment-rotation behavior spectrum. Even though these connections exhibit high stiffness, the end plate yielding is a major mechanism for strength and yielding.

2. BRIEF REVIEW OF LITERATURE

Extensive research has been directed to the modeling, analysis and design of the end plate connections employing elastic and plastic theories, finite element procedures and full scale testing. Research starting in the early 1950s and continuing to the present, resulted in refined design procedures for end-plate connections. The earlier design methods were based on simple statical assumptions concerning prying forces. These methods resulted in larger end plate thicknesses and larger diameter bolts. Recent studies have used the finite element method and regression analysis to develop design equations. Accurate solutions can be developed using the latter technique.

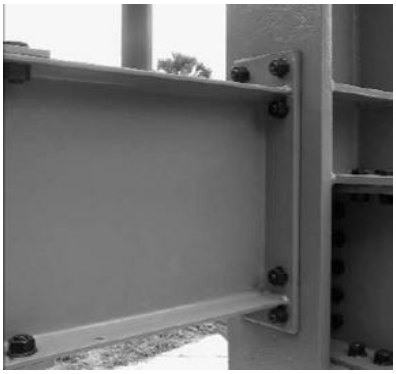

Figure 1. Bolted Extended End-Plate Connection

Prior to 1975, Doughty and McGuire [1], Kato and McGuire [2], Nair et al. [3], developed design criteria for the end-plate connections based on the 'Tee-Stub analogy'. In fact these methods predict a high 'prying action' which in turn resulted in large end-plate thicknesses and also large bolt diameters. For seven commonly used connection types, Frye and Morris [4] presented a polynomial model for analysing steel frames with combination of pinned connections, fixed connections, connections with any specified flexibility characteristics. A method is outlined for expressing, in a non dimensional form, the moment-rotation characteristics for all connections of a given type. This method is quite simple to use and it is dependent on geometrical parameter of the connection. Later, Packer and Morris [5] used curved yield lines to predict end-plate capacity with testing directed at the failure of the column flange. Finite element methodology for the analysis of end-plates was first presented by Krishnamurthy et al. [6]. A 2-dimensional/3-dimensional finite element analysis was conducted to determine adequate correlation between results. Krishnamurthy et al. [6] concluded that prying forces do not exist in moment end-plate connections based on this study. Mann and Morris [7] recommended a design procedure for four bolt extended-stiffened end plate connections. The required end-plate thickness was determined using straight yield-line patterns passing through the bolts. The values for end-plate thickness achieved by this design procedure were reported to withstand the plastic moment strength of the beam. Maxwell et al. [8] used simple bending theory, yield line theory, finite difference method and the finite element method to study the endplate and other connections. They concluded that the finite element method was the best feasible alternative for analyzing such a problem, because it will significantly reduce the number of full scale tests normally required to establish behaviour with this type of investigations. Philips and Packer et al. [9] conducted a series of tests to determine the influence of the endplate thickness on moment rotation characteristics and the endplate collapse mechanism. The introduction of yield line theory as the primary analytical tool in predicting end-plate strengths resulted in greater accuracy of predicted strengths, leading to more economical plate design. Zoetemeijer et al. [10] used the yield line theory for analysis of T-stub and end-plate connections with four bolts. In his study, a design method for the tension side of the statically loaded connection is developed. The design methodology is based on two different collapse mechanisms. Tests were performed to ensure that the developed design rules would lead to connections that would satisfy the limit state of deformations. The test results showed a satisfactory agreement with the proposed design rules. Tsai and Popov [11] conducted three tests on four-bolt stiffened endplate connections under cyclic loading. They found that the conventional design procedure for endplate connections subjected to monotonic loading was satisfactory except for bolt sizing. Korol et al. [12] presented seven full scale extended end plate beam to column connections under cyclic loading. Ghobarah et al. [13] carried out five numbers of beam-to-column bolted end plate connections under cyclic loading simulating the earthquake effects on steel moment resisting frame to validate the behaviour of connection as well as the connecting elements. Foley and Vinnakota [14] proposed a three parameter power model for the moment-rotation behaviour of extended end plate connections with

unstiffened columns. More recently, Mofid et al. [15] developed a physically based yield line model to predict the ultimate moment capacity and yield moment of the bolted extended endplate connections, using the connection dimensions as input. The analytical method is proposed for the extended endplate joints having four bolts in tension region, and without any stiffened plate. Comparison is made to a series of test results for a range of bolted endplate moment connections, and good agreement is achieved. Furthermore, this method has been claimed to efficiently serve design engineers in real design condition. Also, Abolmaali et al. [16] developed two types of moment rotation model equations using Finite Element Analysis. The accuracy of the FEM and its results were compared with experimental results. The obtained FEM results were fitted with Romberg-Osgood and Three Parameter Power models.

The Indian Code for general construction in steel IS:800 [17] has proposed the Frye and Morris [4] model for the design of semi rigid connections. In spite of the criticism against this method, as it yields negative derivatives, this method is simple to use and uses the geometrical parameters of the connection. However the exponents of the Frye-Morris [4] model have not been extensively verified by experiments. Various methods may be used for this verification such as empirical, analytical, mechanical, numerical and experimental tests. In the present study it has been proposed to conduct experimental and numerical investigation to assess the Frye and Morris [4] polynomial model.

3. EXPERIMENTAL INVESTIGATION

Eight test cases are identified for experimental investigation on end plate connections by varying the thicknesses of the end plate and the lever arm distance (distance from the centre of top tension bolt to the centre of thickness of the compression flange of the beam). The details of the experimental specimen are shown in Table 1, where ISMB 300 refers to Indian standard medium beam of depth 300mm and the flange width is 170mm. All endplate connections are made using High Strength Friction Grip (HSFG) bolts. The endplate connections are classified with respect to the thickness of endplate and the lever arm distance. The values of the geometric variables for the different endplate connections with HSFG bolt are presented in Figure 2 and Table 2.

Table 1. Endplate Connection Types and Sections Used

No.	Test ID.	Column	Beam	Endplate		Bolt type
				Thickness in (mm)	Length in (mm)	
1	EP-1-8	ISMB 300	ISMB 300	8	400	High Strength Friction Grip bolts of Class 8.8, 16Ø
2	EP-2-8			8	420	
3	EP-3-10			10	440	
4	EP-4-10			10	420	
5	EP-5-10			10	400	
6	EP-6-12			12	400	
7	EP-7-12			12	420	
8	EP-8-12			12	440	

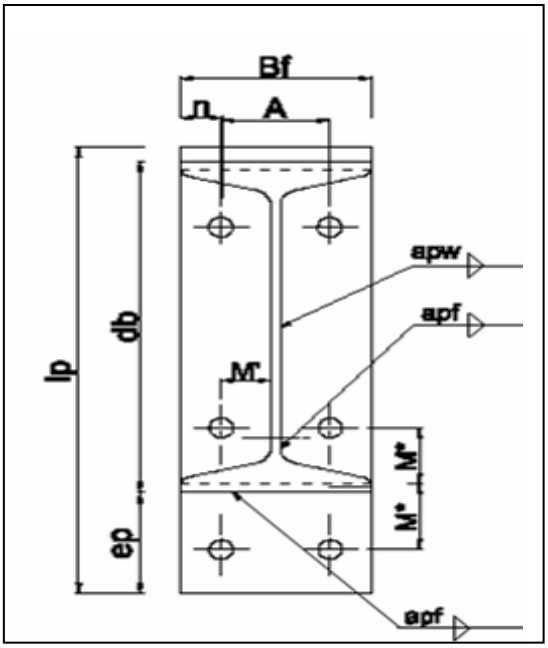

Figure 2. Notations used in the Endplate Connections

Table 2. Geometric Variables of Different Endplate Connections

S. No.	TEST ID.	B_f	t_p	A	M'	N	M^*	d_b	e_p	l_p	d_{bolt}	a_{pw}	a_{pf}
1	EP-1-8	*140*	*8*	*80*	*36.25*	*30*	*55*	*300*	*88.6*	*400*	*16*	*6*	*8*
2	EP- 2-8	*140*	*8*	*80*	*36.25*	*30*	*75*	*300*	*108.6*	*420*	*16*	*6*	*8*
3	EP-3-10	*140*	*10*	*80*	*36.25*	*30*	*55*	*300*	*88.6*	*400*	*16*	*6*	*8*
4	EP- 4-10	*140*	*10*	*80*	*36.25*	*30*	*75*	*300*	*108.6*	*420*	*16*	*6*	*8*
5	EP-5-10	*140*	*10*	*80*	*36.25*	*30*	*95*	*300*	*128.6*	*440*	*16*	*6*	*8*
6	EP-6-12	*140*	*12*	*80*	*36.25*	*30*	*55*	*300*	*88.6*	*400*	*16*	*6*	*8*
7	EP-7-12	*140*	*12*	*80*	*36.25*	*30*	*75*	*300*	*108.6*	*420*	*16*	*6*	*8*
8	EP-8-12	*140*	*12*	*80*	*36.25*	*30*	*95*	*300*	*128.6*	*440*	*16*	*6*	*8*

3.1 Test Setup and Instrumentation

The present experimental test set up consists of two beams connected to a stub column by two endplates connected on either side of the stub column as shown in Figure 3 and Figure 4. All the beams and stub columns used in the test was ISMB300 section of FE 250 steel whose nominal yield strength is 250 MPa. Each beam of length 1150mm is used for all endplate connections. The beam assembly is supported on a roller and hinge assembly. Roller and hinge supports were made up of mild steel. The length and diameter of the roller was 200 mm and 90 mm respectively. The hinge was designed in such way that the support allowed the maximum rotation of 28.03^o. Endplates of grade Fe250 were used. By varying its thickness 8mm, 10mm and 12mm, using the combinations with 400mm, 420mm and 440mm length of plate i,e varying only the distance of

tension side bolts from the centre of beam flange by 55mm, 75mm and 95mm. The stub column flanges are stiffened by 8 mm thick stiffeners fillet welded (6mm) to the column web and flanges. This is done to avoid the yielding of column flange, so that the column can be repeatedly used for other specimens also. The beam which is assumed rigid is welded to the endplate specimens on its both sides, so as to use the beam by reverting and then studying a different connection parameter. The stub column of height 650 mm is used. The span of the beam column joint assembly is 2.10 m. A 60 T capacity hydraulic jack is used for applying load over the specimen. The jack is supported by the cross beam of reaction frame.

Load transfer is achieved by pumping highly viscous oil over the piston. Jack is controlled by instrumentation on an electrical panel board. Mild steel plate of size 190mm x 350mm was kept over the specimen to distribute the load evenly over the stub column. The advantage of the present setup is that since the column does not rotate and displaces only up and down, the relative rotation between the column and beam is due to the contribution of the connection deformation alone; hence the relative rotation θ_r can be easily measured using an inclinometer. During testing the verticality of the stub column is checked using plumb-bob.

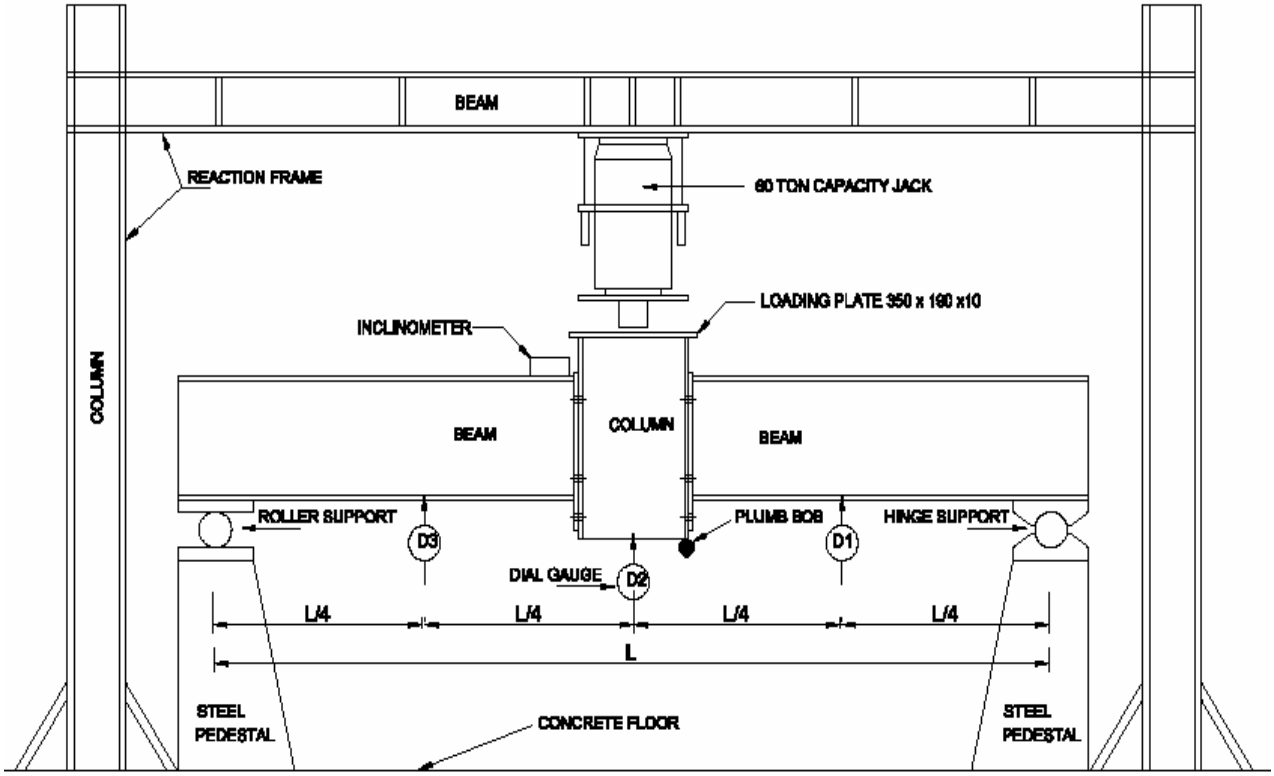

Figure 3. Test Setup and Instrumentation

Figure 4. Photographic View of Test Set-Up

The least count of the dial gauge used is 0.01mm. The maximum deflection allowed in one rotation of dial is 25mm. The number of strain gauges is fixed based on the yield line pattern that will develop on the endplate (Mofid et al. [15], Mann and Morris [7]. The major yield lines are as follows (1) along the bottommost tension bolt row, (2) between the top of tension flange weld and the endplate, (3) adjacent to the web weld and the plate, (4) Inclined line from the centre of the bolt of the mid tension bolt row to the mid of the top tension flange weld and (5) inclined line from the centre of the bolt of the mid tension bolt row to the centre of the compression flange of beam. All specimens showed very stiff linear behaviour up to a minimum load of 7.5 tonnes. The contact opening of the endplates with respect to the column flange on the tension side is symmetric on both sides for all specimens and throughout the tests. Initially the neutral axis lies at centre (i,e., between the compression bolt row and the tension bolt row) due to pre-tension and it slowly goes to the compression flange of the beam as the load increases. It can be seen as an opening between the compression bolt row and mid tension bolt row (Figure 5). Deflection is measured at quarter spans from each end and at mid span. Dial gauge located near the roller support is named as D1, dial gauge located near the hinge support is named as D3 and dial gauge located middle span is named as D2. Deflection patterns of D1 and D3 are same. The general observations of the failure mode in all the specimens are that the second tension bolt rows undergo bending along with axial tension.

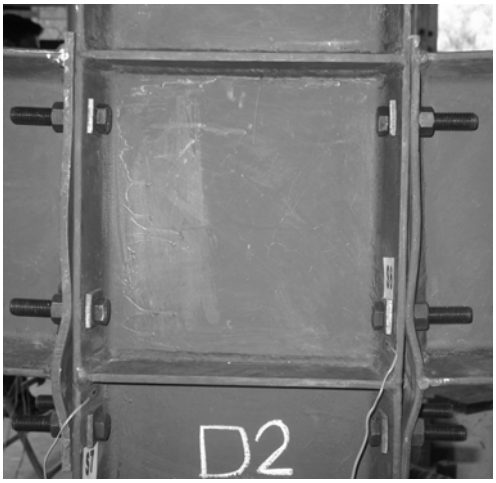

Figure 5. Contact Opening of Endplate Connection

4. EXPERIMENTAL RESULTS AND DISCUSSIONS

Seven strain gauges are used to measure strain variation; out of which five are fixed in the endplates and two are fixed in the stub column at the tension zone near the stiffener. The strain variation with the applied load for the specimen EP-1-8 is shown in Figure 6. The strains observed in the stub column are very less; hence the effect of buckling of the column flange can be completely neglected.

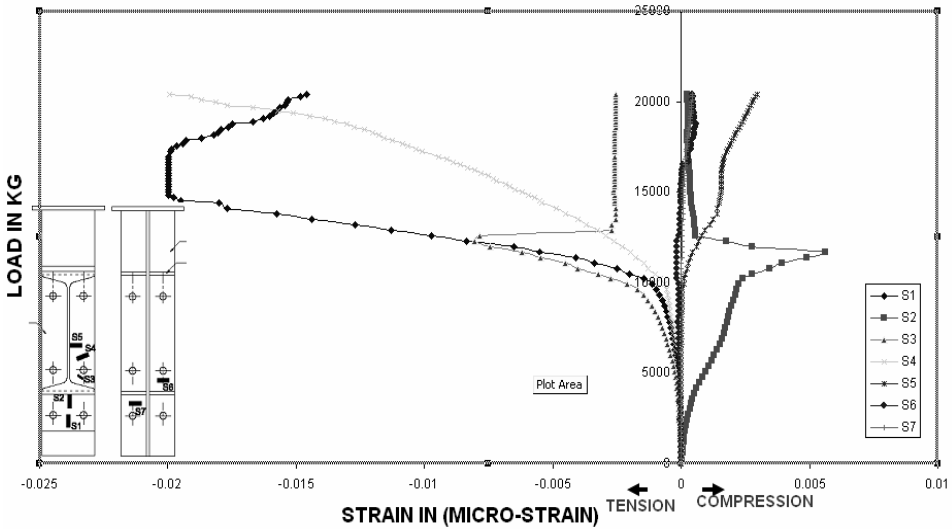

Figure 6. Load vs Microstrain for EP-1-8

The combined moment-rotation and load-deflection curves of all the specimens are shown in Figure 7 and Figure 8 respectively.

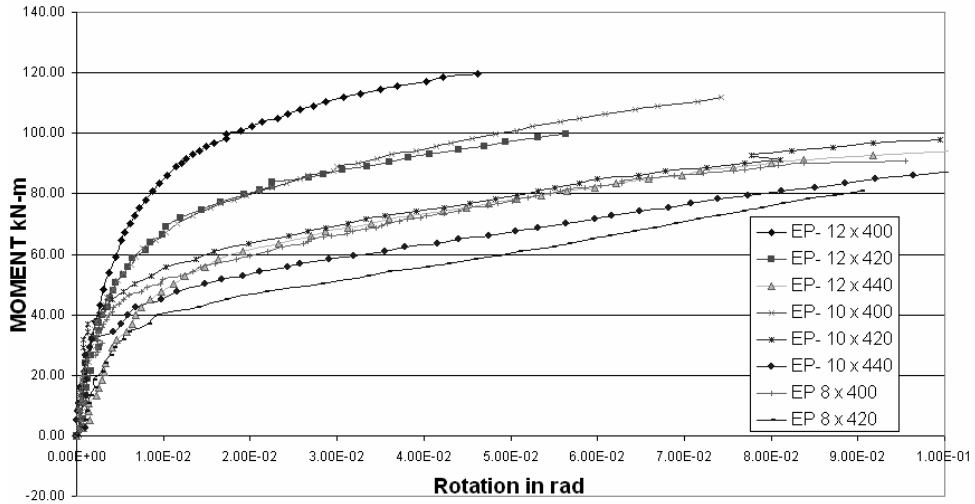

Figure 7. M-θr Relationship of Different Endplate Specimens

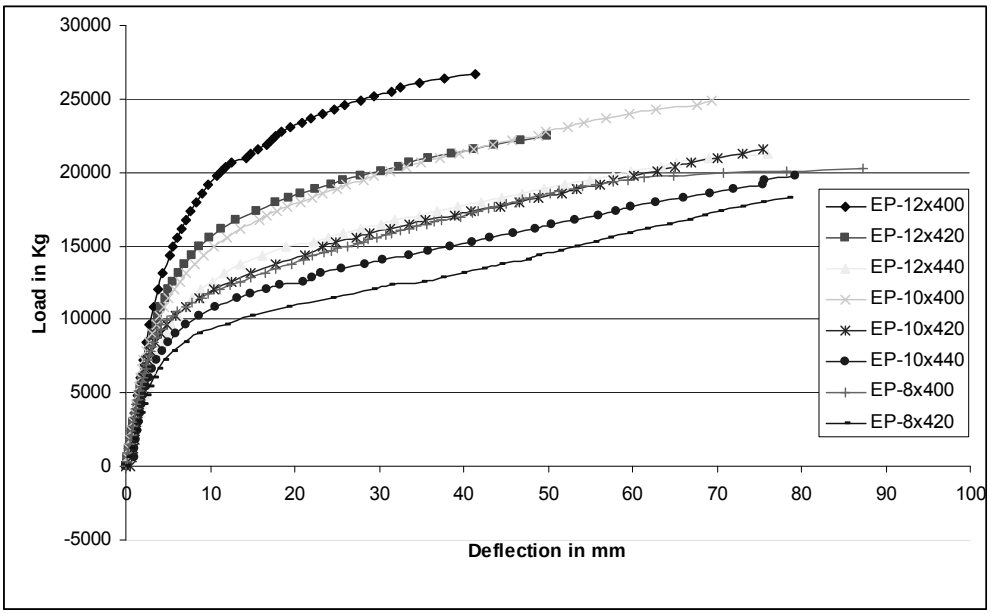

Figure 8. Load-Deflection Behaviour of Different Endplate Specimens

Focusing first on the end plate behavior, the relative displacements between the endplate and the column flange for all the specimens are presented in Figures 9 - 11. The maximum relative displacement of the specimen EP-1-8 is 24mm and for the specimen EP-2-8 is 30mm. The maximum relative displacement of the specimen EP-3-10 is 45mm, for the specimen EP-4-10 is 28mm and for the specimen EP-5-10 is 24mm. The maximum relative displacement of the specimen EP-6-12 is 37mm, for the specimen EP-7-12 is 42mm and for the specimen EP-8-12 is 28mm.

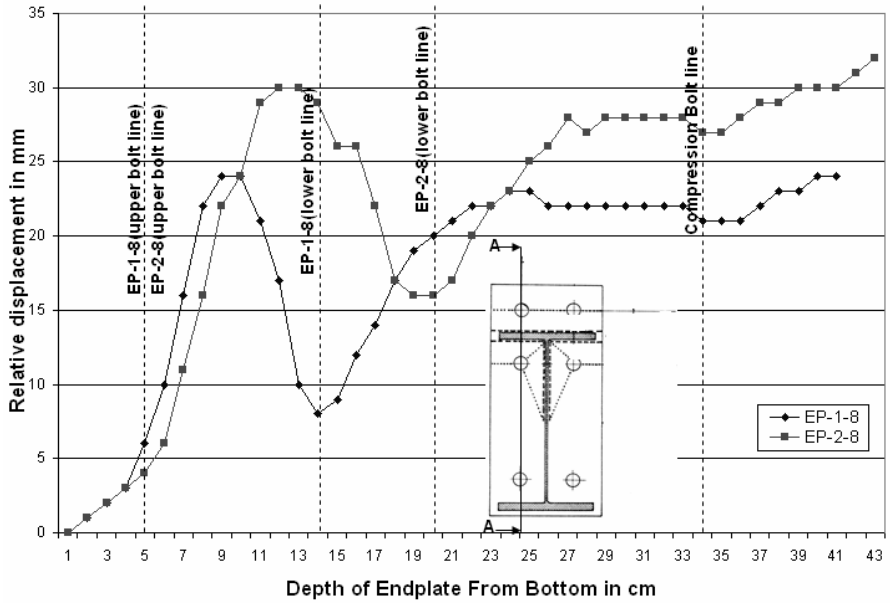

Figure 9. Endplate Relative Displacements of 8mm Thick Endplates

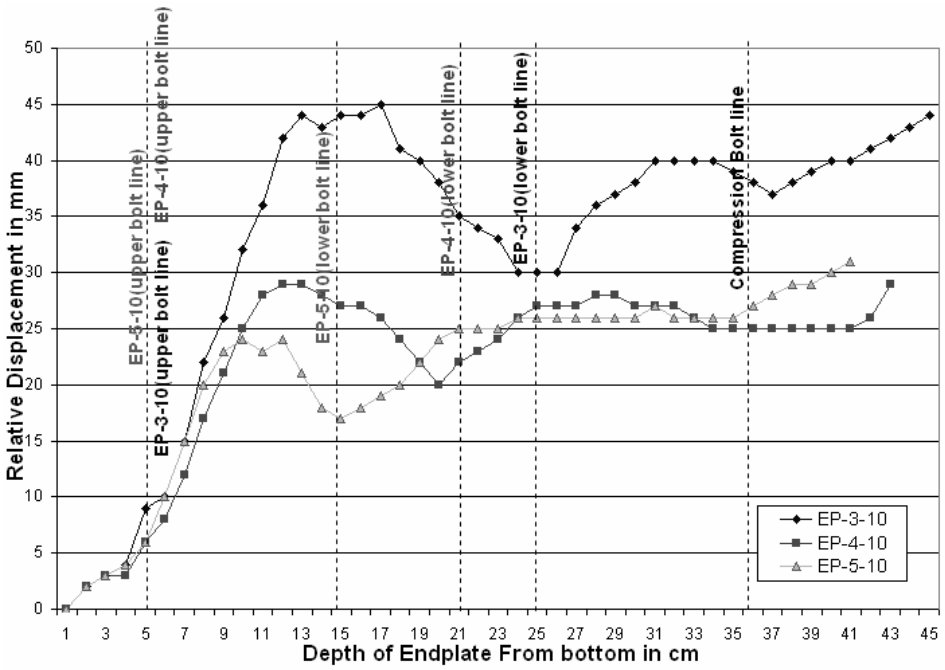

Figure 10. Relative Displacement of 10mm Thick Endplates

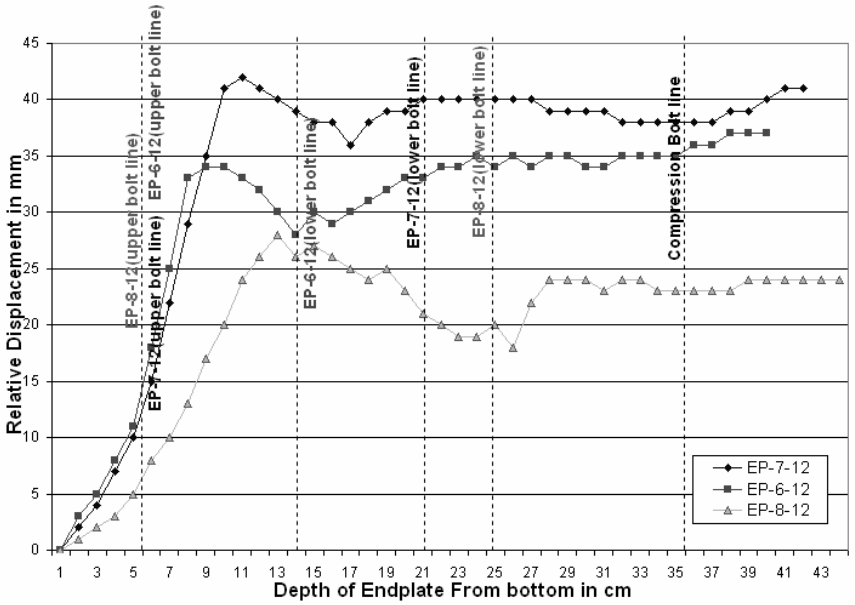

Figure 11. Relative Displacement of 12mm Thick Endplates

5. NUMERICAL INVESTIGATIONS ON END PLATE CONNECTIONS

5.1 FINITE ELEMENT MODELING

Finite element analysis of all the eight test specimens was carried out using ABAQUS software [Hibbit et al. [18])] to assess the design procedure. All the connecting members including the bolts were modeled using the element C3D8R which refers to continuum three dimensional 8-noded brick element with reduced order integration. This element has three degrees of freedom at each node, translations in the nodal x, y, & z direction. As the solid elements do not have rotational degree of freedom, the end-plate and the column flange are discretized across the thickness also to

consider the effect of bending. Small sliding surface-to-surface contact was considered for all the contacts in the connection which assumes relatively small sliding, but can undergo arbitrary rotation of the bodies. The connection between the beam and the end-plate was assumed to be rigid. Frictional (value μ= 0.3) contact using penalty stiffness formulation was considered for the tangential contact between the end-plate and the column flange. The normal contact between the end-plate and the column flange was considered as hard using augmented Lagrange formulation. Hard constraint is used for the connection of bolt head/nut to the beam/column.

The yield and ultimate tensile stresses for the beams, column and end-plate were considered as 250 and 420 MPa respectively. The ultimate strain considered was 0.23. High strength friction grip bolts (8.8 grade) were used in this study. The yield and ultimate tensile stresses considered for the bolts were 640 and 800 MPa respectively. The ultimate strain considered was 0.12. A pretension force of about 0.7 times the bolt yield stress [Maggi et al. [19]] was applied at the center section of the bolt using the pretension option in ABAQUS. Hexagonal bolt heads and nuts are idealized as circular bolt heads and nuts to simplify the model. Washers are not modeled. Bolt holes are assumed to be 1.5mm larger than the bolt size (D=17.5mm). One end of the beam-column assembly is supported by a hinge and the other by a roller to simulate simply supported condition. The fillets in the angles are not modeled in order to reduce the complexity of the model. Final arrangement of the finite element mesh is decided based upon the computer time, convergence of solution and by comparison with the experiment results. Mesh refinement is carried out for corners, holes and the angles, where stress concentration is expected to occur. The sizes of meshes are controlled between the components of connection to enable surface to- surface contacts and easy convergence.

The load application has been effected in two load steps. In the first step, pre tensioning forces are applied to all the bolts. In the second step, uniform pressure load is applied over the stub column (Figure 12). Non linearity arises from large displacement effects, material non linearity and boundary nonlinearity due to contact and friction. In the present study, material and boundary nonlinearities are considered. The highly non linear nature of this problem, leads to non-convergence of the solution. It is overcome by using the nonlinear analysis option of ABAQUS. Figure 13 shows the finite element model and the deformed configuration of a typical end-plate connection. The deformations and rotations were observed to be higher than that observed from the test near to the failure.

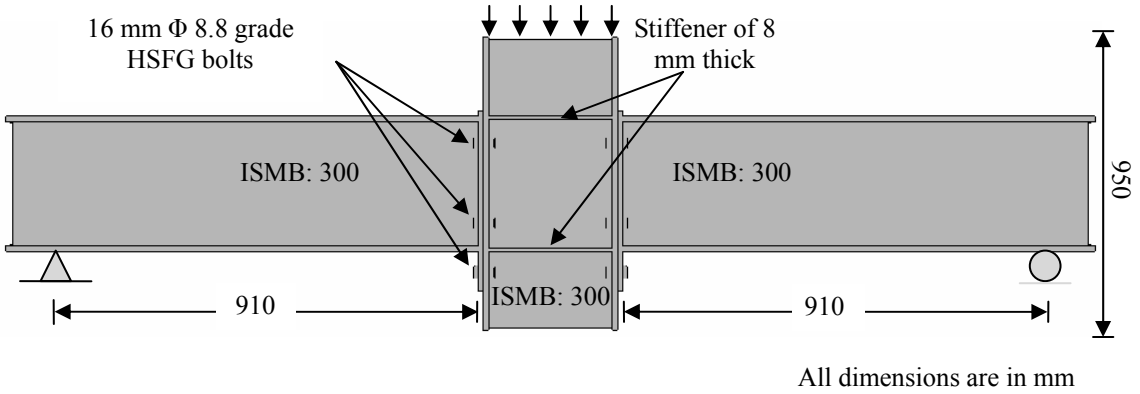

Figure 12. Connection Details

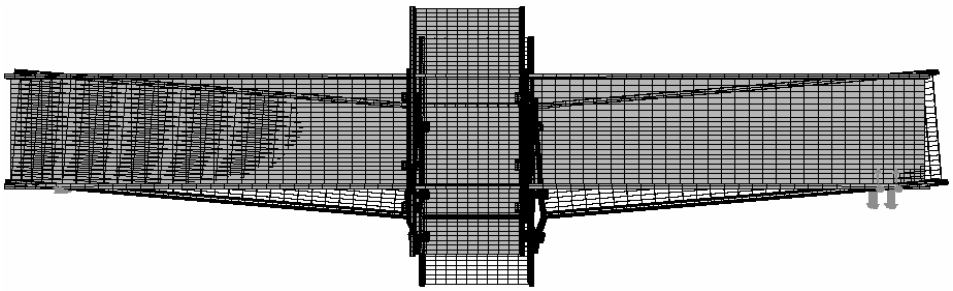

Figure 13. FE Model and the Deformed Configuration of a
Typical End-Plate Connected Beam Assembly Model

5.2 COMPARISON OF ABAQUS RESULT WITH EXPERIMENTS

Comparison of Moment-Rotation curves

Figures 14-16. show the comparison of moment-rotation curves obtained from the finite element analysis with those obtained from the tests, and predictions by Frye-Morris [4] model. For EP-1-8 specimen, the experimental M-θr curve is linear and stiff upto 105 kN and beyond that the flexibility of connection starts. The Frye-Morris model traces more or less the experimental curve. The experimental M-θr curve show that the EP-2-8 specimen is linear and stiff upto 72 kN and beyond that the flexibility of connection starts. This connection behaviour is more flexible than the previous specimen. The Frye-Morris model is stiffer than the experimental curve. Similar to that of 8mm thick plate with 400mm plate length, the behaviour of EP-5-10 specimen matches with experimental value. The experimental M-θr curve is linear and stiff upto 144 kN and beyond that the ductility of connection starts. For EP-4-10 specimen, the experimental M-θr curve is linear and stiff upto 90 kN and beyond that the ductility of connection starts. This connection behavior is more flexible and similar to that of EP-2-8 specimen. The Frye-Morris model curve shows a stiffer behaviour than the experimental curve. EP-3-10 specimen behaves stiffer than the previous specimen 10 x 420 and the Frye-Morris model curve is conservative for this specimen. The curve is linear upto 78kN and the ductility of the connection starts beyond that load. The behaviour of experimental moment rotation curve of EP-6-12 specimen is similar to that of the 8mm & 10mm thick endplate. The Frye-Morris model curves are unconservative when compared to the experimental ones. The experimental M-θr curve is linear and stiff upto 174 kN and beyond that the ductility of connection starts. The experimental M-θr curve of EP-7-12 specimen is linear and stiff upto 132 kN and beyond that the ductility of connection starts. The connection behavior is more flexible and similar to that of 8mm x420mm. The Frye-Morris model curve is slightly stiffer than the experimental curve. The moment rotation is so stiff than the previous specimen 10 x 420 and the Frye-Morris model is much conservative for EP-8-12 specimen. The curve is linear upto 114kN and the ductility of the connection start beyond that load.

A good correlation of moment rotation curves obtained from the FEM with that obtained from the tests can be seen up to a specimen deflection of L/100 which is well beyond the allowable deflection for serviceability (L/180) as prescribed in the IS: 800 draft [17] for 10 mm and 12 mm thick plates. The moment rotation curve for 8 mm thick plate slightly deviates from the test curve after a deflection of L/525, but the initial and final stiffness correlate well with the test results. It is also noticed that the stiffness of the connection increases with the increase in the thickness of the end-plate and reduces as the lever arm increases both in tests as well as FEM.

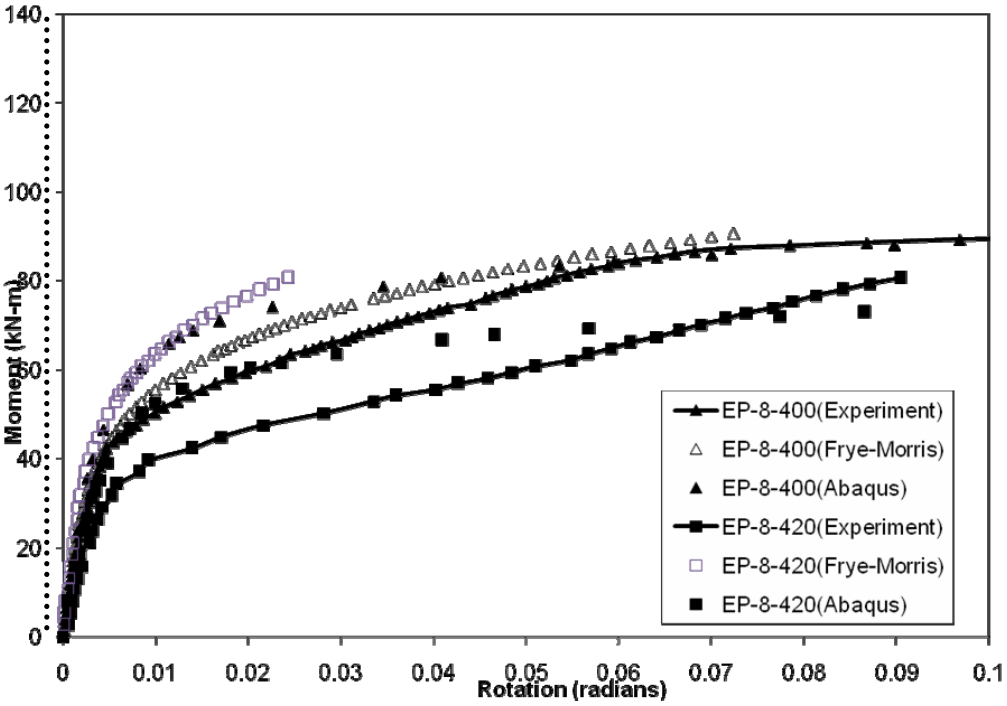

Figure 14. Comparison of Moment Rotation Curves for All 8mm Endplates

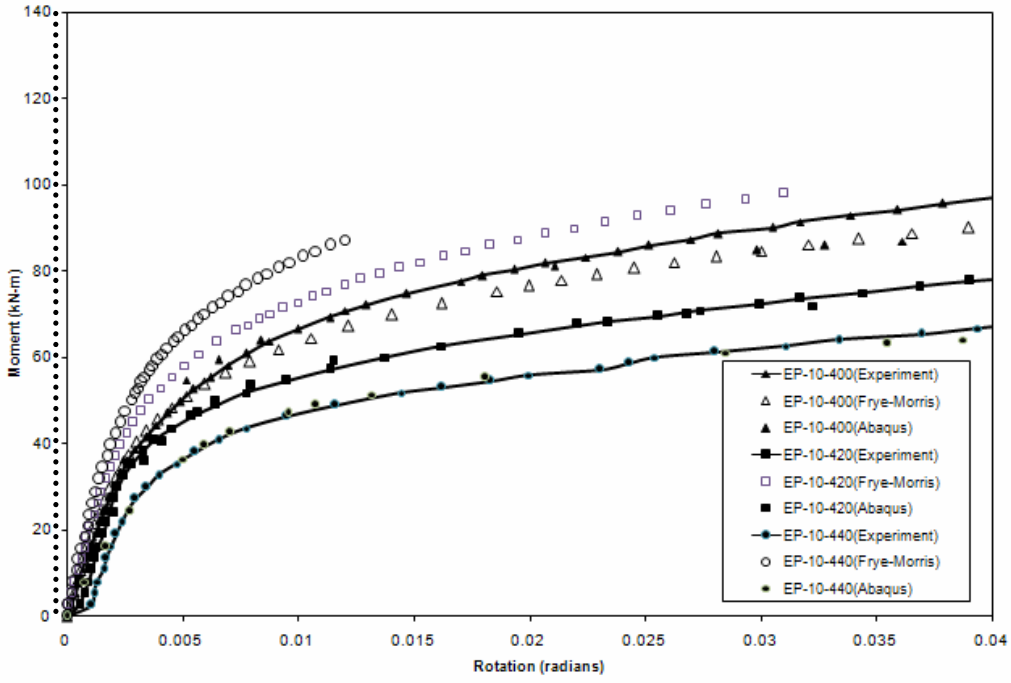

Figure 15. Comparison of Moment Rotation Curves for All 10mm Endplates

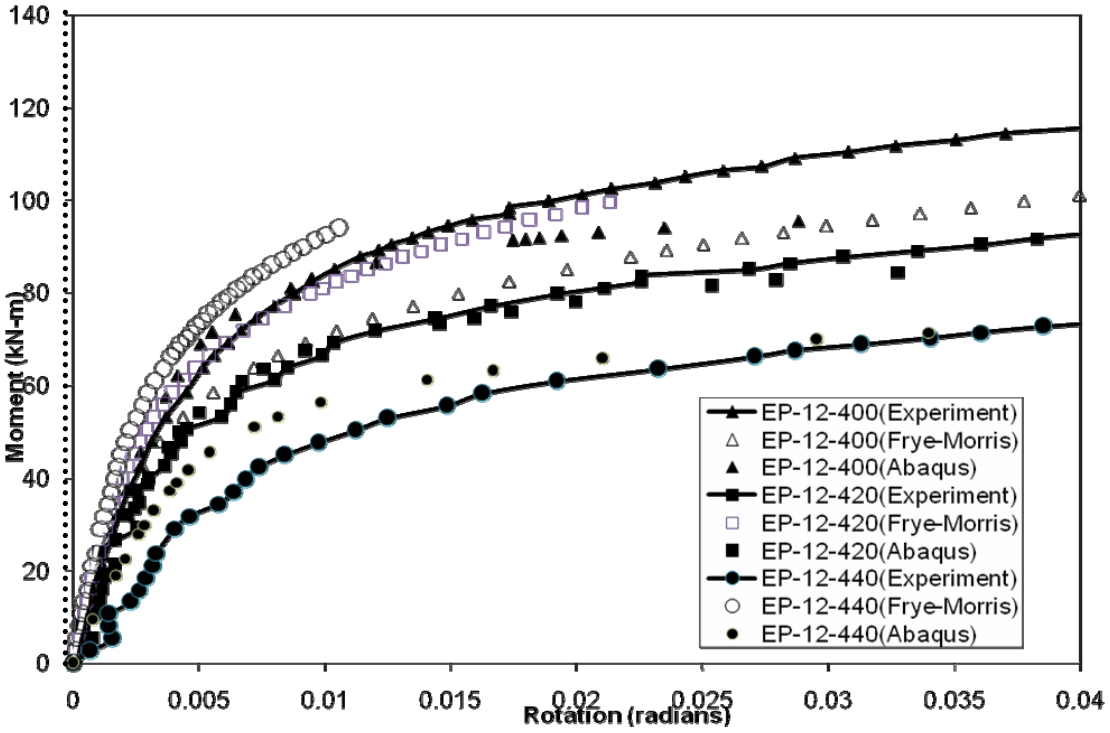

Figure 16. Comparison of Moment Rotation Curves for All 12mm Endplates

Comparison of Failure modes and Loads

Figure 17. shows the stresses in all the parts of the connection at failure. Two types of failures (i) end-plate rupture and (ii) bolt rupture were observed in the tests as well as in FEM analysis (Figure 18). Table 3 shows comparison of failure modes and loads obtained from FEM with that obtained from the tests. The specimen with 8 mm thick and 400 mm depth end plate failed due to tearing of end-plate. As the lever arm increases, the failure of the specimens is by fracture of the bottom row of tension bolts. For plate with 10 mm thick and 400 and 420 mm depth, the failure is by tearing of end-plate by finite element analysis against fracture of the middle row of bolts observed in tests. In both the cases EP-3-10 and EP-4-10, these two limit states such as tearing of endplate and fracture of bolts were close to each other. Since finite element analysis is based on ideal assumptions, in which the fracture of the bolt occurred before the fracture of endplate. However in the experiments the endplate fractured before the fracture of the bolt. For larger lever arm, failure is by fracture of bottom row of tension bolts in finite element analysis and tests. For plate with 12 mm thick and 400 and 420mm, the failure is by fracture of bottom row of bolts by finite element analysis against the fracture of the middle row of bolts observed in tests. For larger lever arm, failure is by fracture of bottom row of tension bolts by both finite element analysis and tests. The failure loads obtained from FEM analysis compare within 12% of the loads obtained from the tests.

Table 3. Failure Modes and Loads

Specimen Designation	Failure load (kN)		Mode of failure	
	Experiment	FE analysis	Experiment	FE analysis
EP-1-8	204	203.5	Tearing of end-plate	
EP-2-8	185	174	Fracture of bottom row tension bolt	
EP-3-10	252	221.3	Tearing of end-plate	Fracture of middle row tension bolt
EP-4-10	219	193.3		
EP-5-10	201	188.5	Fracture of bottom row tension bolt	
EP-6-12	270	246.2	Fracture of bottom row tension bolt	Fracture of middle row tension bolt
EP-7-12	225	214.9		
EP-8-12	210	196.5		Fracture of bottom row tension bolt

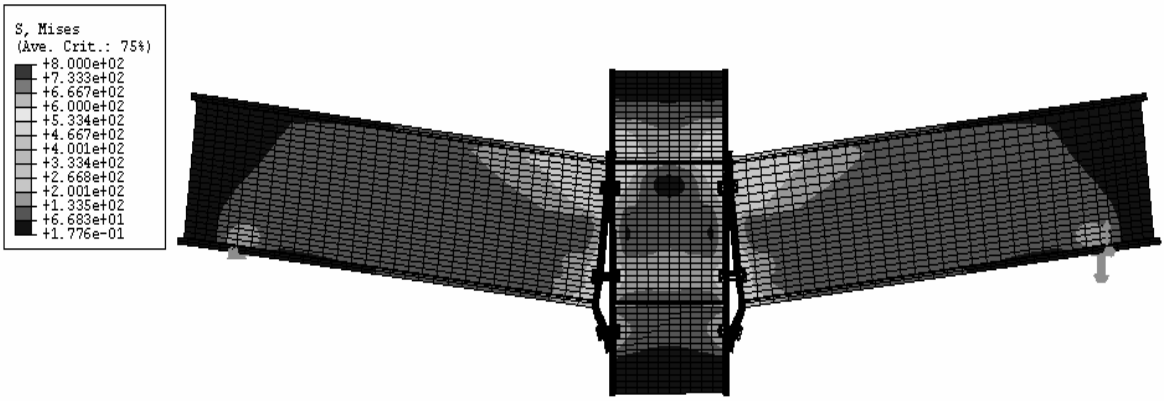

Figure 17. Stress contour at failure

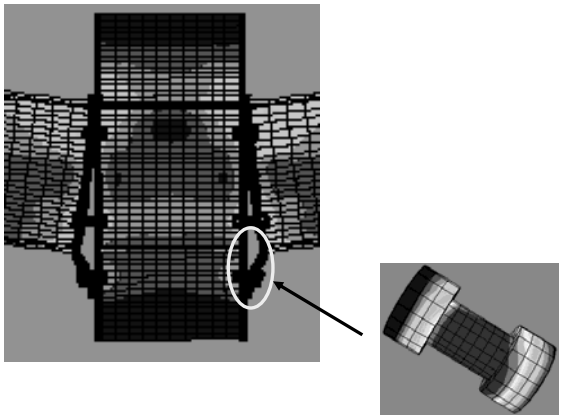

FE Model

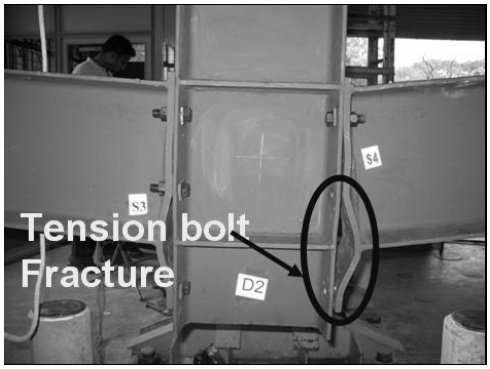

Experiment

(a) Bolt Rupture

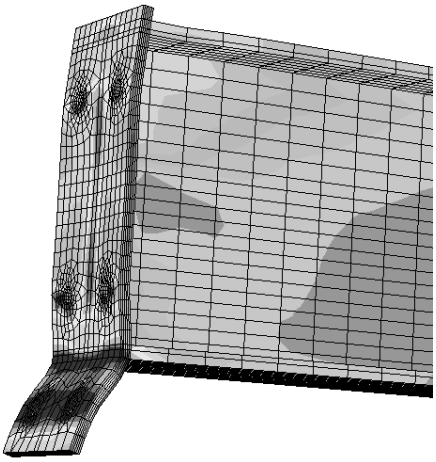

FE model

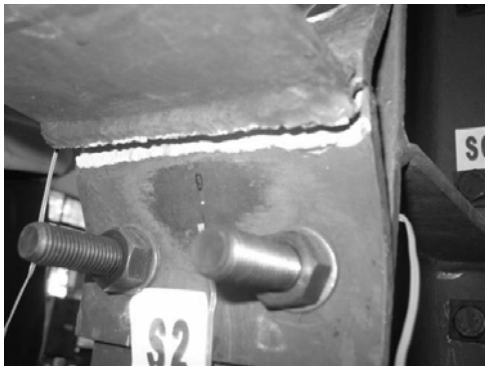

Experiment

(b) End-plate Rupture

Figure 18. Failure Modes

6. VALIDATION OF FRYE-MORRIS MODEL

As discussed earlier Frye-Morris [4] model, a non-dimensional polynomial model for moment-rotation characterization of the connections, has been incorporated in IS:800 [17]. This model has not been evaluated for Indian construction practices. The polynomial model for the moment-rotation behaviour of the endplate connections is reassessed based on the present experimental and numerical results.

The original Frye-Morris [4] equation for endplate connection is given by

$$\theta_r = 2.06 \times 10^{-1}(KM) + 5.36 \times 10^{2}(KM)^3 + 1.31 \times 10^{7}(KM)^5 \quad (1)$$

(Moment kN-m, Parameters in cm) and the standardization factor for the endplate connection is given as

$$K = t_p^{-0.6} . d_g^{-2.4} \quad (2)$$

The above equations are based on limited experimental results numbering 15, which are reported in the literature between 1948 - 1970. However the construction methods themselves have undergone a sea change world over, resulting in very flexible endplate connections. This flexibility is not reflected in the original equations which were based on tests with very stiff connection characteristics. The size parameters for the endplate connections with the column stiffeners are thickness of plate (t_p) and the lever arm distance (d_g). The moment-rotation curves are generated by systematically varying the size parameters. After finding exponents of all size parameters, a standardized moment – rotation curve is plotted for all specimens. Finally, the curve fitting constants C_1, C_2, C_3 of standardized moment – rotation relationship is derived by using the least squares curve fitting procedure.

The revised standardization factor K obtained from the present study based on Frye-Morris [4] procedure is

$$K= t_p^{-1.04}.d_g^{4.20} \tag{3}$$

The curve fitting constants C_1, C_2, C_3 of standardized M-θ_r relationship are listed in Table 4.

Table 4. Curve Fitting Constants for All Endplate Connection Specimens

TEST - ID	C1	C2	C3
EP-1-8x400	-1.00E-11	2.11E-27	6.40E-45
EP-2-8x420	-3.24E-11	3.90E-27	-1.34E-44
EP-5-10x400	6.37E-12	9.90E-28	1.49E-44
EP-4-10x420	-3.48E-11	2.62E-27	2.85E-46
EP-3-10x440	-3.81E-11	2.58E-27	-3.88E-45
EP-6-12x400	4.02E-11	-1.16E-27	3.61E-44
EP-7-12x420	2.49E-11	-3.87E-28	1.20E-44
EP-8-12x440	2.06E-11	9.80E-28	1.03E-44

Therefore the average value of $C_1 = -2.91\text{x}10^{-12}$, $C_2= 1.45\text{x}10^{-27}$, $C_3= 7.83 \text{ x } 10^{-45}$ and the Eq. 1 becomes,

$$\theta_r = -2.91\text{x}10^{-12}(KM)+1.45\text{x}10^{-27}(KM)^3+7.83\text{x } 10^{-45}(KM)^5 \tag{4}$$

This proposed model is checked with the experimental values and with the original Frye-Morris model for different thicknesses of the endplate varying with their bolt spacing. They are given in Figures 19-21. From the comparative study it is found that the original Frye-Morris model prediction overestimates the stiffness for all specimens except for EP-6-12 and shows closer results to specimens EP-1-8, Ep-5-10. The proposed Frye-Morris model equation presents a best fit to all ranges of endplate connections.

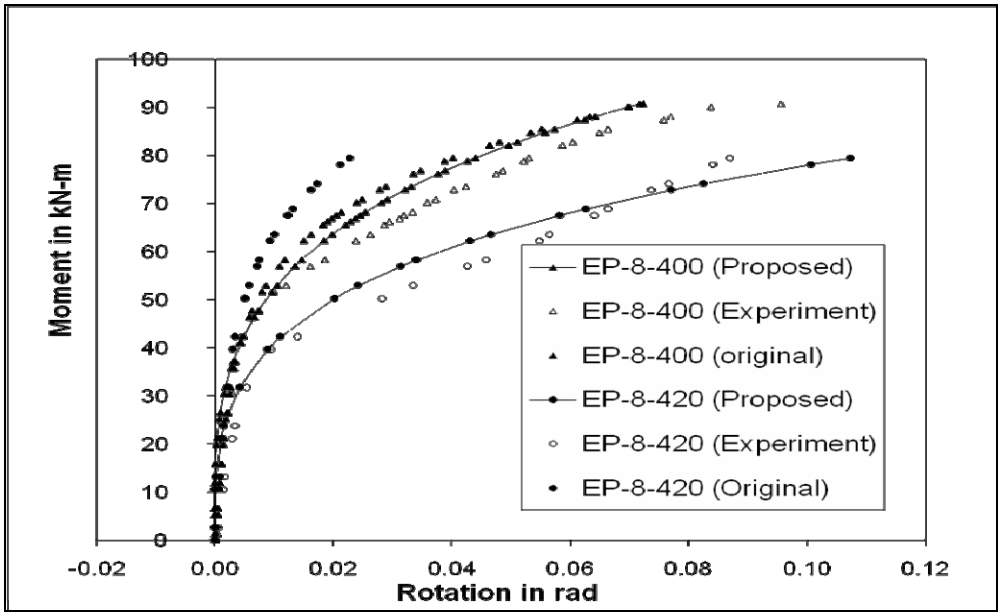

Figure 19. Comparison of M-θ_r Curves of Proposed Model with Experiment and Original Model for All 8mm Specimens

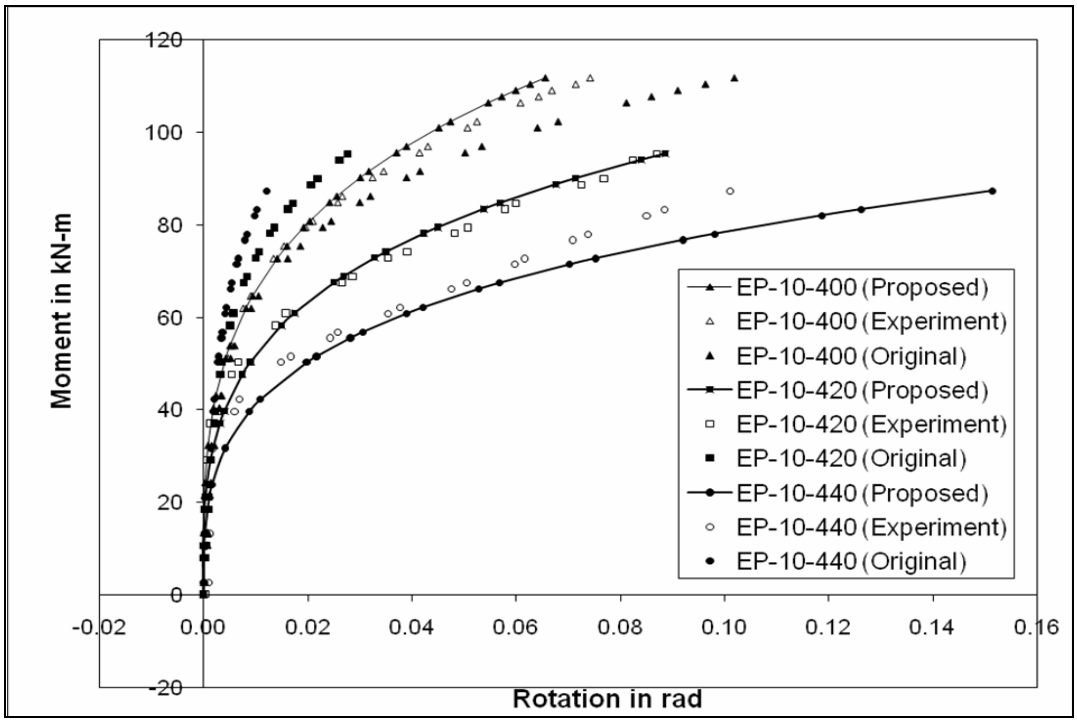

Figure 20. Comparison of M-θ_r Curves of Proposed Model with Experiment and Original Model for All 10 mm Specimens

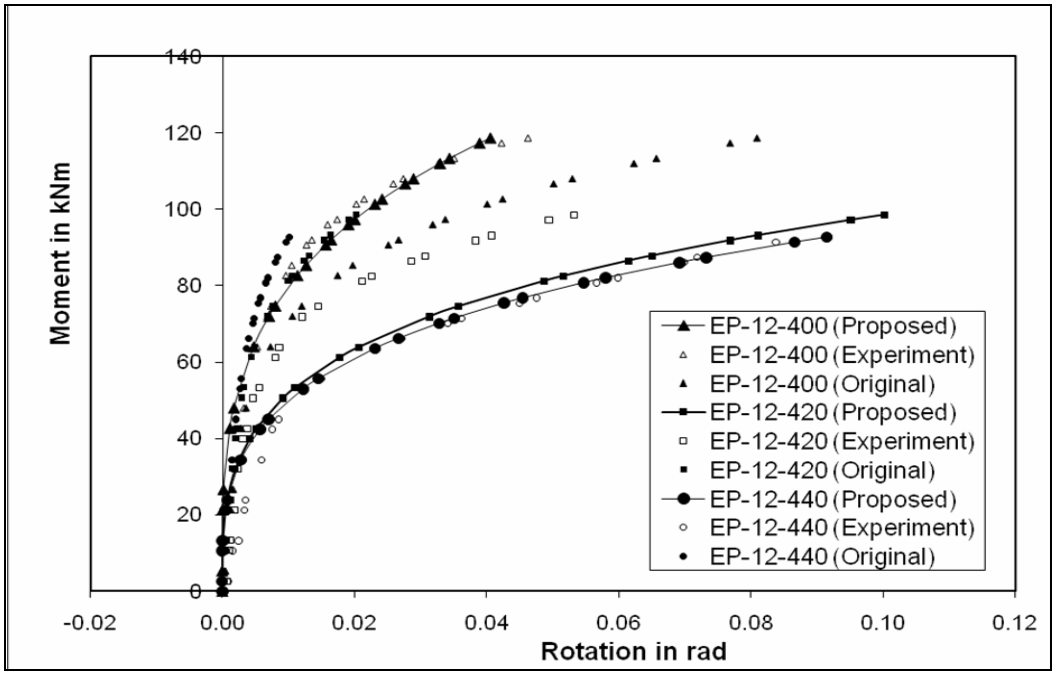

Figure 21. Comparison of M-θ_r Curves of Proposed Model with Experiment and Original Model for All 12 mm Specimens

7. CONCLUSION

From the experimental study the following observations are made.

1. In the case of endplate connections for a particular thickness, it is observed that the initial stiffness reduces with the increase in bolt spacing. It is also observed that the contact opening increases with the increase in bolt spacing.
2. For the same thickness, the load carrying capacity decreases with the increase in bolt spacing and this is due to the increased prying action on the bolts due to increased prying length.
3. For the same bolt spacing, the load carrying capacity increases with the increase in endplate thickness and this increase is provided by the flexural yielding strength of the endplate. As the thickness of the endplate increases, the endplate becomes stiffer and the failure is observed to be by fracture of tension bolt. This is due to the fact that as the thickness of the plate is increased, the tension is directly transferred to the bolts.

Finite element analysis of eight test specimens are carried out using the FE software, ABAQUS and the results are compared with the tests results. The following conclusions are drawn from the numerical study

1. Moment rotation curves obtained from ABAQUS compare reasonably well with those obtained from the tests.
2. Two modes of failure (i) end-plate rupture and (ii) bolt rupture of the connections are observed in the tests as well as in finite element analysis
3. The failure loads obtained from FEM analysis compare within 12% of the loads obtained from the tests

It is observed that the results obtained from the tests compare well with those obtained using the original Frye-Morris model for EP-1-8 and EP-5-10; whereas for all the other specimens, the Frye-Morris model predicts higher stiffness compared with that obtained from the tests. Hence it is concluded that the Frye-Morris model does not represent the different stiffness ranges in the endplate connection. A modified Frye and Morris model has been developed for the moment-rotation behaviour of endplate connection based on the test results. The revised Frye-Morris model is proposed for incorporation in the next revision of IS:800 [17].

ACKNOWLEDGEMENTS

The authors thank Dr. N. Lakshmanan, Director, Structural Engineering Research Centre, Chennai, for his constant support and encouragement. They also thank Dr. Nagesh R. Iyer, Advisor (Management) for his unstinted support. This paper is published with the kind permission of the Director, Structural Engineering Research Centre (SERC), Chennai, India.

REFERENCES

[1] Doughty, R.T. and McGuire, W., "High Strength Bolted Moment Connections", Journal of Structural Division, 1965, Vol. 91, pp. 101-128.

[2] Kato, B. and McGuire, W., "Analysis of T-Stub Flange to Column Connections", Journal of Structural Division, 1973, Vol. 99, pp. 865-888.

[3] Nair, R.S., Birkemoe, P.C. and Munse, W.H., "High Strength Bolts Subjected to Tension and Prying", Journal of Structural Division, ASCE, 1974, Vol. 100, pp. 351-372.

[4] Frye, M. John and Morris, A. Glenn, "Analysis of Flexibility Connected Steel Frame", Canadian Journal of Civil Engineering, 1975, Vol. 2, pp. 280-291.

[5] Packer, J.A. and Morris, L.J., "A Limit State Design Method for Tension Region of Bolted Beam Column Connections", The Structural Engineer, 1977, Vol. 55, No. 10, pp. 446-458.

[6] Krishnamurthy, N., Hung, H.T. and Jeffrey, P.K., "Analytical M-θ Curves for End Plate Connections", Journal of the Structural Division, 1979, Vol. 105, pp. 133-145.

[7] Mann, P. and Morris, J. L., "Limit State of Extended End Plate Connections", Journal of the Structural Division, 1979, Vol. 105, pp. 511-525.

[8] Maxwel, S.M., Jenkins, W.M. and Howlett, J.H., "The Effects of Endplate Thickness on Flush Endplate Connections", Joints in Structural Steel Work, Proceedings of the International Conference on Joints in Steelwork held at Middlesbrough, Cleveland, United Kingdom Pentach Press, London, 1981, pp. 2.49-2.70.

[9] Philips, J. and Packer, J.A., "The Effects of Endplate Thickness on Flush Endplate Connections", Joints in Structural Steel Work, Proceedings of the International Conference on Joints in Steelwork held at Middlesbrough, Cleveland, United Kingdom Pentach Press, London, 1981, pp. 6.77- 6.92.

[10] Zoetemeijer Piet., Bijlaard, S.K., Witteveen, J. and Stark, W.B. Jan., "Welded and Bolted Beam to Column Connections", Journal of the Structural Division, 1982, Vol. 108, No. 2, pp. 433-455.

[11] Tsai, K.C. and Popov, E.P., "Cyclic Behavior of End-Plate Moment Connections", Journal of Structural Engineering, 1990, Vol. 116, No. 11, pp. 2917-2930.

[12] Korol, R.M., Ghobarah, A. and Osman, A., "Behaviour of Extended Endplate Connections Under Cyclic Loading", Engineering Structures, 1990, Vol. 12, pp. 15-27.

[13] Ghobarah, A., Osman, A., and Korol, R.M., "Extended End Plate Connections Under Cyclic Loading: Behaviour and Design", Journal of Constructional Steel Research, 1990, Vol. 16, pp. 253-280.

[14] Foley, M. Christopher and Vinnakota, Sriramulu, "Toward Design Office Moment Rotation Curves for End Plate Beam to Column Connections", Journal of Constructional Steel Research, 1995, Vol. 35, pp. 217-253.

[15] Mofid, M., Mohammadi, M.R.S. and McCabe, S.L., "Analytical Approach on Endplate Connection: Ultimate and Yield Moment", Journal of Structural Engineering, 2005, Vol. 131, pp. 449-456.

[16] Abolmaali, Ali. John, H. Matthys., Mohammed Farooqi and Yeol Choi, "Development of Moment-Rotation Model Equations for Flush End Plate Connections", Journal of Constructional Steel Research, 2005, Vol. 61, pp. 1595-1612.

[17] IS:800 Draft, Code of Practice for General Construction in Steel, Bureau of Indian Standards, New Delhi, 2007.

[18] Hibbit, Karlsson and Sorenson**,** ABAQUS User's Manual, Version 6.6. Pawtucket, 2006, USA.

[19] Maggi, Y.I., Gonclaves, R.M., Leon, R.T. and Rebeiro, L.F.L., "Parametric Analysis of Steel Bolted End-Plate Connections Using Finite Element Modeling", Journal of Constructional Steel Research, 2005, Vol. 61, pp. 689-708.

AN ARTIFICIAL NEURAL NETWORK MODEL FOR PREDICTING THE BEHAVIOUR OF SEMI-RIGID JOINTS IN FIRE

K.S. Al-Jabri [1,*], S.M. Al-Alawi [2], A.H. Al-Saidy [1] and A.S. Alnuaimi [1]

[1] *Department of Civil and Architectural Engineering, College of Engineering, Sultan Qaboos University, Oman*
[2] *Department of Electrical and Computer Engineering, College of Engineering, Sultan Qaboos University, Oman*
**(Corresponding author: E-mail: aljabri@squ.edu.om)*

Received: 9 April 2008; Revised: 14 July 2008; Accepted: 29 July 2008

ABSTRACT: This paper presents an artificial neural networking (ANN) model developed to predict the behaviour of semi-rigid bare-steel joints at elevated temperature. Data for three flush end-plate and one flexible end-plate joints were considered. Sixteen parameters which included geometry of the joint's components, material properties of the joint, joint's temperature and the applied moment were used as the input variables for the model whilst the joint's rotation was the main output parameter. Data from experimental fire tests were used for training and testing the model. In total, fifteen different test results were evaluated with 331 and 61 cases were used for training and testing the developed model, respectively. The model predicted values were compared with actual test results. The results obtained indicated that the model can predict the moment-rotation behaviour in fire with very high accuracy. The coefficients of determination (R^2) for training and validation of the model were 0.964 and 0.956, respectively.

Keywords: Bare-steel, flush end-plate, flexible end-plate, semi-rigid joints, artificial neural network, fire, elevated temperature, rotation

1. INTRODUCTION

Steel loses both its strength and stiffness when subjected to fire. Fire tests on steel structures have shown that the temperature within the joints is lower compared to connecting steel members. This is attributed to the additional material around joints (column, end-plate, concrete slab, etc.) which significantly reduces the temperatures within the connections compared to those at the centre of supported beams. The experimental results on the behaviour of steel connections under fire conditions are relatively recent and limited, partly because of the high cost of the fire tests and the limitations on the size of furnaces used. Only limited joint tests have been performed and they were concentrated on obtaining the moment-rotation relationships of isolated joints (Al-Jabri et al. [1]). Therefore, experimental fire joint tests are not anticipated to be performed on many connection types with various end conditions. It is well known that even nominally 'simple' connections can resist significant moments at large rotation. At the severe deformation of structural members in fire, moments are transferred through the joints to the adjacent members, and hence, they may have a beneficial effect on the survival time of members.

Accurate prediction of the structural behaviour of steel beam-to-column connections, by estimating the local deformations and induced stresses, is necessary to assess the capacity of the connections and prevent their failure. Numerical modeling presents, in principle, an alternative way to predict the response of structural steel joints in fire. Artificial neural network (ANN) modeling is an artificial intelligence-based technique that emulates the human ability to learn from the past experience and derive quick solutions to new problems. The developed ANN-based prediction model can be used by structural engineers to predict the elevated temperature behaviour of similar structural members.

Few ANN models have been developed to predict the connection behaviour at ambient temperature. Stavroulakis and Abdalla [2] and Stavroulakis et al. [3] described a neural network approach for identification and classification of semi-rigid connections in steel structures. The moment-rotation law of the connection was obtained from experimental results by the use of a neural network based on the perceptron model. Then the elastic plastic analysis problem was formulated for the given moment-rotation law as a quadratic programming problem and solved by a neural network based on the Hopfield model. The bi-linear moment-rotation characteristics for minor axis steel connections were predicted by Anderson et al. [4] using ANN. The results from the model were compared with experimental tests in which significant parameters have been varied. The results were found to provide approximations to the experimental response that are satisfactory for use in structural engineering design. Recently, a neural network model was proposed by Demirtas et al. [5] to obtain nonlinear moment-rotation curves for semi-rigid connections. The resulting model was then integrated into a non-linear frame analysis program to obtain nodal displacements and corresponding frame element forces. Results from the analysis were compared with experimental results for a two-storey one-bay frame with semi-rigid connections. Al-Khaleefi et al. [6] reported the possibility of predicting the behaviour of structural members in fire after investigating the fire resistance of concrete filled tubular steel columns using neural networks. The fire resistance of thirty-five hollow steel columns filled with plain concrete was predicted. Results were in good agreement with results obtained from experimental column tests.

This paper presents a new artificial network model developed to predict the behaviour of semi-rigid bare-stee1 unstiffened joints under fire conditions. The developed ANN can be used for similar connections under fire by observing various factors influencing the connection's behaviour such as: (a) geometrical factors (i.e., member sizes), (b) material factors (i.e., strength and stiffness), and (c) loading conditions (i.e., static and fire). The researcher is required to provide the magnitude of these influencing factors as inputs to the neural network and the network will predict the behaviour of the joint based on the combined effects of these factors. This model can be used to predict the rotational capacity of the connection and the contribution of individual components of the connection as well as the contribution of the loading to the overall connection's behaviour without conducting costly fire tests.

2. ARTIFICIAL NEURAL NETWORKS (ANNs)

ANNs are computer programs that are trained in order to recognize both linear and nonlinear relationships among the input and the output variables in a given data set. In general, ANN applications in engineering have received wide acceptance. The popularity and acceptance of this technique stems from ANN features that are particularly attractive for data analysis. These features include handling of fragmented and noisy data; speed inherent to parallel distributed architectures, generalization capability over new data, ability to effectively incorporate a large number of input parameters, and its capability of modeling nonlinear systems.

One of the most common and frequently used ANN paradigm is the Back-propagation paradigm. This supervised learning method was developed by Rumelhart [7] based on the generalization of the least mean square error (LMS) algorithm. The Back-propagation algorithm uses gradient descent search technique to minimize a cost function equal to the mean square difference between the desired and the actual net output. The network is trained by selecting small random weights and internal threshold and then presenting all training data repeatedly by using supervised training technique. The weights are changed till the network reach the desired error level or the cost function is reduced to an acceptable value.

The major building block for any ANN architecture is the processing element or neuron. These neurons are located in one of three types of layers: the input layer (weights), the hidden (bias) layer, or the output (an activation function) layer. The input neurons receive data from the outside environment, the hidden neurons receive signals from all of the neurons in the preceding layer, and the output neurons send information back to the external environment. The neurons in the input layer receive the input signals representing the input parameters which describe the system modelled such as geometrical and material properties of the joint, loading, temperature, etc. The output layer, on the other hand, consists of output neuron representing the predicted results obtained from the ANN modelling such as joint's rotation, internal forces of the joint's components, etc. Between the input and output layers, generally, there is one or more hidden layer. These neurons are connected together by a line of communication called connection. Stanley [8] indicated that the way in which the neurons are connected to each other in a network typology has a great effect on the operation and performance of the network. ANN models come in a variety of typologies or paradigms. Simpson [9] provides a coherent description of 27 different popular ANN paradigms and presents comparative analyses, applications, and implementations of these paradigms.

In the back propagation (BP) architecture, shown in Figure 1, each element or neuron receives input from the real-world environment or from other processing elements, processes this input, and produces a specific output. Generally, many of these processing elements perform their operations at the same time. This parallelism is a unique feature of the ANN that distinguishes it from the serial processing that is usually performed by conventional computer systems. Each neuron has a straightforward assignment. Input coming to the neuron is associated with a weight indicating its strength. In the neuron, the values of the input are multiplied by the corresponding weights and all products are added to obtain a net value (net_i). After summation, the net input of the neurons is combined with the previous state of the neurons to produce a new activation value. Whether the neurons fire or not will depend on the magnitude of this value. For example, each neuron receives inputs $x_1, x_2, \ldots\ldots x_n$, attached with a weight w_i which shows the connection strength for that input for each connection. Each neuron is then multiplied by the corresponding weight of the neuron connection. A bias b_i can be defined as a type of connection weight with a constant nonzero value added to the summation of inputs and corresponding weights u as expressed in Eq. 1.

$$u_i = \sum_{j=1}^{H} w_{ij} x_j + b_i \tag{1}$$

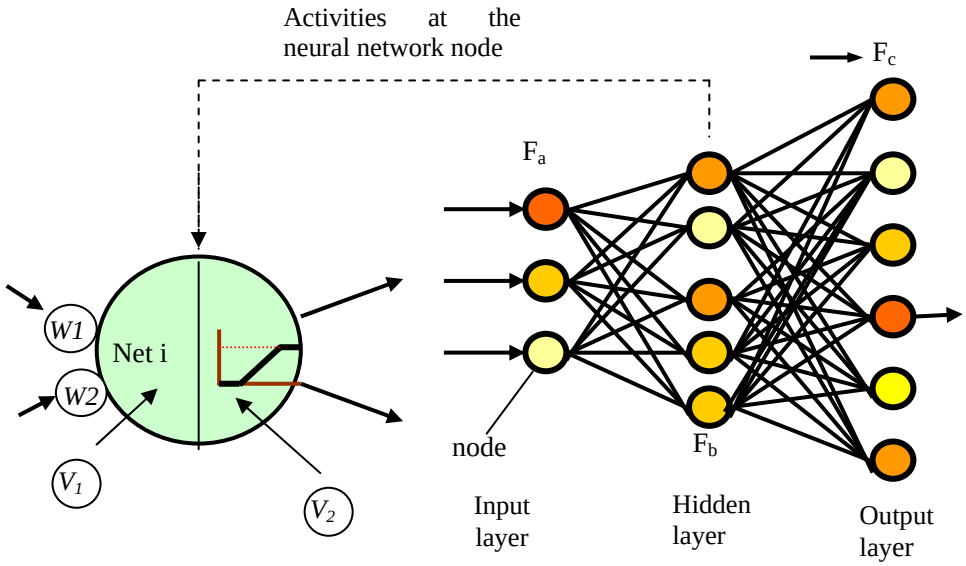

Figure 1. Typical Back-Propagation Architecture

The activation is then passed through an output or a transfer function (fu_i) that generates the actual neuron output. The transfer function modifies the value of the output signal. $f(u_i)$ yielding a value called the unit's "activation", given in Eq. 2.

$$Y_i = f(ui) \quad (2)$$

This function can be either a simple threshold function that only produces output if the combined input is greater than the threshold value, or it can be a continuous function that changes the output based on the strength of the combined input. Activation functions serve to introduce nonlinearity into neural networks, which makes ANNs so powerful (Guzelbey et al. [10-11]). Typical transfer functions employed in building ANN applications include a linear threshold transfer function, step function, sigmoid function, and others. In this work a sigmoid function was used to develop the ANN Model.

Another important network design variable is the learning rate coefficient which represents the degree by which the weights are changed when two neuron are excited. Each time a pattern is presented to the network, the weights leading to a neuron are modified slightly during learning in the direction required to produce a smaller error at the outputs the next time the same pattern is presented. The amount of weight modification is proportional to the learning rate. The value of the coefficient ranges between 0.0 to 1.0, where a value closer to 1 indicates significant modification in weight while a value closer to 0 indicates little modification (Al-Khaleefi et al. [6]).

2.1 ANN Training and Testing

The first and the most critical step in developing an effective ANN model is input and output definition and data preparation. This includes identifying variables of interest, gathering the relevant data and inspecting them for possible errors, missing values, and outliers. Data accuracy is vital for the development of an efficient model that can provide accurate prediction. If incorrect or erroneous data are fed to the model, this will result in incorrect prediction. As the saying goes, "garbage in, garbage out".

Once the ANN model architecture is defined, data are collected and fed to the model. The network is then trained to recognize the relationships between the input and output parameters. The BP algorithm uses the supervised training technique. In this technique, the interlayer connection weights and the processing elements' thresholds are first initialized to small random values. The network is then presented with a set of training patterns, each consisting of an example of the problem to be solved (the input) and the desired solution to this problem (the output). These training patterns are presented repeatedly to the ANN model and the error between actual and predicted results is calculated. Weights are then adjusted by small amounts that are dictated by the General Delta Rule (Rumelhart and McClelland [7]). This adjustment is performed after each completed iteration whenever the network's Computed output is different from the desired output. This process continues until weights converge to the desired error level or the output reaches an acceptable level.

The ANN model can sometimes learn something different than the relationships in the data. It also can memorize the data or part of this data without learning the relationships between variables or trends in the data. Hence, to insure network accuracy and the generalization capability, the network must be tested on a continuous basis and should be monitored during the training and testing operations. The testing operation is performed by passing a separate testing set to the trained ANN model and recording the results. These results are compared to actual results. The trained model is assumed to be successful if the model gives good results for that test set. To

insure that ANN models provide correct prediction or classifications, the prediction results produced by ANN models can be validated against expert predictions for the same cases or it can be validated against the results of other computer programs or experimental tests.

3. KNOWLEDGE REPRESENTATION

The procedure adopted to model the rotational behaviour of semi-rigid joints in fire consists of the following steps:

1. Identification of the major factors that influence the behaviour of semi-rigid joints in fire.
2. Collection of a set of experimental cases with values for these identified factors along with the respective joint's rotation.
3. Coding of the laboratory test cases and corresponding value of rotation obtained based on experiments.
4. Development of ANN model, from the coded cases, which is capable of predicting the rotation of other similar joints in fire.
5. Compare results generated by the model with the corresponding experimental results and identifying the contribution of each input parameter on the overall behaviour of joint at high temperature.

4. GEOMETRY OF THE JOINTS

The cruciform bolted beam-to-column steel joints, tested experimentally by Leston-Jones [12] and Al-Jabri et al. [1], were considered. Two of the joints (Fire1 and Fire2) have the same member sizes but different end-plate thicknesses whilst the third joint (Fire3) has larger member sizes. The first two joints consist of two 254x102UB22 beams connected to a 152x152UC23 column using six M16 bolts and 8 mm (Figure 2) and 12 mm thick flush end-plates for Fires1 and 2, respectively. The third joint (Fire3) comprised a pair of 356 x 171UB51 beams connected to a 254 x 254UC89 column by 10mm thick flush end-plates with eight M20 Grade 8.8 bolts (Figure 3). The fourth joint (Fire4) is a flexible end-plate joint with beam and column sizes similar to Fire3 but the end-plates dimension is different as shown in Figure 4. In total fifteen elevated temperature tests were modelled with 331 and 61 cases were used for training and testing the proposed model, respectively. Table 1 shows the loading level for each test.

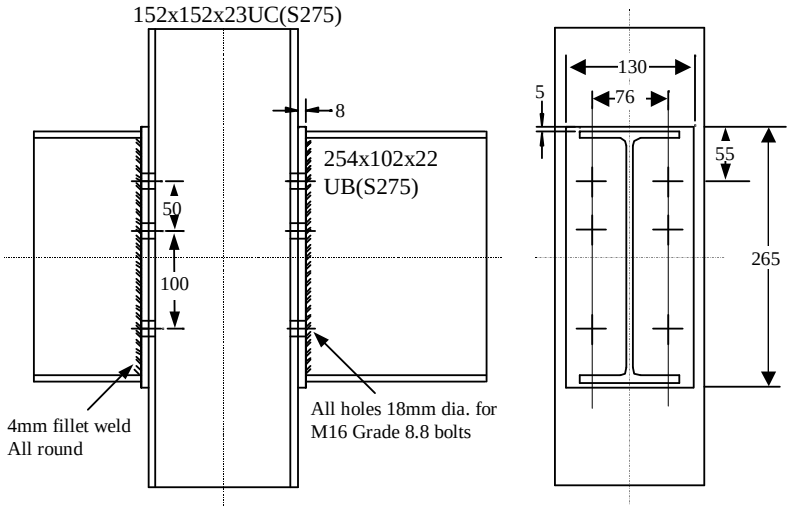

Figure 2. Flush End-Plate Joint Detail for Fire1 Tests (FR1)

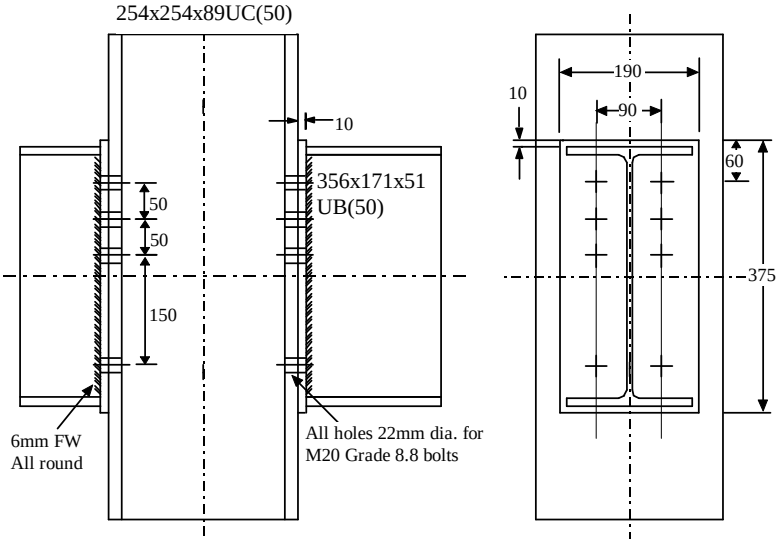

Figure 3. Flush End-Plate Joint Detail for Fire3 Tests (FR3)

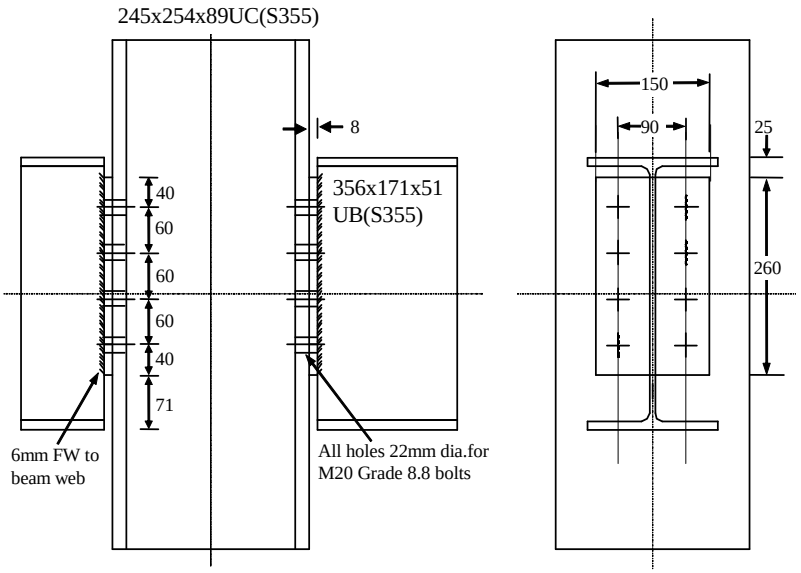

Figure 4. Flexible End-Plate Joint Detail for Fire4 Tests (FR3)

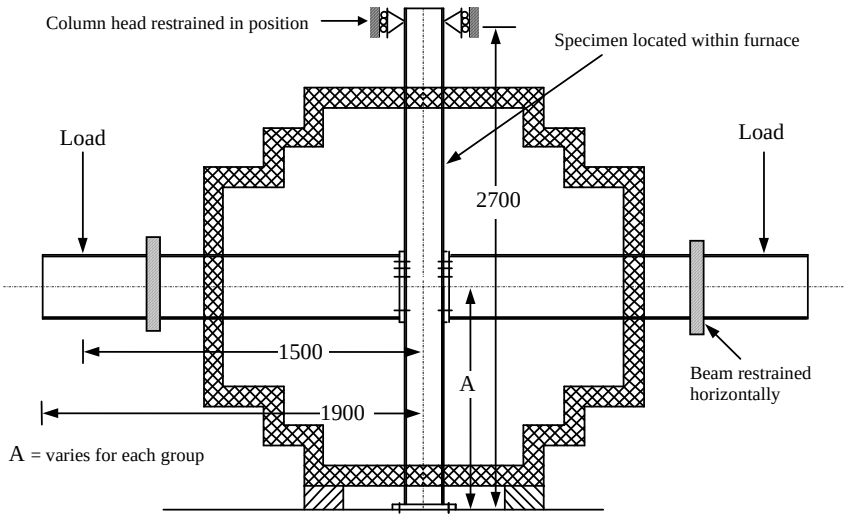

Figure 5. Elevated Temperature Testing Arrangement

Table 1. Level of Loading for Joint Tests

Test		Applied M (kNm):	Average recorded M (kNm):	Comments:
Fire1	FR11	4	4.40	Group 1, Test 1
	FR12	8	8.20	Group 1, Test 2
	FR13	13	13.12	Group 1, Test 3
	FR14	17	17.10	Group 1, Test 4
Fire2	FR21	5	4.9	Group 2, Test 1
	FR22	10	9.3	Group 2, Test 2
	FR23	15	14.4	Group 2, Test 3
	FR24	20	19	Group 2, Test 4
	FR25	25	23	Group 2, Test 4
Fire3	FR31	27	27.4	Group 3, Test 1
	FR32	56	54.8	Group 3, Test 2
	FR33	82	82.1	Group 3, Test 3
	FR34	110	110	Group 3, Test 4
Fire4	FR41	8	8.2	Group 4, Test 1
	FR42	16	16.5	Group 4, Test 2

M = Moment applied at the joint

The fire testing arrangement consisted of a symmetric cruciform arrangement of a single column 2.7m high with two cantilever beams 1.9m long connected either side to the column flanges as shown in Figure 5. All specimens were major axis joints, i.e., beams connected to the column flanges with mild steel end-plates. Tests were performed in a gas-fired portable furnace lined with ceramic fibre specially designed for testing connections. A linear temperature ramp (at a rate of about 10°C per minute) achieving 900°C in 90 minutes was adopted. The instrumentation included clinometers for measuring rotations, displacement transducers, load cells and thermocouples. The experimental elevated-temperature joint tests were conducted by keeping the specimen at a constant load level and increasing the furnace temperature until failure. For all specimens, ambient-temperature material properties were measured using standard tensile coupon tests, and cross-sectional dimensions were recorded prior to testing in the furnace.

5. DEVELOPMENT OF THE ANN MODEL

The ANN model for semi-rigid joints was developed using the back-propagation paradigm. As shown Figure 6, 16 different input parameters were used to model the joint's moment-rotation-temperature response. These included the joint's temperature, the applied moment, material properties such as the yield strength of the joint's components and the geometry of the beams, the column, the end-plates and the bolts.

Having identified the factors that influence the rotational capacity of the joint at elevated temperature, it is necessary to establish the training samples to develop the neural network model. The experimental data were transformed into a numerical scale and coded to generate a set of training and testing data. If the rotational behaviour for a certain joint and the factors affecting this behaviour in fire are known, then it is possible to develop an empirical model for this prediction process.

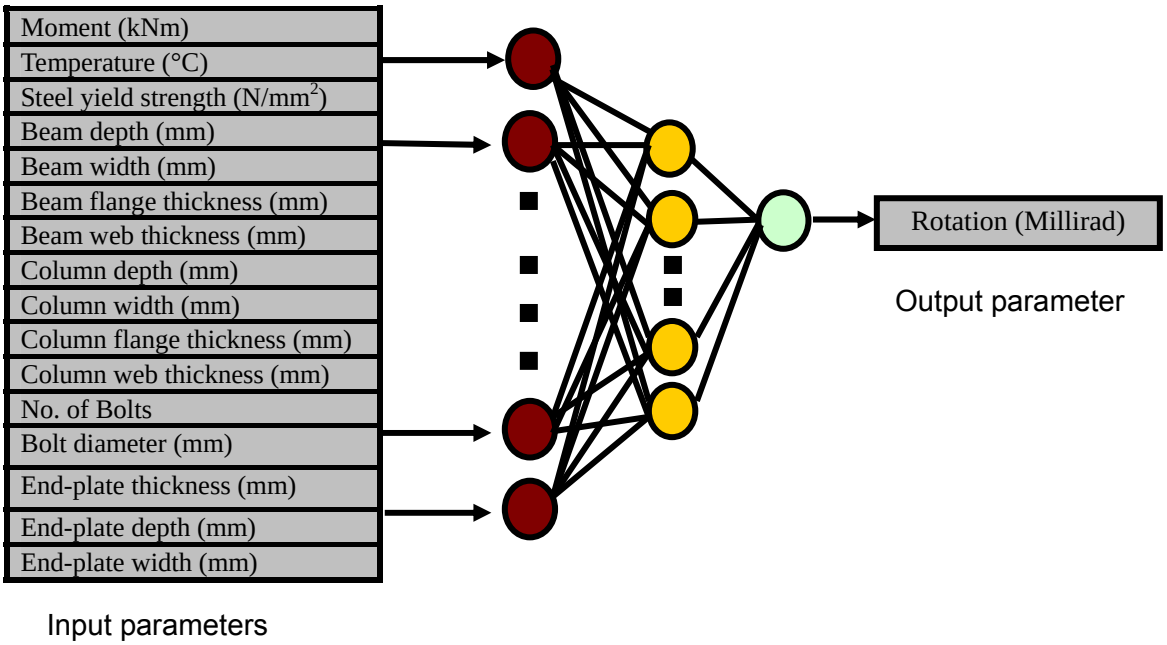

Figure 6. The Architecture of the Developed ANN Models

In the development of this generalized model, a training set consisting of 331 cases was utilized that were obtained from the experimental data and a testing and validation set of 61 cases that were selected randomly from the experimental data. Each training and testing data set contains variations of the 16 variables representing the different situations that could possibly take place as input and its corresponding output. Typical training patterns used as part of the training data set are shown in Table 1. The ANN model used in each case consists of 16 input nodes representing the input variables, while the output node is one representing the rotation as shown in Figure 6.

To produce a successful model, it is necessary to have a sufficient number of training cases in order to enable the ANN model to fit a continuous function to the training data. Further more, the number of training points that are needed to develop an accurate continuous model depends on other factors such as the complexity of the solution model being modelled, stochastic content of the data in which adequate training cases are required to prevent bias due to random fluctuations and the number of input variables (Al-Khaleefi et al. [6], Garson [13]).

A small learning rate of 0.4 was adopted for the current investigation since larger learning rates have been found in some cases to lead to oscillations in weight changes resulting in never ending learning process. In order to achieve an effective learning without oscillation, it is useful to make the weight change as a function of the previous weight change. This weight change is represented by the momentum coefficient. The modelling process was performed satisfactorily with a momentum coefficient value of 0.6.

The factors that provide the power of the internal representation in capturing the non-linear relationship between the input and output parameters are the number of hidden layer(s) and the number of hidden neurons in the hidden layers. Determining the number of hidden layers to use and the appropriate number of neurons to include in each hidden layer is not an exact science. Research in this area (Garson [13], Goh [14], Hecht-Nielsen [15]) proved that one or two hidden layers with an adequate number of neurons are sufficient to model any solution surface of practical interest. Therefore, a larger number of hidden layers and hidden neurons provides a good mean for developing a more effective network. However, the addition of more hidden neurons increases the number of undetermined parameters (weights and biases) associated with the network. A large

number of training examples is then needed to solve these parameters and get a good approximation of the problem domain. When too few training examples are provided, the network will try to memorize, resulting in poor generalization (Al-Khaleefi et al. [6]). In order to provide a good approximation over the problem domain, it should be insured that the number of training pairs should be more than the number of undetermined parameters which are the weights and biases associated with the ANN approximations (Carpenter and Hoffman [16]). In this study, one hidden layer with 8 hidden neurons was found adequate to give satisfactory results.

6. RESULTS AND DISCUSSION

The experimental results from the fifteen different tests conducted on the four bare-steel joints were divided into a training set (331 cases) and a testing set (61 cases) which gives a total number of 392 cases that considered when developing the ANN model. The testing set (which constitutes about 15% of the data) was extracted randomly from the collected data to ensure that the developed ANN model has the capability of predicting rotational behaviour of the joints to a good degree of accuracy. The training process was performed using the NeuroShell® simulator [17]. Sixteen input neurons and one output neuron with eight hidden neurons constitute the neural network arrangement for the problem. After several adjustments to the different network parameters and after completing 12417 iterations, the network converged to a threshold of 0.0001 in less than 5 min. with a learning rate of 0.4, a momentum value of 0.6.

Table 2 a provides a comparison between the experimental results and the ANN generated output for some cases in the training set whereas Table 2b shows a comparison between the experimental results and the ANN predicted output for selected cases in the testing set. It can be seen from Table 2 that the developed model could capture the decision process very closely. The same trend was observed in the data which is not presented in Table 2.

The trained model predictions were in good agreement with the actual experimental results as demonstrated by Figure 7, hence, producing R^2 value of 0.9639. These results indicate that approximately more than 96% of the variation in the rotation values predicted could be explained by the 16 selected input variables and the experimental data used for model development.

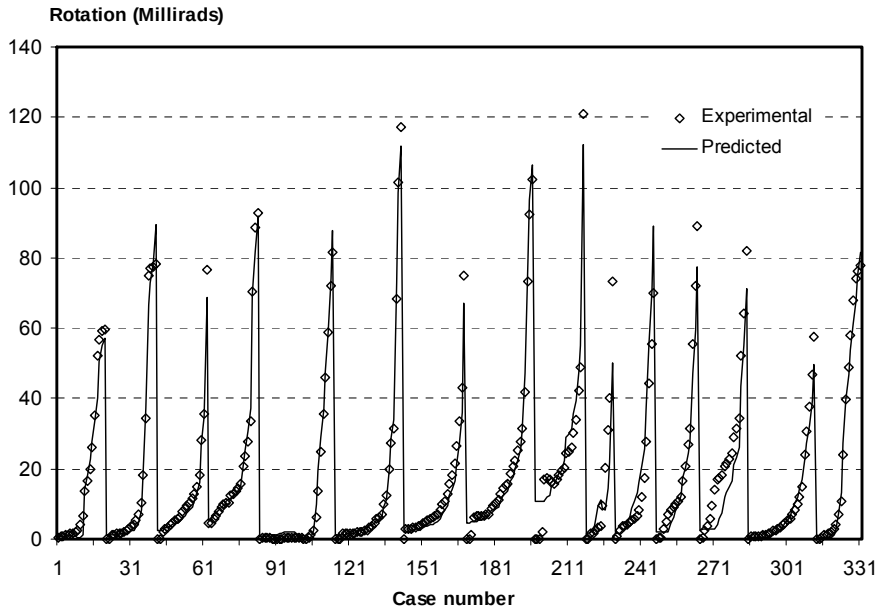

Figure 7. Comparison between Predicted and Experimental Results for the Training Set Data

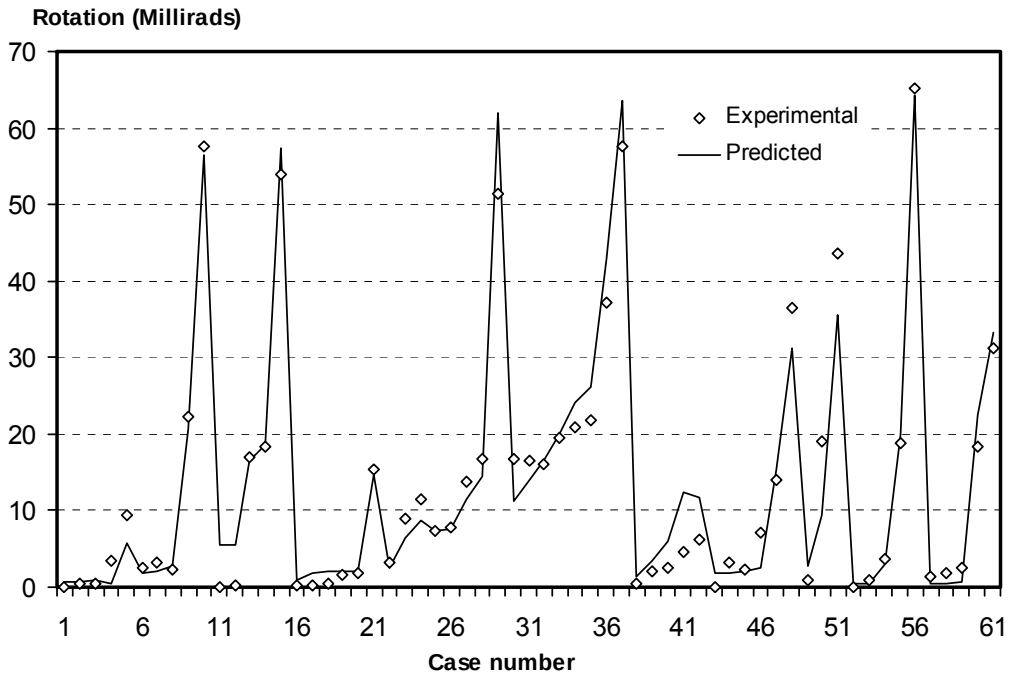

Figure 8. Comparison between Predicted and Experimental Results for the Testing Set Data

Having trained the network successfully, the next step is to test the network in order to judge its performance and to determine whether the predicted results confirm with the actual results. The ANN model can sometimes learn something different than the relationships in the data. It also can memorize the data or part of this data without learning the relationships between variables or trends in the data. Hence, to insure network accuracy and the generalization capability, the network must be tested on a continuous basis and should be monitored during the training and testing operations. The testing operation is performed by passing a separate testing set to the trained ANN model and recording the results. These results are compared to actual or experimental results. The trained model is assumed to be successful if the model gives good results for that test set or validation set. Using the testing and validation set of 61 cases that were extracted randomly from the experimental data for the model; the testing operations were then performed on the model separately. The results were compared with the actual experimental results. The statistical analysis of these results indicates that the R^2 value for the testing set was 0.9562 as shown in Figure 8. This high generalization capability indicates that the ANN model developed in this work can be used to model and predict the relationship accurately based on the given input variables. However it should be noted from Figures. 7 and 8 that at very low rotations the developed ANN predicting higher rotations that the experimental ones while at very large rotational levels lower values of rotation was predicted compared to experimental results. This variation was observed in both training and testing sets respectively. This discrepancy between the experimental and predicted rotations will not affect the reliability of the model since practically the actual behaviour of the joint can rarely undergo very large levels of rotation beyond the levels closely predicted by the model even at very high temperatures.

Table 2. Comparison between Predicted Results from the Neural Network Model Generated vs. Experimental Rotations on Some Training and Testing Cases

Case #	Experimental rotation	ANN generated rotation
(a) training cases		
2	0.71	0.92
15	26.22	27.92
20	59.55	57.25
35	10.22	8.33
52	8.05	6.17
59	18.33	16.28
73	12.98	12.28
80	33.49	37.32
89	0.12	1.23
109	24.84	28.98
122	1.55	1.62
142	117.1	111.6
161	12.71	9.58
186	15.9	13.79
201	16.83	10.65
225	9.36	8.57
246	70.08	88.86
288	0.75	0.41
300	4.52	4.46
312	57.66	49.76
325	39.72	39.79
331	77.89	81.43
(b) testing cases		
3	0.38	0.83
7	3.21	2.16
10	57.54	56.39
16	0.17	0.83
21	15.36	14.65
27	13.71	11.53
32	16.01	16.5
36	37.26	42.85
41	4.62	12.4
48	36.4	31.3
55	18.84	19.88
61	31.17	33.37

Table 3. Percent Contribution of the Input Variables to the Rotation in the Three Models

Joint's Component	Input parameter	% Contribution	RANK
	Moment (kNm)	33.04	1
	Temperature (°C)	28.65	2
	Depth	1.47	16
Beam	Width	1.73	14
	Flange thickness	1.73	13
	Web thickness	1.80	10
	Depth	1.82	8
Column	Width	2.02	6
	Flange thickness	1.80	11
	Web thickness	1.87	9
	No. of Bolts	1.55	15
Bolts	Bolt diameter	1.92	7
	Thickness	3.58	5
End-plate	Depth	5.92	4
	Width	9.35	3
	Steel yield strength	1.75	12
TOTAL	100		

To find the percent contribution of each of the input variables with respect to the output variables, the partitioning method of the connection weights of the network (Garson [13], Goh [14]) was used. It was found that the highest contribution is due to the moment (33.04%), temperature (28.65%), and end-plate width (9.35%), depth (5.92%), and thickness (3.58%). These results, as shown in Table 3, clearly indicate that the temperature, the moment and the geometries of the end-plate are important factors in determining the effect elevated temperature on the degree of rotation.

7. CONCLUSIONS

This paper presented an artificial neural network (ANN) model developed to predict the rotational behaviour of semi-rigid joints in fire. Data from three flush end-plate and flexible end-plate bare-steel joints were modelled and results from fifteen different tests were evaluated. Data from these tests were used for training and testing the neural network model. The results obtained from the model compared very closely with the experimental results with R^2 value of 0.964 and 0.956 for training and testing sets, respectively demonstrating the capability of the ANN simulation techniques in predicting the behaviour of semi-rigid joints in fire with high accuracy. Results also showed that the applied moment, temperature and end-plate geometry have considerable effect on the rotation of joints in fire more than the other input parameters studied. The described model can be modified to study other important parameters that can have considerable effect on the behaviour of joints at elevated temperatures.

REFERENCES

[1] Al-Jabri, K.S., Burgess, I.W., Lennon, T. and Plank, R.J., “Moment-Rotation-Temperature Curves for Semi-Rigid Joints”, Journal of Constructional Steel Research, 2005, Vol. 61, pp. 281-303.

[2] Stavroulakis, G.E. and Abdalla, K.M., “A Systematic Neural Network Classificator in Mechanics. An Application in Semi-rigid Steel Joints”, International Journal for Engineering Analysis and Design, 1994, Vol. 1, pp. 279-292.

[3] Stavroulakis, G.E., Avdelas, A.V., Abdalla, K.M. and Panagiotopoulos, P.D., “A Neural Network Approach to the Modelling, Calculation and Identification of Semi-rigid Connections in Steel Structures”, Journal of Constructional Steel Research, 1997, Vol. 44, No. 1-2, pp. 91-105.

[4] Anderson, D., Hines, E.L., Arthur, S.J. and Eiap, E.L., “Application of Artificial Neural Networks to the Prediction of Minor Axis Steel Connections”, Computers and Structures, 1997, Vol. 63, No. 4, pp. 685-692.

[5] Dermitas, B., De Santiago, E. and O'leary, J.R., “Classification of Steel Semi-rigid Connections by Neural Networks”, Structures 2004-Building on the Past: Securing the future, 2004. Nashville, Tennessee, USA.

[6] Al-Khaleefi, A.M., Terro, M.J., Alex, A.P. and Wang, Y., “Prediction of Fire Resistance of Concrete Filled Tubular Steel Columns using Neural Networks”, Fire Safety Journal, 2002, Vol. 37, pp. 339-352.

[7] Rumelhart, D. and McClelland, J., “PDP Research Group. Parallel Distributed Processing, Explorations in the Microstructure of Cognition, Vol. 11: Foundations”, Cambridge, MA, MIT Press/Bradford Books, 1988.

[8] Stanley, J., “Introduction to Neural Networks”, 3rd Edition, Sierra Madre, California Scientific Software, California, 1990.

[9] Simpson, P.K., “Artificial Neural Systems: Foundations, Paradigms, Applications, and Implementations”, 1st Edition, Elmsford, NY, Pergamon Press, Inc., 1990.

[10] Guzelbey, I.H., Cevik, A. and Gögüs, M.T., "Prediction of Rotation Capacity of Wide Flange Beams using Neural Networks", Journal of Constructional Steel Research, 2006, Vol. 62, pp. 950-961.

[11] Guzelbey, I.H., Cevik, A., and Erklig, A., "Prediction of Web Crippling of Cold-Formed Steel Sheetings using Neural Networks", Journal of Constructional Steel Research, 2006; Vol. 62, pp. 962-973.

[12] Leston-Jones, L.C., "The Influence of Semi-rigid Connections on the Performance of Steel Framed Structures in Fire", PhD, Thesis, University of Sheffield, UK, 1997.

[13] Garson, G.D., "Interpreting Neural Network Connection Weights", AI Expert; 1991, Vol. 6, No. 7, pp. 47-51.

[14] Goh, A.T.C., "Back-Propagation Neural Networks for Modelling Complex Systems", Artificial Intelligence in Engineering, 1995, Vol. 9, pp. 143-151.

[15] Hecht-Nielsen, P., "Theory of the Back Propagation Neural Network", Proceeding of International Conference on Neural Networks. Washington D.C., 1989, pp. 593-605.

[16] Carpenter, W.C. and Hoffman, M.E., "Training Back Prop Neural Networks, AI Expert, 1995, Vol. 10, pp. 30–33.

[17] NeuroShell™., "Neural Network Shell Program", 4th Edition. Ward Systems Group, Inc., Frederick, MD, USA, 1991.

ELASTO-DYNAMIC INSTABILITY OF SHALLOW PIN-ENDED STEEL ARCHES UNDER CENTRAL STEP LOADING

Yong-Lin Pi [1,*], Mark Andrew Bradford [1] and Shuguo Liang [2]

[1] *Centre for Infrastructure Engineering and Safety, School of Civil and Environmental Engineering UNSW, Sydney, NSW 2052, Australia*
[2] *School of Civil Engineering, Wuhan University, Wuhan 430071, P.R. China*
**(Corresponding author: E-mail: y.pi@unsw.edu.au)*

Received: 23 April 2008; Revised: 6 August 2008; Accepted: 11 August 2008

ABSTRACT: When a shallow steel arch is subjected to in-plane central step loading, the arch will oscillate about an equilibrium position due to the kinetic energy imparted to the arch by the load. If the load is sufficiently large, the motion of the arch may reach an unstable equilibrium configuration that leads to elasto-dynamic instability of the arch. This paper presents a study of the in-plane elasto-dynamic instability of a shallow pin-ended circular arch under central step loading with infinite duration. The principle of conservation of energy is used to establish the criterion for elasto-dynamic instability, and analytical solutions for the lower and upper elasto-dynamic instability loads of the arch are obtained. It is found that the elasto-dynamic instability loads of a shallow pin-ended arch under central step loading with infinite duration are lower than its elasto-static counterparts.

Keywords: Bifurcation buckling, circular arch, dynamic instability, elastic, energy criterion, limit instability, step loading

1. INTRODUCTION

A shallow steel arch that is subjected to an in-plane central static load may buckle in the plane of loading in an elastic bifurcation mode or in an elastic limit instability mode when the load reaches a critical value. It has been found [1-5] that the prebuckling deformations have significant effects on the instability of a shallow arch and that classical buckling theory cannot predict the instability load of shallow arches correctly. Analytical solutions for limit instability and bifurcation buckling loads for shallow arches under a central load have been obtained [1]. When the central load is suddenly applied to the arch at time $t = 0$ as a step load (Figure 1), the load will impart kinetic energy to the arch, and dynamic effects of the step loading on the instability of the arch have to be considered. When the step load is sufficiently small, it causes the arch to oscillate about a stable equilibrium position and the amplitudes of oscillation are sufficiently small. If this load is sufficiently large, the motion of the arch may reach an unstable equilibrium position, which may then induce elasto-dynamic buckling of the arch.

Commonly, the equations of motion of an arch are solved numerically for various values of the load parameter to obtain the response of the system [6-12]. The load parameter at which there exists a large increase of the transient response is considered as the critical one [6]. The major merit of this method is that it considers the dynamic effects directly and intuitively. However, when this method is applied to a continuum such as a shallow arch, a number of approximations have to be made. Power series expansion of the displacement components are usually used to obtain approximate solutions for the elasto-dynamic instability [13-14]. For convenience in obtaining dynamic solutions, the effects of the transverse deformation on the axial deformation are usually ignored [6-14]. However, the effects of transverse (normal) deformations on axial deformations in a circular shallow arch are significant and so should be considered, particularly when exact closed form solutions are sought, as was pointed out in [1-5]. In addition, most investigations of the dynamic buckling of shallow arches using this method have focused on sinusoidal arches under loads distributed as half sine-waves [6, 7, 9, 10].

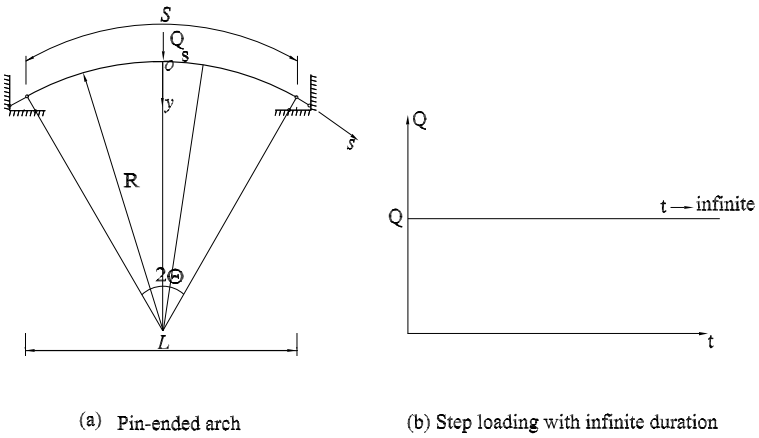

(a) Pin-ended arch (b) Step loading with infinite duration

Figure 1. Arch and Load

The total energy phase plane of a structural system is also used to predict the elasto-dynamic instability of arches [8, 9, 11, 12]. The motion of the arch can be represented by a trajectory in a functional phase space which can be taken as a Euclidean space of infinite dimensions. Critical conditions are related to the characteristics of the system's phase plane or space, and the emphasis is on establishing sufficient conditions for stability and for instability [6-9].

The principle of conservation of energy [9, 15-17] can be applied to the elasto-dynamic instability analysis of a conservative system. The major merit of the method is that it is devoted to finding the criterion which allows the elasto-dynamic buckling load to be determined without actually having to solve the equations of motion per se.

In this paper, attention will be directed to using the principle of energy conservation to investigate the elasto-dynamic buckling of shallow pin-ended circular steel arches that are subjected to a central step loading of infinite duration as shown in Figure 1.

2. ENERGY CRITERION FOR ELASTO-DYNAMIC INSTABILITY

2.1 Equation of Motion Approach

In this section, a one degree-of-freedom idealized arch system shown in Figure 2 is used to establish the energy criterion for dynamic instability. The system consists of two rigid bars with the same length L pinned together and the other ends of the two bars are pin-ended or simply supported (Figure 2). A mass m is attached to the pin-joint and a linear translational spring is connected to the pin-joint with the dimensions as shown in Figure 2. The stiffness of the spring is k. The system is assumed to have an initial angle θ_0. The motion of the system under a sudden horizontal load Q can be described by the rotation angle θ.

Before developing the energy criterion for dynamic instability, the equation of motion approach is used to investigate the dynamic instability of the one degree-of-freedom arch system. The equation of motion for the system can be obtained in a dimensionless form as

$$\ddot{\theta}(\tau)+\left(1-\frac{\sqrt{1+\sin\theta(0)}}{\sqrt{1+\sin\theta(\tau)}}\right)\cos\theta(\tau)-\bar{Q}\sin\theta(\tau)=0\,, \tag{1}$$

where $\ddot{\theta} = \partial^2\theta/\partial\tau^2$ is the dimensionless angular acceleration of the system, and the dimensionless time parameter τ is defined by $\tau = t\sqrt{k/m}$, and the dimensionless load $\bar{Q}$ is defined by $\bar{Q} = 2Q/kL$ (Figure 2), in which *t* is the time.

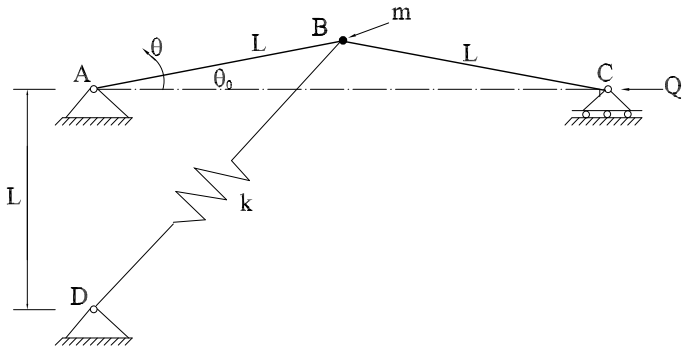

Figure 2. One Degree-of-Freedom System

The initial value problem given by Eq. 1 can be solved by numerical schemes such as the Runge-Kutta procedure when the initial conditions at $\tau = 0$ are given. For example, when the initial rotation angle $\theta(0)$ = 0.008 and the initial angular velocity $\dot{\theta}(0) = 0$ at $\tau = 0$ are assumed, the results that are obtained for the dimensionless load $\bar{Q}$ = 0.4000, 0.4100, 0.4153, and 0.4154 are shown in Figure 3 as variations of the rotational angular response $\theta(\tau)$ with the dimensionless time τ. It can be seen from Figure 3 that when the load $\bar{Q}$ = 0.4000, 0.4100, or 0.4153 is suddenly applied, the motion of the system is simply oscillatory with small amplitudes. The oscillation takes place between the initial position $\theta(0)$ = 0.008 and a maximum amplitude of $\theta(\tau)$. When the load $\bar{Q}$ = 0.4154 is suddenly applied, the amplitude of the motion of the system becomes so large that an escaping motion, i.e. dynamic instability of the system, occurs as shown in Figure 3.

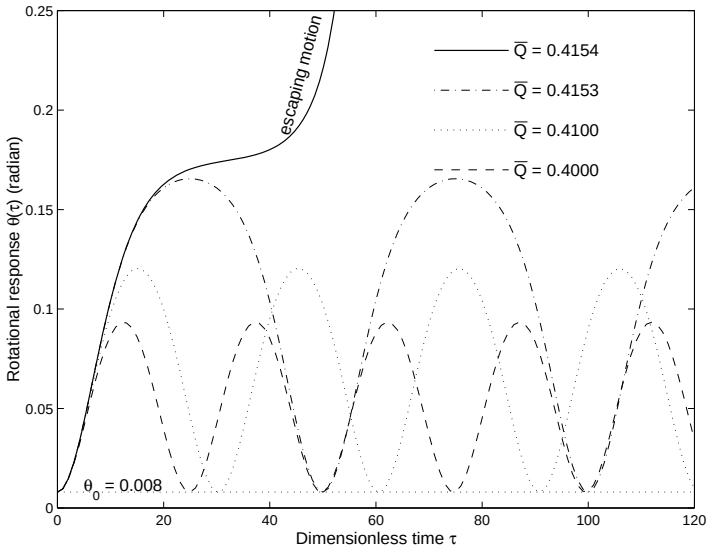

Figure 3. Variations of the Rotational Response with Dimensionless Time

Variations of the maximum response amplitude $\theta_{\max}$ with the dimensionless load $\bar{Q}$ are shown in Figure 4. It can be seen that there is large jump in the maximum amplitude $\theta_{\max}$ at $\bar{Q}$ = 0.4154. According to the Budiansky-Roth criterion [6], the dynamic buckling load is estimated to be $\bar{Q}$ = 0.4154.

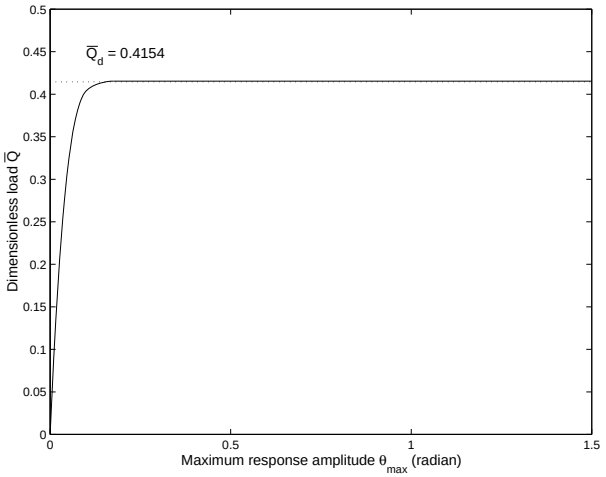

Figure 4. Variations of the Maximum Amplitude $\theta_{\max}$ with the Dimensionless Load $\bar{Q}$

2.2 Energy Criterion for Elasto-Dynamic Instability

Although the equation of motion approach can be used with numerical methods to deal with a continuum subjected to a number of initial conditions, calculations in this approach require an excessive amount of time, which often makes its application very difficult. In addition, the accuracy of this approach often depends on the number of degrees-of-freedom of the reduced system and on the accuracy of the numerical method adopted [13-14].

For a dynamic instability analysis, what is actually needed is to establish the critical states for the instability and so the complete dynamic solution is usually not needed. Herein, an effort will be devoted to finding the criterion that makes it possible to determine the dynamic instability load without actually having to solve the equations of motion for the arch system. A dynamic load generally is one whose magnitude, direction, or point of application varies with time, and it is difficult to solve the dynamic instability problem of a structure analytically under a general dynamic load. This paper concentrates only on step loading with infinite duration, which is a special form of dynamic loading and is suddenly applied at the time $t = 0$.

Because the structure and the step load of infinite duration form a conservative system, the total energy of the system must satisfy the principle of energy conservation, i.e.

$$\bar{E}\left(\dot{\theta},\theta\right)=\bar{T}\left(\dot{\theta}\right)+\bar{U}\left(\theta\right)=\text{constant}, \tag{2}$$

where $\bar{E}\left(\dot{\theta},\theta\right)$ is the dimensionless total energy, $\bar{T}\left(\dot{\theta}\right)$ is the dimensionless kinetic energy of the system and is given by

$$\bar{T}\left(\dot{\theta}\right)=\frac{m[L\dot{\theta}(t)]^2}{2kL^2}=\frac{1}{2}[\dot{\theta}(\tau)]^2, \tag{3}$$

and $\bar{U}(\theta)$ is the dimensionless total potential energy of the system and is given by

$$\bar{U}(\theta)=\left(\sqrt{1+\sin\theta}-\sqrt{1+\sin\theta_0}\right)^2-\bar{Q}(\cos\theta_0-\cos\theta)\,. \tag{4}$$

The necessary conditions for extremes of the total energy $\bar{E}\left(\dot{\theta},\theta\right)$ are given by

$$\partial\bar{E}\left(\dot{\theta},\theta\right)/\partial\dot{\theta}=\partial\bar{T}\left(\dot{\theta}\right)/\partial\dot{\theta}=0\,, \tag{5}$$

and

$$\partial\bar{E}\left(\dot{\theta},\theta\right)/\partial\theta=\partial\bar{U}\left(\theta\right)/\partial\theta=0\,. \tag{6}$$

The condition given by Eq. 5 leads to

$$\dot{\theta}(\tau)=0\,. \tag{7}$$

The value of the total energy $\bar{E}\left(\dot{\theta},\theta\right)$ of the system is determined by the initial condition before it is subjected the step loading. At $t=0$, it is assumed that the system is free from loading and is at rest, and so $\dot{\theta}(0)=0$ and the displacement $\theta(0)=\theta_0$. In this case, the total energy $\bar{E}\left(\dot{\theta}(0),\theta(0)\right)=0$ at $t=0$. Because of the principle of energy conservation, for $t>0$

$$\bar{E}\left(\dot{\theta},\theta\right)=\bar{T}\left(\dot{\theta}\right)+\bar{U}\left(\theta\right)=\bar{E}\left(\dot{\theta}(0),\theta(0)\right)=0\,. \tag{8}$$

Substituting Eqs. 3 and 7 into Eq. 8 leads to

$$\bar{U}(\theta)=0\,, \tag{9}$$

which indicates that vanishing of the total potential energy is a necessary condition for extremes of the total energy.

Eq. 6 leads to another necessary condition for extremes of the total energy as

$$\bar{Q}=\frac{\left(\sqrt{1+\sin\theta}-\sqrt{1+\sin\theta_0}\right)\cos\theta}{\sin\theta\sqrt{1+\sin\theta}} \tag{10}$$

which is also the condition for the static equilibrium configurations of the system.

Variations of the total potential energy $\bar{U}(\theta)$ with rotation angle $(\theta-\theta_0)$ are shown in Figure 5, where A_i and B_i (i = 1, 2, 3, 4) are the equilibrium positions obtained by setting $\partial\bar{U}/\partial\theta=0$. Because the kinetic energy $\bar{T}\left(\dot{\theta}\right)$ of the system is a positive definite function of the velocity $\dot{\theta}$ and the system is at rest at t = 0 prior to loading, motion of the system is possible when the total potential energy $\bar{U}(\theta)$ is non-positive and so the principle of energy conservation given by Eq. 8

holds. It can be seen from Figure 5 that for loads $\bar{Q} = 0.4000$ or 0.4100, the total potential energy $\bar{U}(\theta) < 0$ at a stable equilibrium position A_i, so the principle of energy conservation given by Eq. 8 holds and the system will oscillate about A_i. However, the total potential energy of the system $\bar{U}(\theta) > 0$ at the unstable equilibrium position B_i, so the principle of energy conservation given by Eq. 8 is violated and the oscillation of the system cannot reach the unstable equilibrium position B_i. When the total potential energy at an unstable equilibrium position vanishes ($\bar{U}(\theta) = 0$), the principle of energy conservation given by Eq. 8 holds if the kinetic energy also vanishes. In this case, the oscillation of the system can reach the unstable equilibrium position and so dynamic buckling is possible. The dynamic buckling load and the corresponding rotation angle can then be obtained by solving $\bar{U}(\theta) = 0$ given by Eq. 9 and $\partial \bar{U}(\theta)/\partial\theta = 0$ given by Eq. 10 simultaneously as $\bar{Q}_d = 0.4154$ and θ = 0.174698 (B_3 in Figure 5), which is the same as that obtained from the equation of motion.

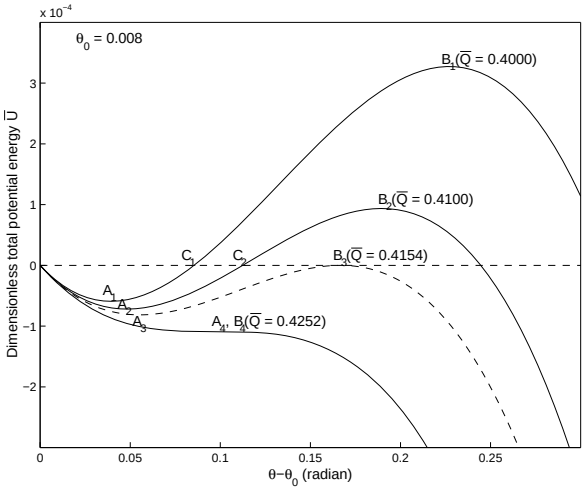

Figure 5. Variation of Energy with Rotation

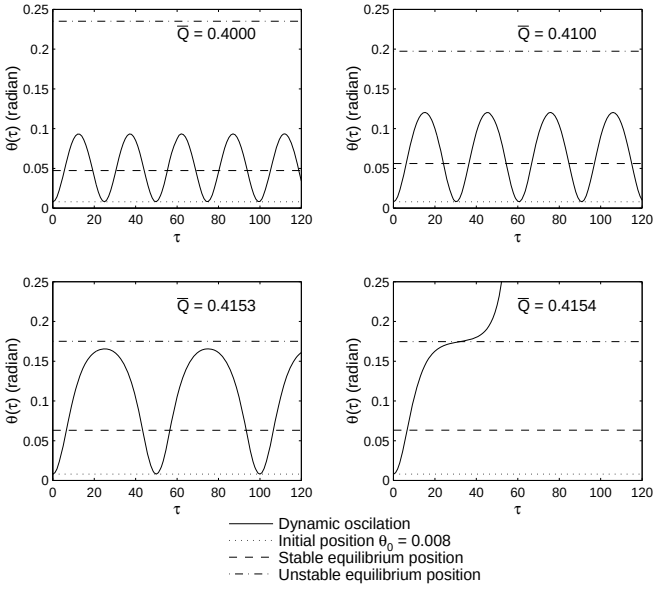

Figure 6. Dynamic Responses and Static Equilibrium

The static equilibrium positions of the arch system given by Eq. (10) are compared with its dynamic responses given by Eq. 1 in Figure 6 for loads $\bar{Q} = 0.4000$, 0.4100, 0.4153, and 0.4154. It can be seen that when the load $\bar{Q} = 0.4000$, 0.4100 and 0.4153, the arch system oscillates through the stable equilibrium positions θ = 0.047307, 0.056118, and 0.063097 respectively and that the oscillations cannot reach the unstable equilibrium positions θ = 0.235087 (for $\bar{Q} = 0.4000$), 0.197357 (for $\bar{Q} = 0.4100$), and 0.175143 (for $\bar{Q} = 0.4153$). However, when the load $\bar{Q} = 0.4154$, the arch system moves through the stable equilibrium position θ = 0.06326 first, and then reaches the unstable equilibrium position θ = 0.174698 and escaping motion, i.e. dynamic instability of the system occurs.

If the load is slowly applied to the system, it can be considered as a static load and the system may buckle in a static instability mode. The static instability load of the system needs to satisfy

$$\frac{\partial^2 \bar{U}}{\partial \theta^2} = 0. \tag{11}$$

Solving Eqs. 10 and 11 simultaneously yields the static instability load as $\bar{Q}_s = 0.4252$ (Figure 5) which is higher than the dynamic instability load $\bar{Q}_d = 0.4154$.

3. DIFFERENTIAL EQUATIONS OF MOTION FOR SHALLOW STEEL ARCHES

It is assumed that the dynamic response of the arch is undamped and so the Lagrangian $\mathcal{L}$ of the shallow pin-ended steel arch and load system can be expressed as

$$\mathcal{L} = T - U, \tag{12}$$

where T is the kinetic energy of the system given by

$$T = \frac{1}{2}\int_V m\left(\dot{v}^2 + \dot{w}^2\right)\mathrm{d}V = \frac{mA}{2}\int_{-S/2}^{S/2}\left(\dot{v}^2 + \dot{w}^2\right)\mathrm{d}s, \tag{13}$$

and U is the total potential energy of the system given by

$$\begin{aligned} U &= \frac{1}{2}\int_{-S/2}^{S/2}\int_A E\varepsilon^2 \mathrm{d}A\mathrm{d}s - \int_{-S/2}^{S/2}\delta(s)Qv\mathrm{d}s \\ &= \int_{-S/2}^{S/2}\left[\frac{1}{2}\left(AE\varepsilon_m^2 + EI_x v''^2\right) - \delta(s)Qv\right]\mathrm{d}s, \end{aligned} \tag{14}$$

where $\bar{\delta}(s)$ is the Dirac-delta function, E is the Young's modulus of steel, A is the area of the cross-section, and I_x is the second moment of area of the cross-section about its major principal axis.

In Eq. 14, the longitudinal normal strain ε at an arbitrary point of the cross-section consists of the membrane strain ε_m and bending strain ε_b as [1, 2]

$$\varepsilon = \varepsilon_m + \varepsilon_b \quad \text{with} \quad \varepsilon_m = w' - v/R + v'^2/2 \quad \text{and} \quad \varepsilon_b = -yv'', \tag{15}$$

where $(\,)' = \partial(\,)/\partial s$, s is the axial coordinate (Figure 1), v and w are the radial and axial displacements of the centroid, R is the initial radius of the circular arch, and y is the coordinate of the arbitrary point in the principal axis system of the cross-section.

The equations of motion can be derived from Hamilton's principle which can be stated as

$$\int_{t_1}^{t_2} \delta \mathcal{L} \mathrm{d}t = \int_{t_1}^{t_2} \delta\left(T - U\right)\mathrm{d}t = 0 \text{ with } \delta v = \delta w = 0 \text{ at } t = t_1, t_2 \text{ for } -S/2 \le s \le S/2. \tag{16}$$

Integrating Eq. 16 by parts and considering that δv and δw are arbitrary, leads to the differential equations of motion as

$$\varepsilon_m' + mA\ddot{w} = 0 \quad \text{and} \quad EI_x v^{iv} - AE\varepsilon_m v'' - AE\varepsilon_m / R + mA\ddot{v} = \bar{\delta}(s)Q/R\,, \tag{17}$$

in the axial and radial directions; and to the boundary conditions $v = v'' = w = 0$ at $s = \pm S/2$.

In this study, the arch is assumed to be free from loading and at rest at $t = 0$ before the step loading. Hence, the initial conditions of the arch are $v = \dot{v} = \ddot{v} = w = \dot{w} = \ddot{w} = 0$ at $t = 0$ for $-S/2 \le s \le S/2$.

4. ELASTO-STATIC INSTABILITY OF SHALLOW STEEL ARCHES

4.1 Nonlinear Elasto-Static Equilibrium

In order to use the principle of energy conservation to investigate the dynamic instability of a shallow arch under central step loading of infinite duration, knowledge of the static primary equilibrium path and of the static instability of the arch under a central static load is essential. The static instability of a shallow pin-ended circular arch was investigated by Bradford et al. [1]. For the static instability analysis, the displacements v and w are independent of time t and so $\dot{v} = \ddot{v} = \dot{w} = \ddot{w} = 0$.

From the first equation of Eq. 17, the membrane strain is a constant and can be written as

$$\varepsilon_m = -\frac{N}{AE} \tag{18}$$

where N is the axial compressive force.

The differential equation of equilibrium for the radial direction can then be obtained from the second differential equation of motion of Eq. 17 as

$$\frac{v^{iv}}{\mu^2} + v'' = \frac{\bar{\delta}(s)Q}{NR} - \frac{1}{R}, \tag{19}$$

where μ is the axial force parameter and is defined by

$$\mu^2 = \frac{N}{EI_x}. \tag{20}$$

The solution for v can be obtained from Eq. 19 and the boundary conditions $v = v'' = 0$ at $s = \pm S/2$ as

$$v = \frac{1}{\mu^2 R}\left\{1 - \frac{\cos(\mu s)}{\cos(\mu S/2)} + \frac{1}{2}\left[(\mu S/2)^2 - (\mu s)^2\right] + \frac{\bar{Q}}{\mu S/2}\left[\tan(\mu S/2)\cos(\mu s) - \mu S/2 + H(s)(\mu s - \sin(\mu s))\right]\right\}, \tag{21}$$

where the dimensionless load $\bar{Q}$ is given by

$$\bar{Q} = \frac{Q(S/2)^2}{2\Theta EI_x} = \frac{QRS}{4EI_x}, \tag{22}$$

and the step function $H(\theta)$ is given by

$$H(s) = \begin{cases} 1 & \text{for } s > 0 \\ -1 & \text{for } s < 0 \end{cases}. \tag{23}$$

From Eqs. 15 and 18, it can be obtained that

$$w' = -\frac{N}{AE} + \frac{v}{R} - \frac{v'^2}{2}. \tag{24}$$

Substituting Eq. 21 into Eq. 24 and integrating it over the entire arch leads to the nonlinear equation of equilibrium for the external central load and the internal axial force as

$$A_1\bar{Q}^2 + B_1\bar{Q} + C_1 = 0, \tag{25}$$

where

$$A_1 = \frac{1}{4(\mu S/2)^4}\left[\tan^2(\mu S/2) - \frac{3\tan(\mu S/2)}{\mu S/2} + 3\right], \tag{26}$$

$$B_1 = \frac{1}{2(\mu S/2)^4}\left[\frac{2\cos(\mu S/2) - \mu S/2\sin(\mu S/2)}{\cos^2(\mu S/2)} - 2\right], \tag{27}$$

$$C_1 = \left(\frac{\mu S}{2\lambda}\right)^2 + \frac{\mu S/2 - \sin(\mu S/2)\cos(\mu S/2)}{4(\mu S/2)^3\cos^2(\mu S/2)} - \frac{1}{6} \quad \text{with} \quad \lambda = \frac{\Theta}{2}\frac{S/2}{r_x} = \frac{S^2}{4r_x R}, \tag{28}$$

in which λ is the geometric parameter of the arch, which is a function of the half included angle Θ and the slenderness S/r_x of the arch.

4.2 Limit Instability

A typical nonlinear elastic behaviour obtained from Eqs. 21 and 25 for an arch with a geometric parameter λ = 6.5 is shown in Figure 7a as variations of the dimensionless central displacement

v_c/f with the dimensionless load $\bar{Q}$, and in Figure 7b as variations of the internal axial force parameter $\mu S/2$ with the dimensionless load $\bar{Q}$, where v_c is the central radial displacement and f is the arch rise. It is assumed that the arch is loaded in a displacement-controlled manner. It can be seen from Figures 7a and 7b that as the displacement increases, the load and the internal force parameter increase along the stable equilibrium path 0*a* until the upper limit point *a* is reached. As the displacement continues to increase, the load decreases along the unstable equilibrium path *ab* and the internal axial force parameter increases first and then decreases until the lower limit point *b* is reached. As the displacement increases further, the load increases again but the internal axial force continues to decrease along the stable equilibrium path *bf*. The loads corresponding to the upper and lower limit points are known as the upper and lower limit instability loads, respectively.

However, in practice, an arch is usually loaded in a load-controlled manner. When the load is increased further from the limit point *a* by an infinitesimal amount, there is no adjacent stable equilibrium state and the only possible stable equilibrium state exists at a finite distance apart, i.e. at the state corresponding to the stable equilibrium point *c* as shown in Figures 7a and 7b. Therefore, the arch snaps through from the limit point *a* to the equilibrium point *c*, as indicated by the dashed lines in Figures 7a and 7b, which are not an equilibrium path.

When the external load decreases, the arch follows the path *fcb* until the lower limit point *b* is reached. If the load is further decreased by an infinitesimal amount, there is no adjacent stable equilibrium state and the arch will snap-through to the stable equilibrium point *d*. Because of the snap-through phenomenon, the upper and lower limit instability loads are also known as the upper and lower snap-through buckling loads.

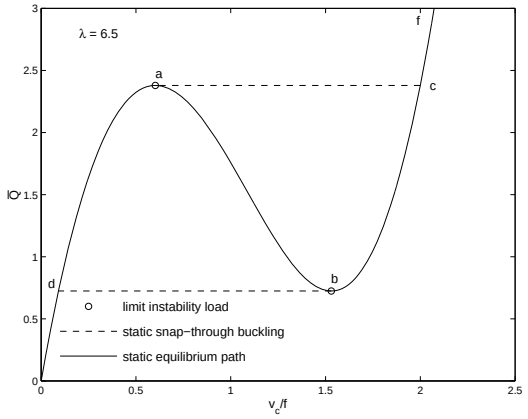

a. Variations of Dimensionless Central Displacement with Dimensionless Load

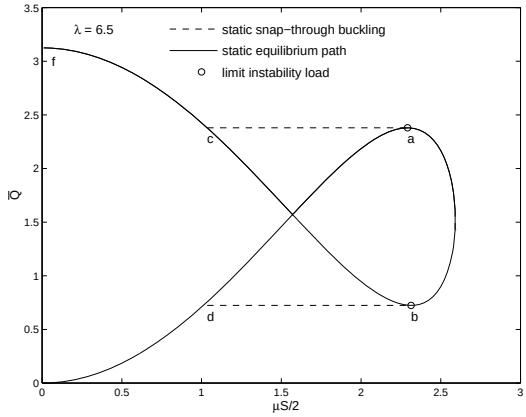

b. Variations of Dimensionless Axial Force with Dimensionless Load

Figure 7. Static Limit Instability

Eq. 25 expresses the load $\bar{Q}$ as an implicit function of the axial force parameter μ as $F(\bar{Q},\mu)=0$. Setting $\partial\bar{Q}/\partial\mu=-\left(\partial F\left(\bar{Q},\mu\right)/\partial\mu\right)/\left(\partial F\left(\bar{Q},\mu\right)/\partial\bar{Q}\right)$ leads to the following equation for the upper and lower limit points *a* and *b*

$$A_2\bar{Q}^2+B_2\bar{Q}+C_2=0, \tag{29}$$

$$A_2=\frac{1}{8\left(\mu S/2\right)^4}\left[8-\frac{15\tan\left(\mu S/2\right)}{8\left(\mu S/2\right)}+\frac{7}{\cos^2\left(\mu S/2\right)}-\frac{2\left(\mu S/2\right)\tan\left(\mu S/2\right)}{\cos^2\left(\mu S/2\right)}\right], \tag{30}$$

$$B_2 = \frac{1}{4(\mu S/2)^4}\left[\frac{8}{\cos(\mu S/2)} - 8 - \frac{5(\mu S/2)\tan(\mu S/2)}{\cos(\mu S/2)} - \frac{(\mu S/2)^2}{\cos(\mu S/2)} + \frac{2(\mu S/2)^2}{\cos(\mu S/2)}\right], \tag{31}$$

$$C_2 = \frac{1}{8(\mu S/2)^2}\left[\frac{3}{\cos^2(\mu S/2)} - \frac{3\tan(\mu S/2)}{\mu S/2} - \frac{2(\mu S/2)\tan(\mu S/2)}{\cos^2(\mu S/2)}\right] - \frac{(\mu S/2)^2}{\lambda^2}. \tag{32}$$

The limit instability loads obtained by solving Eqs. (25) and (29) simultaneously are shown in Figures 7a and 7b.

4.3 Bifurcation Buckling

Considering equilibrium in the prebuckled and the adjacent buckled configurations, and that the buckling membrane strain $\varepsilon_{mb} = 0$, leads to the differential equation for elasto-bifurcation buckling of the arch as

$$\frac{v_b^{iv}}{\mu^2} + v_b'' = 0, \tag{33}$$

where v_b is the buckling displacement. The solution of Eq. 33 can be written as

$$v_b = E_1\cos(\mu s) + E_2\sin(\mu s) + E_3 s + E_4. \tag{34}$$

Substituting Eq. 34 into the boundary conditions $v_b = v_b'' = 0$ at $s = \pm S/2$ leads to a group of four homogeneous algebraic equations for E_1, E_2, E_3, E_4. The condition for nontrivial solutions of the group of equations for E_1, E_2, E_3, and E_4 leads to a characteristic equation as

$$\sin(\mu S/2)\cos(\mu S/2) = 0. \tag{35}$$

The fundamental solution of the first factor $\sin(\mu S/2) = 0$ of Eq. 35 is $\mu S/2 = \pi$ and substituting this into the nonlinear equation of equilibrium given by Eq. 25 yields the equation for the bifurcation buckling load as

$$A_3\bar{Q}^2 + B_3\bar{Q} + C_3 = 0 \quad \text{with} \quad A_3 = \frac{3}{4\pi^4},\ B_3 = -\frac{2}{\pi^4},\ C_3 = \frac{1}{4\pi^2} - \frac{1}{6} + \frac{\pi^2}{\lambda^2}. \tag{36}$$

Typical bifurcation buckling behaviour for an arch with a geometric parameter λ = 13 obtained from Eqs. 22, 25 and 36 is shown in Figure 8a as variations of the dimensionless central displacement v_c/f with the dimensionless load $\bar{Q}$ and in Figure 8b as variations of the internal axial force parameter $\mu S/2$ with the dimensionless load $\bar{Q}$. It can be seen from Figures 8a and 8b that as the displacement increases, the load increases along the stable equilibrium path 0*a* until the upper bifurcation point *a* is reached. As the displacement continues to increase, the internal axial force remains a constant but the load decreases along the secondary bifurcation unstable equilibrium path *ab* until the lower bifurcation point *b* is reached and at the lower bifurcation point *b*, equilibrium of the arch bifurcates from the secondary bifurcation equilibrium path back to the primary stable equilibrium path *bf*. After that, as the displacement increases, the load again

increases but the internal axial force continues to decrease along the stable equilibrium path *bf*. The curve for the primary equilibrium path is also shown in Figures 8a and 8b. It can be seen that the upper limit instability load at the limit point a_s is higher than the upper bifurcation buckling load, while the lower limit instability load at the limit point b_s is lower than the lower bifurcation buckling load. Hence, limit instability of this arch cannot occur.

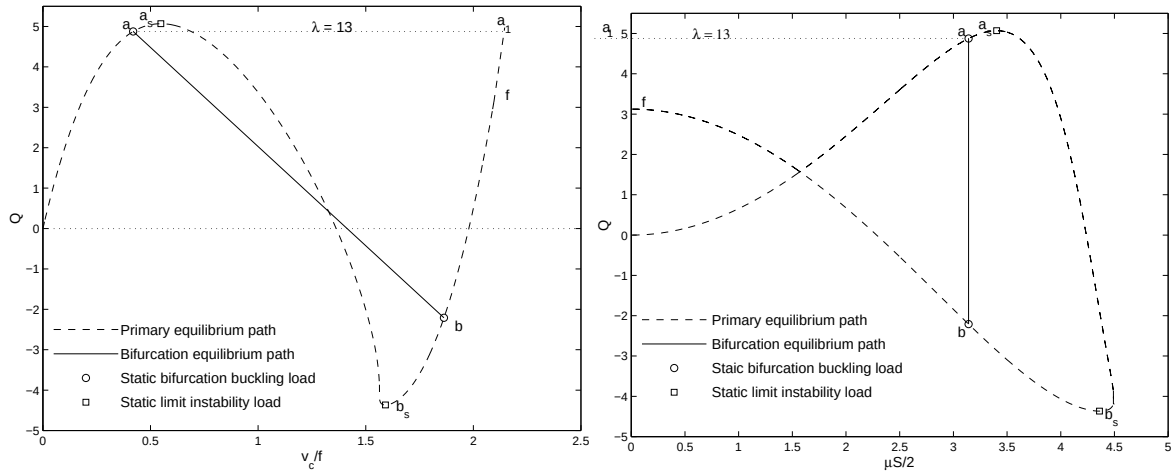

a. Variations of Dimensionless Central Displacement with Dimensionless Load

b. Variations of Dimensionless Axial Force with Dimensionless Load

Figure 8. Bifurcation Buckling

In practice, an arch is usually loaded in a load-controlled manner. When the load is increased further from the bifurcation buckling point *a* by an infinitesimal amount, there is no adjacent stable equilibrium state and the only possible equilibrium state exists at a finite distance apart, i.e. at the state corresponding to a remote stable equilibrium point a_1 as shown in Figures 8a and 8b. Similarly to the limit instability, the arch snaps from the bifurcation buckling point *a* to the remote stable equilibrium point a_1, as indicated by the dashed lines in Figures 8a and 8b, which is not an equilibrium path.

5 ELASTO-DYNAMIC ISTABILITY OF SHALLOW STEEL ARCHES

The criterion for the elasto-dynamic instability developed for the one degree-of-freedom idealized arch system can be applied to the elasto-dynamic instability analysis of shallow pin-ended arches under central step loading with infinite duration.

The dimensionless total potential energy of the arch and load system can be obtained by substituting solutions for the membrane strain ε_m given by Eq. 18 and for the radial displacement v given by Eq. 21 into the expression for the dimensionless total potential energy given by Eq. 14 and then integrating the expression as

$$U = \frac{EI_x}{R^2}\left(A_4\bar{Q}^2 + B_4\bar{Q} + C_4\right), \tag{37}$$

where

$$A_4 = \frac{\left[(\mu S/2) + 4(\mu S/2)\cos^2(\mu S/2) - 5\sin(\mu S/2)\cos(\mu S/2)\right]}{2\mu^3 (S/2)^2 \cos^2(\mu S/2)}, \tag{38}$$

$$B_4 = \frac{\left\{4\cos(\mu S/2) - \left[4 + (\mu S/2)^2\right]\cos^2(\mu S/2) - \mu S/2 \sin(\mu S/2)\right\}}{\mu^2 S/2 \cos^2(\mu S/2)}, \tag{39}$$

$$C_4 = \frac{S}{2} + \frac{S}{4\cos^2(\mu S/2)} - \frac{3\tan(\mu S/2)}{2\mu} + \frac{\mu^2 S^3}{8}\left(\frac{\mu S/2}{\lambda}\right)^2. \tag{40}$$

Before being subjected to the central step loading, the shallow arch is assumed to be free from loading and at rest. Hence, the total energy of the arch is equal to zero, i.e. $E = 0$ at $t = 0$. From the principle of energy conservation, for $t > 0$

$$E = T + U = 0. \tag{41}$$

It is noted that the kinetic energy T of the arch imparted by the step loading is a positive definite function of the velocities. When the load is sufficiently small, from Eq. 14, the potential energy U of the arch and load system at a stable equilibrium position is non-positive, the principle of energy conservation given by Eq. 41 may hold and the arch will oscillate about the stable equilibrium position. However, when the load is so small that the total potential energy U of the system at an unstable equilibrium position given by Eq. 14 is positive, the total energy E does not vanish and the principle of energy conservation given by Eq. 41 is violated. In this case, the motion of the arch to the unstable equilibrium position is impossible. As the value of the step load increases, it can be obtained from Eq. 14 that the total potential energy U decreases. Because the kinetic energy of the arch is a positive definite function, its minimum value is equal to zero. From the principle of energy conservation given by Eq. 41, the necessary condition that the arch can move to the unstable equilibrium position with the zero kinetic energy is vanishing of the total potential energy U of the arch, i.e.

$$U = A_4 \bar{Q}^2 + B_4 \bar{Q} + C_4 = 0. \tag{42}$$

In this case, the elasto-dynamic instability of the arch under the central step loading of infinite duration is possible. Because the elasto-dynamic instability load corresponds to an unstable equilibrium position, it also needs to satisfy the equilibrium equation given by Eq. 25. The elasto-dynamic instability load can then be obtained by solving Eqs. 25 and 42 simultaneously. Since Eq. 25 describes the primary equilibrium of the arch, the solution obtained is the upper elasto-dynamic instability load.

The total potential energy may also vanish on the secondary bifurcation unstable equilibrium path. In this case, the lower elasto-dynamic instability load can be obtained by solving Eq. 42 with $\mu S/2 = \pi$.

Typical solutions for the upper and lower elasto-dynamic instability loads for an arch with an arch geometric parameter $\lambda = 14$ are shown in Figure 9, where the solid line is the primary equilibrium path under static loading, the dashed line is the secondary equilibrium path for bifurcation buckling, and the dot-dashed line represents the variation of the dimensionless load $\bar{Q}$ and axial force parameter $\mu S/2$ for the condition of zero total potential energy ($U = 0$). The intersection point d_u of the zero total potential energy curve and the unstable branch $a_s b_s$ of the primary equilibrium path

defines the upper elasto-dynamic instability load while the intersection point d_l on the zero total potential energy curve and the secondary bifurcation equilibrium path *ab* defines the lower elasto-dynamic instability load.

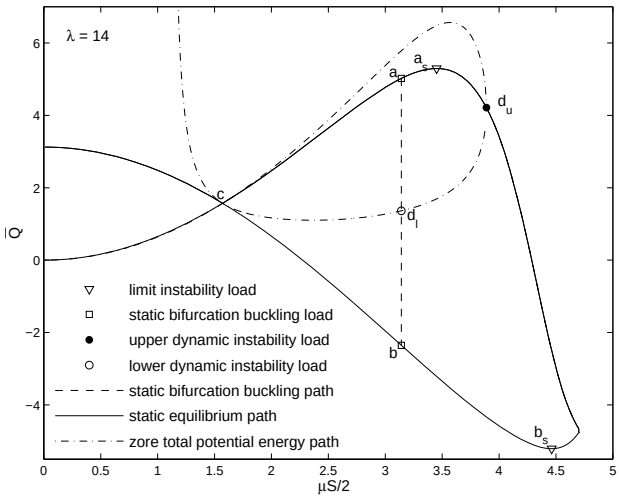

Figure 9. Upper and Lower Dynamic Instability Loads

The variations of the dimensionless upper and lower elasto-dynamic instability loads $QS^2/16EI_x$ with the arch geometric parameter λ are shown in Figure 10. It can be seen that the elasto-dynamic instability load increases with an increase of the arch geometric parameter. The variations of the elasto-static instability loads $QS^2/16EI_x$ of the arches given by Eqs. 25, 29, and 36 with the geometric parameter λ are also shown in Figure 10. It can be seen that both the upper and the lower elasto-dynamic instability loads are lower than the corresponding elasto-static instability load.

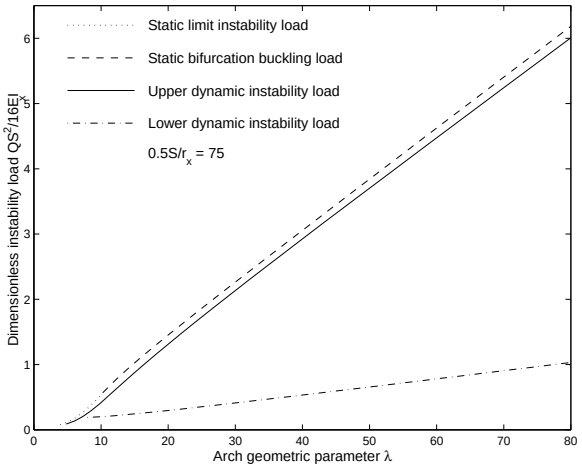

Figure 10. Comparisons of Dynamic Instability Loads with their Static Counterparts

6. CONCLUSIONS

The principle of conservation of energy was used in this paper in conjunction with a one degree-of-freedom idealized arch system to establish an energy criterion for the elasto-dynamic instability of a conservative structural system. The merit of the criterion is that it can determine the critical instability load without the need to solve the equations of motion of the system. The energy criterion was applied to the elasto-dynamic instability analysis of shallow pin-ended circular steel

arches that are subjected to central step loading with infinite duration. The exact total potential energy, and the exact primary equilibrium and the secondary bifurcation equilibrium paths have been obtained, which are essential for the elasto-dynamic instability analysis based on the principle of energy conservation. Analytical solutions for the upper and lower elasto-dynamic instability loads of shallow pin-ended arches under the central step loading with infinite duration have been obtained. Because they are based on the exact total potential energy and equilibrium paths, the solutions for the elasto-dynamic instability loads are accurate. It has been found that the elasto-dynamic instability load for a pin-ended arch increases with an increase of the arch geometric parameter. It has also been found that the elasto-dynamic instability load of a shallow pin-ended arch due to the central step loading is lower than its elasto-static counterpart.

ACKNOWLEDGEMENTS

This work has been supported by the Australian Research Council through Discovery Projects, and an Australian Research Council Federation Fellowship, awarded to the second author.

REFERENCES

[1] Bradford, M.A., Uy, B. and Pi, Y.-L., "In-Plane Elastic Stability of Arches under a Central Concentrated Load", Journal of Engineering Mechanics, ASCE, 2002, Vol. 128, No. 7, pp. 710-719.

[2] Pi, Y.-L., Bradford, M.A. and Uy, B., "In-Plane Stability of Arches", International Journal of Solids and Structures, 2002, Vol. 39, No. 1, pp. 105-125.

[3] Pi, Y.-L., Bradford, M.A. and Tin-Loi, F., "Nonlinear In-Plane Buckling of Rotationally Restrained Shallow Arch under a Central Concentrated Load", International Journal of Non-Linear Mechanics, 2008, Vol. 43, No. 1, pp. 1-17.

[4] Pi, Y.-L., Bradford, M.A. and Tin-Loi, F., "Nonlinear Analysis and Buckling of Elastically Supported Circular Shallow Arches", International Journal of Solids and Structures, 2007, Vol. 44, No. 7-8, pp. 2401-2425.

[5] Pi, Y.-L. and Trahair, N.S., "Non-Linear Buckling and Postbuckling of Elastic Arches", Engineering Structures, 1998, Vol. 20, No. 7, pp. 571-579.

[6] Budiansky, B. and Roth, R.S., "Axisymmetric Dynamic Buckling of Clamped Shallow Spherical Shells", Collected Papers on Instability of Shell Structures, NASA TN D-1510, 1962.

[7] Budiansky, B. and Hutchinson, J.W., "Dynamic Buckling of Imperfection-Sensitive Structures", Proceedings XI International Congress of Applied Mechanics, Munich, 1964.

[8] Hsu, C.S., "Stability of Shallow Arches against Snap-Through under Timewise Step Loads", Journal of Applied Mechanics, 1968, Vol. 35, No. 1, pp. 1-39.

[9] Simitses, G.J., "Dynamic Stability of Suddenly Loaded Structures", Springer-Verlag, New York, USA, 1990.

[10] Lo, D.L.C. and Masur, E.F., "Dynamic Buckling of Shallow Arches", Journal of the Engineering Mechanics Division ASCE, 1976, Vol. 102, No. EM3, pp. 901-917.

[11] Gregory, W.E. Jr. and Plaut, R.H., "Dynamic Stability Boundaries for Shallow Arches", Journal of the Engineering Mechanics Division ASCE, 1982, Vol. 108, No. EM6, pp. 1036-1050.

[12] Donaldson, M.T. and Plaut, R.H., "Dynamic Stability Boundaries of a Sinusoidal Shallow Arch under Pulse Loads", AIAA Journal, 1983, Vol. 21, No. 3, pp. 469-471.

[13] Matsunaga, H., "In-Plane Vibration and Stability of Shallow Circular Arches Subjected to Axial Forces", International Journal of Solids and Structures, 1996, Vol. 33, No. 4, pp. 469-482.

[14] Huang, C.S., Nieh, K.Y. and Yang, M.C., "In-Plane Free Vibration and Stability of Loaded and Shear Deformable Circular Arches", International Journal of Solids and Structures, 2003, Vol. 40, No. 22, pp. 5865-5886.

[15] Kounadis, A.N., Gantes, C.J. and Bolotin, V.V., "Dynamic Buckling Loads of Autonomous Potential System Based on the Geometry of the Energy Surface", International Journal of Engineering Science, 1999; Vol. 37, pp. 1611-1628.

[16] Kounadis, A.N., Gantes, C.J. and Raftoyiannis, I.G., "A Geometric Approach for Establishing Dynamic Buckling Load of Autonomous Potential N-Degree-of-Freedom Systems", International Journal of Non-Linear Mechanics, 2004; Vol. 39, pp. 1635-1646.

[17] Pi, Y.-L. and Bradford, M.A., "Dynamic buckling of shallow pin-ended arches under a sudden central concentrated load", Journal of Sound and Vibration, 2008, Vol. 17, No. 3-5, pp. 898-917.

EXPERIMENTAL STUDIES ON STRESS CONCENTRATION FACTORS FOR PARTIALLY OVERLAPPED CIRCULAR HOLLOW SECTION K-JOINTS

C.K. Lee *, S.P. Chiew, S.T. Lie, T. Sopha and T.B.N. Nguyen

School of Civil and Environmental Engineering, Nanyang Technological University
50, Nanyang Avenue, Singapore 639798
**(Corresponding author: E-mail: ccklee@ntu.edu.sg)*

Received: 14 May 2008; Revised: 9 July 2008; Accepted: 29 July 2008

ABSTRACT: This paper describes the testing results of two full-scale partially overlapped circular hollow section (CHS) K-joints. The two specimens were designed in such a way that partially overlapping is inevitable in order to eliminate the eccentricity of the resulted joints. Experimental studies were carried out by applying static loadings at the end of the through braces of the joints. The stress distributions of the partially overlapped CHS K-joints tested under the three basic loading cases (axial (AX), in-plane (IPB) and out-of-plane bending (OPB)) and their combinations were carefully recorded during the test. For each specimen, experimental study was carried out to investigate the stress concentration factor (SCF) and the hot spot stress (HSS) distributions along the brace-chord intersections. The experimental results obtained show that even for a simple combination of AX and IPB loading cases, the maximum HSS could be located either on the brace side or the chord side of the joints. The SCFs obtained from the experimental studies are compared with the SCF formulae suggested by Efthymiou and Durkin [1] and those from finite element analyses. It is observed that Efthymiou's formulae may not be completely suitable for the design of partially overlapped CHS K-joints.

Keywords: Partially overlapped circular hollow section K-joint, stress concentration factor, hot spot stress, fatigue assessments

1. INTRODUCTION

Simple non-overlapped circular hollow section (CHS) K-joint is one of the most widely used connection types in offshore structures. However, due to the existence of a gap between the braces, under some geometrical configurations, eccentricity and unbalanced moment could be generated on the chord and this may lead to undesirable brittle responses of the joints (BOMEL [2]). Hence, in many design codes (Zhao et al. [3] and EC3 [4]), an upper limited is imposed on the eccentricity for non-overlapped K-joints. In practice, any eccentricity for a non-overlapped CHS K-joint could be eliminated by partially overlapping the braces. When compared with a non-overlapped K-joint, a partially overlapped CHS K-joint normally has a higher fabrication cost due to the more complex intersection profile. However, due to their optimized load transfer pattern and zero eccentricity property, partially overlapped CHS K-joints often offer a higher residual capacity and ultimate strength (Bouwkamp [5-6]). In a study carried out by Healy [7], it was found that in case the through brace was in tension, the capacity of partially overlapped joint was much better than when it was otherwise loaded. Dexter and Lee [8-9] examined numerically the effects of several geometrical parameters and the overlapping percentage on the behaviour of overlapped joints. It was founding that, in general, overlapping the braces has a beneficial effect on joint strength for the joints with relatively thick brace walls. Furthermore, it was also reported from Dexter et al. [10] that partially overlapped CHS K-joints are expected to have increased strength up to a certain amount of overlap and then decrease when the joint is completely overlapped. Besides strength enhancement, partially overlapped joint could also lead to more cost effective joint design. In a study carried out by Tizani et. al. [11], it is found that after considering both material and fabrication costs, the use of a partially overlapped joint could lead to the cheapest solution with the addition fabrication cost actually offset by avoiding the use of canned gap joint as an alternative.

In the study of fatigue performance of partially overlapped CHS K-joints, works by Bouwkamp [5-6] found that the stress concentration factor (SCF) could be reduced by more than 30% when compared with the non-overlapped CHS K-joints having the same parameters and properties. Fessler et al. [12] also observed that the hot spot stress (HSS) of a partially overlapped CHS K-joint is 40%-45% less than a gap joint. Furthermore, having compared the results of overlapped and gapped CHS K-joints, Gibstein [13] concluded that fatigue strength improvements could be obtained by using a partially overlapped joint with same chord and brace diameter. So far, the most detailed work related to the SCF and the HSS distributions of this joint type was published by Efthymiou and Durkin [1]. Over 100 partially overlapped CHS K-joints were analyzed using finite element (FE) models for nine different load cases. Parametric equations were then developed for each load case and the results were experimentally verified by Dharmavasan and Seneviratne [14] using acrylic models. It was found that overlapping helps reduce the chord SCFs significantly.

Despite the above mentioned advantages of a partially overlapped K-joint, equations for the fatigue design of this type of joints are not commonly available in design code. Efthymiou and Durkin [1] had published some formulae but they were not adopted in the EC3 [4]. Furthermore, not many full scale testing results related to the SCF and the HSS values for partially overlapped CHS K-joints were reported (Lee et al. [15]). The main objective of this study is to investigate experimentally the SCF distribution around the brace-chord intersection for this type of joints. Static tests were conducted for two carefully designed full scale partially overlapped CHS K-joints. Basic (AX, IPB and OPB) and combined loadings were applied to the joints and detailed measurements for the stresses induced along the joint intersection were made. A comparison between the experimental results obtained with Efthmiou's formulae [1] and those obtained from FE modeling are then carried out.

2. SET UP OF THE TEST RIG AND THE LOADING SYSTEM

The tests of the partially overlapped CHS K-joints were carried out using the "orange" rig (Figure 1) located in the Construction Technology Laboratory, School of Civil and Environmental Engineering, Nanyang Technological University. This test rig is designed for static and fatigue tests of hollow section joints under AX, IPB and OPB loads or combinations of them. The test rig has three actuators namely, Actuators 1, 2 and 3 (Figure 2) installed at one end of the rig which are able to apply cyclic loadings with adjustable frequency to the specimen along three mutually perpendicular axes. In this study, Actuators 1 and 2 which have a maximum capacity of 250kN were employed to apply AX and IPB loadings, respectively. Actuator 3 with a maximum capacity of 150kN was employed for the generation OPB loading. All three actuators can apply both tension and compression loadings and they can be operated individually or concurrently to create combined loading conditions.

3. THE SPECIMENS TESTED

In this study, two full scale partially overlapped CHS K-joints (Specimen I and Specimen II) were test. The typical test set up of the two specimens and their geometrical properties are shown in Figures 1 and 3. Each joint specimen comprises the chord, a through brace and an overlapping brace. The angles between the braces and the chord are equal to 45° and 60° for Specimens SI and Specimen SII, respectively. These two joints were fabricated using structural steel pipes compiled to the BS EN10210-S355 J2H standard. The joints were welded according to the AWS specifications [16]. Ultrasonic checking was conducted along all the welding paths to ensure that the welding at the intersections of the chord and braces was complete penetration groove weld with

standard flat profile. In the set up of each specimen, both ends of the chord and the overlapping brace were welded onto the flat plates and bolted directly onto strong reaction panels of the rig. The end of the through brace was welded onto a flat plate and bolted directly onto the actuators (Figure 2). The physical dimensions and other important non-dimensional parameters of the specimens are listed in Table 1. The material properties of the sections obtained from standard coupon tests are summarized in Table 2. Note that the section sizes and configurations of these two specimens were carefully selected in such a way that if they are fabricated as non-overlapped joints with minimum gap spacing, the eccentricity of the resulted joints shall exceed the maximum limit imposed by the EC3 [4].

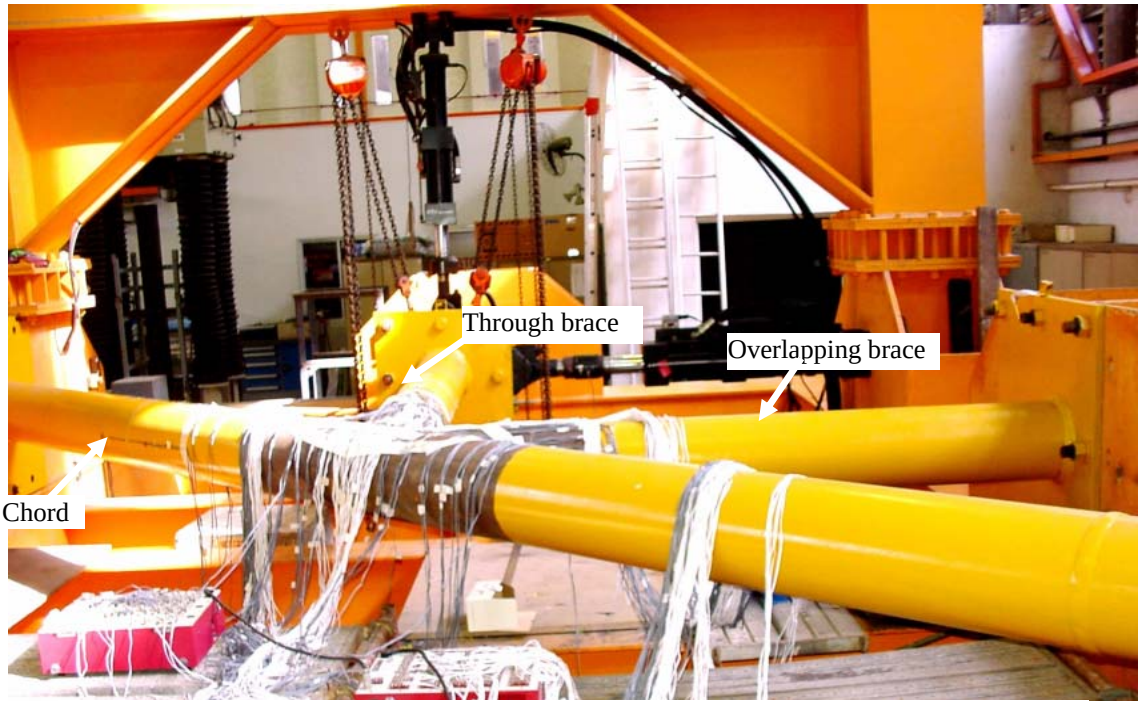

Figure 1. The "Orange" rig and the Partially Overlapped CHS K-Joint Specimen

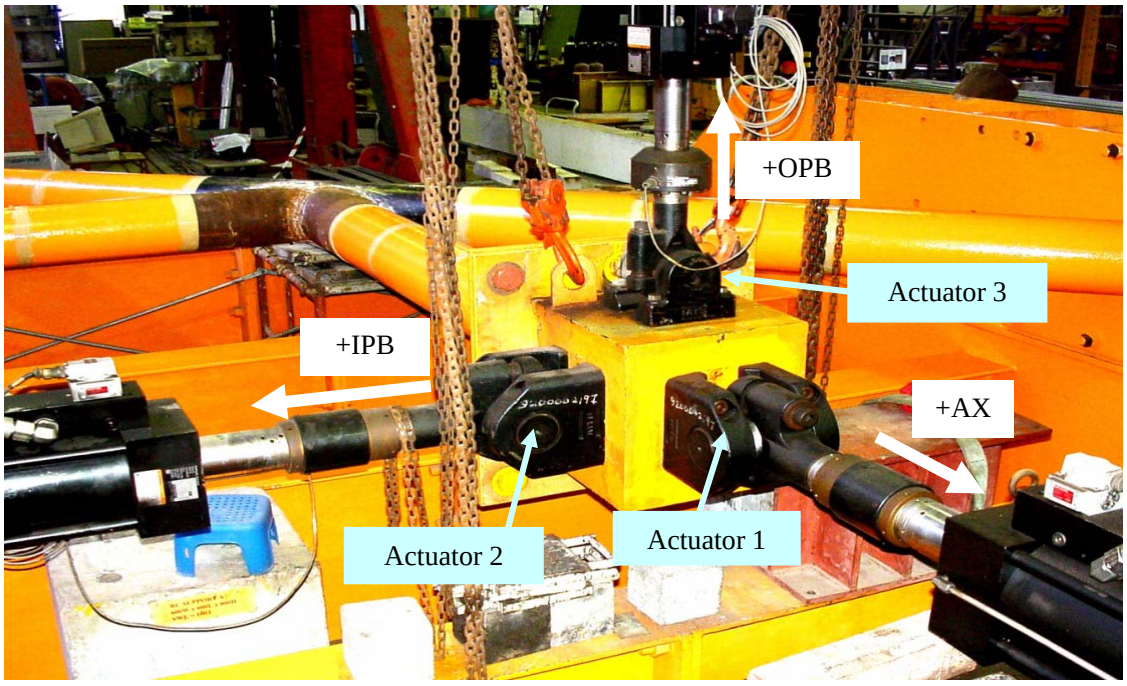

Figure 2. Actuators and Loading Directions

Table 1. Dimension of Specimens

Specimen	D(mm)	T(mm)	d(mm)	t(mm)	θ_1(°)	θ_2(°)	O_V(%)	e(mm)
SI	273	26	244.5	20.0	45	45	21	0
SII	355.6	16	323.9	16	60	60	45.35	0

(a) Physical Dimensions

Specimen	$\alpha=2L_C/D$	$\beta=d/D$	$2\gamma=D/T$	$\tau=t/T$
SI	42.789	0.895	10.50	0.769
SII	27.146	0.91	22.22	1.00

(b) Non-Dimensional Parameters

Table 2. Material Properties of the Specimens

Specimen	**Member**	**Yield strength (MPa)**	**Tensile strength (MPa)**	**Modulus of Elasticity (GPa)**
SI	Chord	403.9	553.6	207.5
	Braces	426.9	585.1	201.9
SII	Chord	428.17	526.00	204.21
	Braces	424.23	564.94	200.89

4. STRAIN AND STRESS MEASUREMENTS

Since the main objective of this study is to investigate the HSS and the SCF distributions along the intersections of the tubular sections, extensive strain measurements were conducted by installation of strain gauge arrays at the joint. At the joint intersections, three curves, namely, Curves A, B and C were identified (Figure 4). Curve A is the intersection between the through and the overlapping brace. Curves B and C are the intersections between the chord and the overlapping and the through braces, respectively. From Figure 4, it can be seen that for each side of the joint, these three curves meet at a junction point. Along these three curves, strain gauges were installed at locations near the weld toe of the chord and the braces to record the strain distributions. As from many past studies (Lee et al. [15, 17]), the quadratic extrapolation method (Zhao et al. [3]) is needed to obtain accurate strain measurements, three rows of strain gauges were installed at each measurement location along the line perpendicular to the weld toe at distances equal to 0.4t, 1.0t and 1.4t (t is the thickness of member) from the weld toe (Figures 4 and 5). Three types of strain gauge arrangements were deployed in this study (Figure 5). At locations far way from the junction point and the saddle and crown of the intersections, a single perpendicular strain gauge arrangement is used. At the saddle and crown of the intersections, an arrangement of a pair of strain gauges arranged in the perpendicular and the parallel directions to the weld toe was adopted. Finally, in order to capture the complex strain pattern, rosettes were deployed at regions close to the junction point. Besides along the intersection curves, eight strain gauges were also installed at the two cross-sections along the through brace to detect any secondary bending moment caused by load eccentricity and joint flexibility (Figure 6). During the test, all strain gauges were connected to four TML ASW-50 switchboxes and a TML TDS-801 data logger. The data logger was then connected to a personal computer where special software for monitoring, collecting and processing of the testing data was installed.

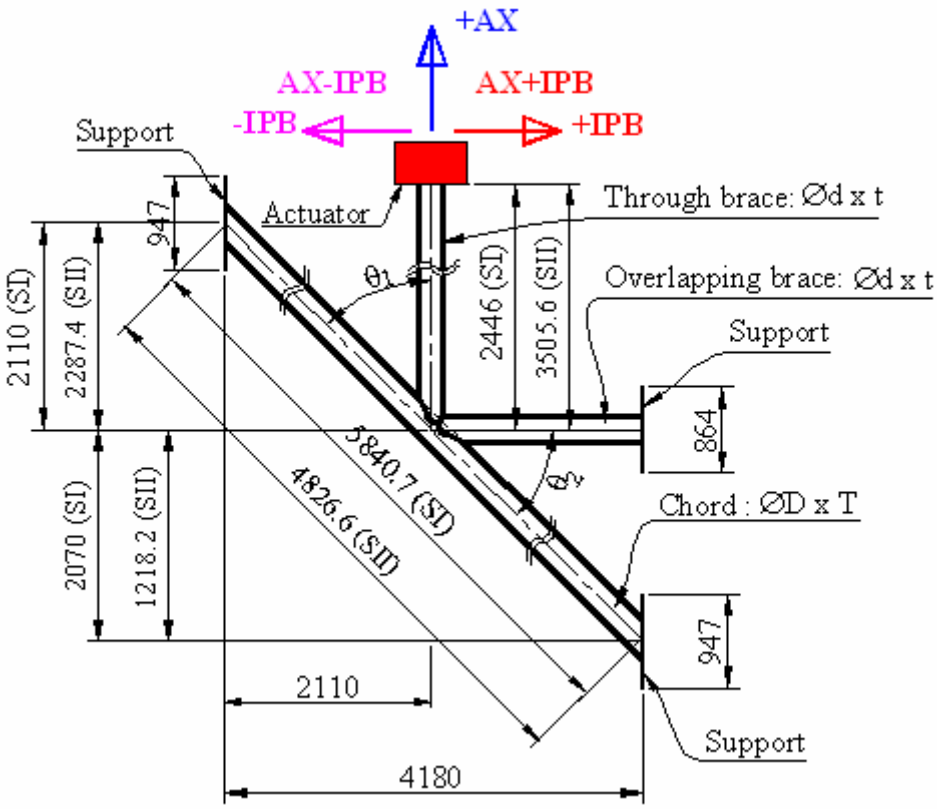

Figure 3. Dimensions and Configuration of the Specimens

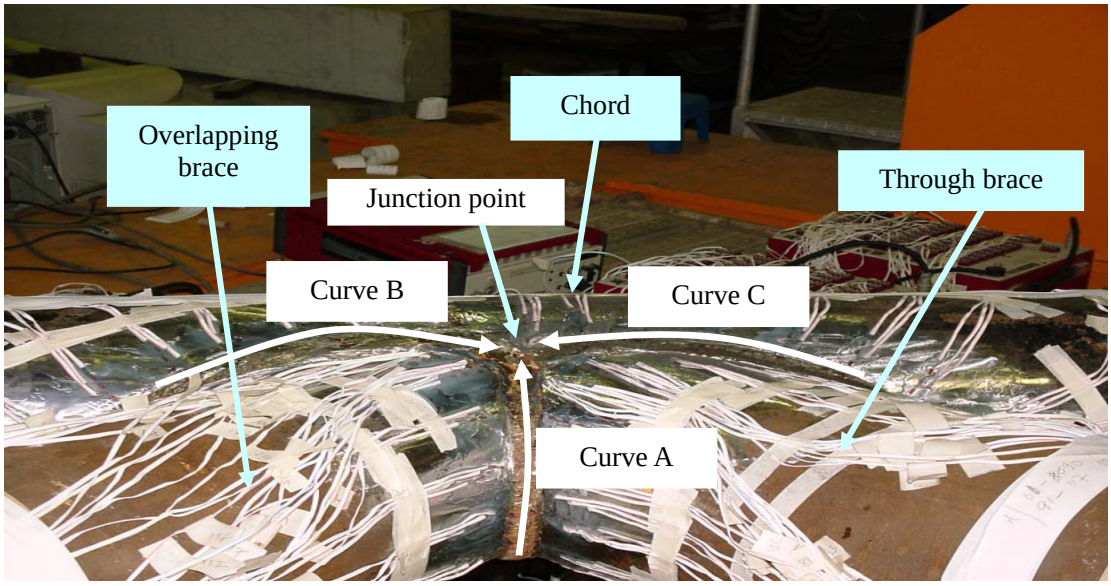

Figure 4. Close up View of the Partially Overlapped Joint and the Three Welding Curves

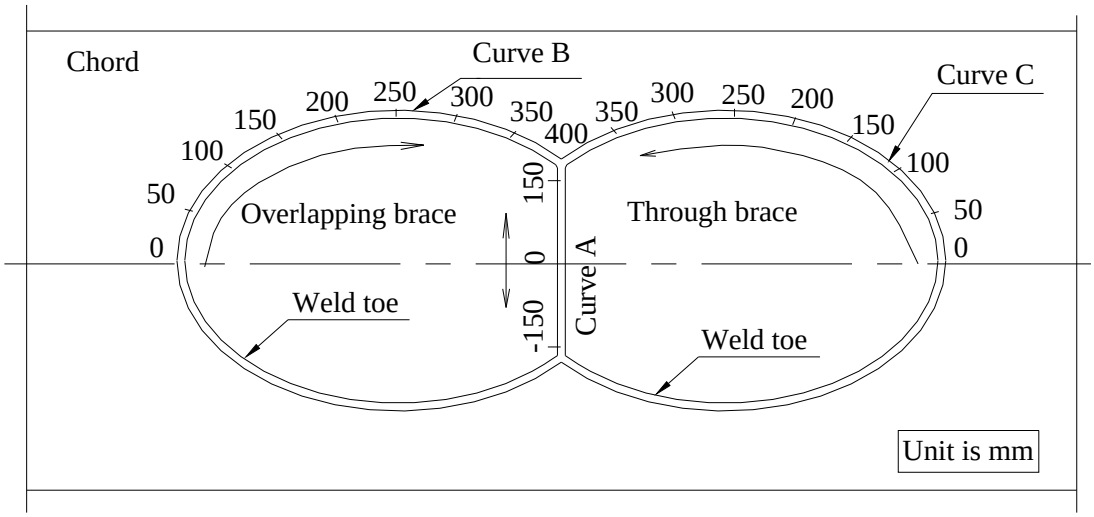

(a) Plan View of the Intersection

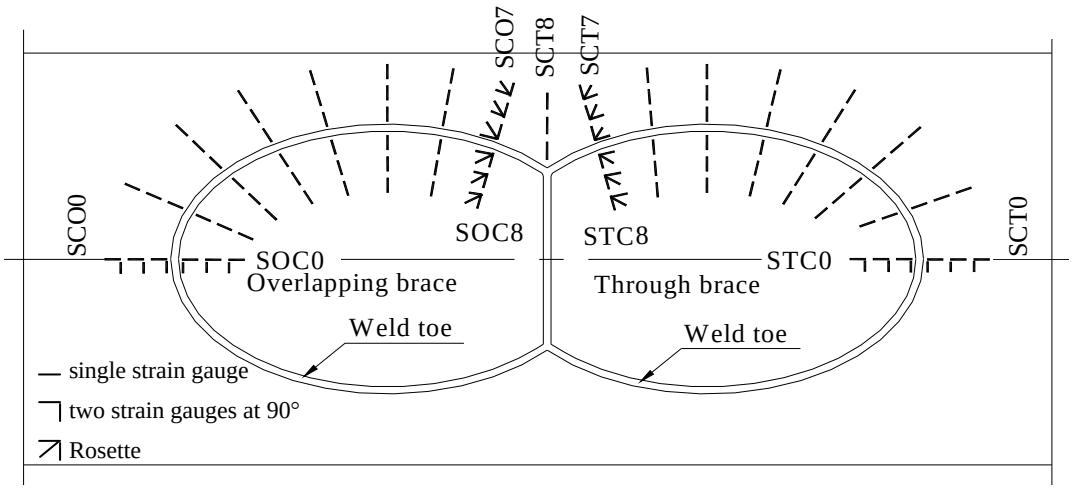

(b) Strain Gauges Locations on Chord and Braces, SI

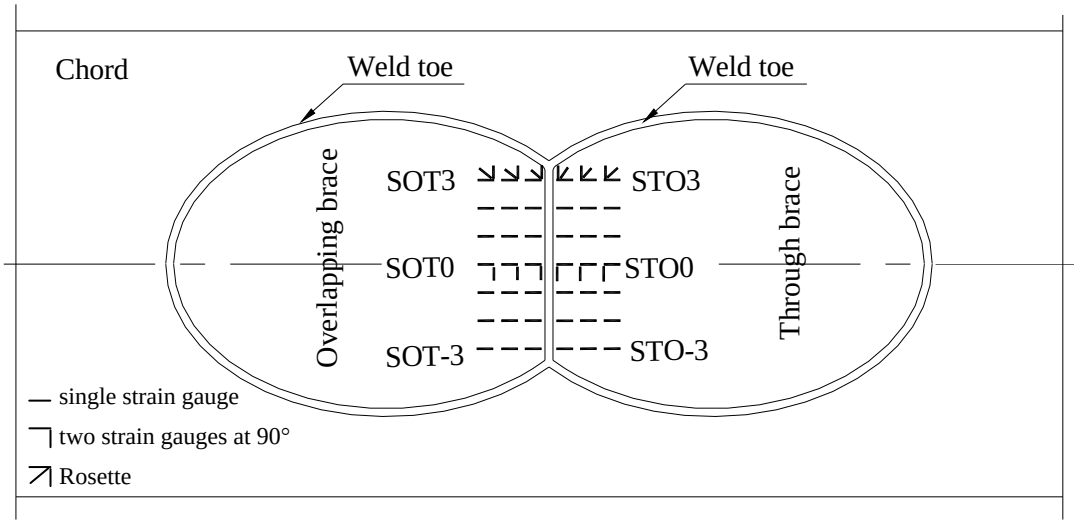

(c) Strain Gauges Locations on Through and Overlapping Braces, SI

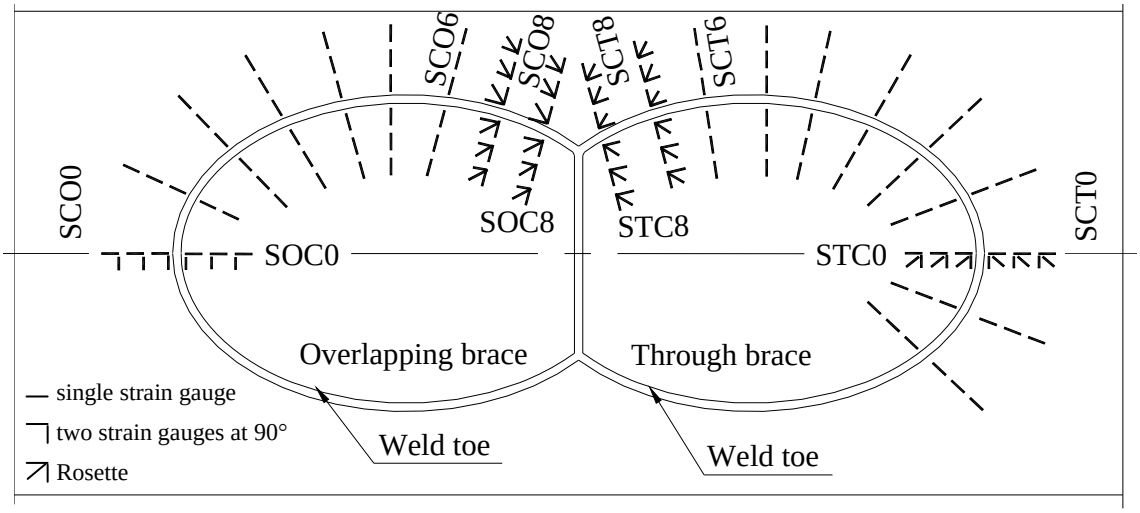

(d) Strain Gauges Locations on Chord and Braces, SII

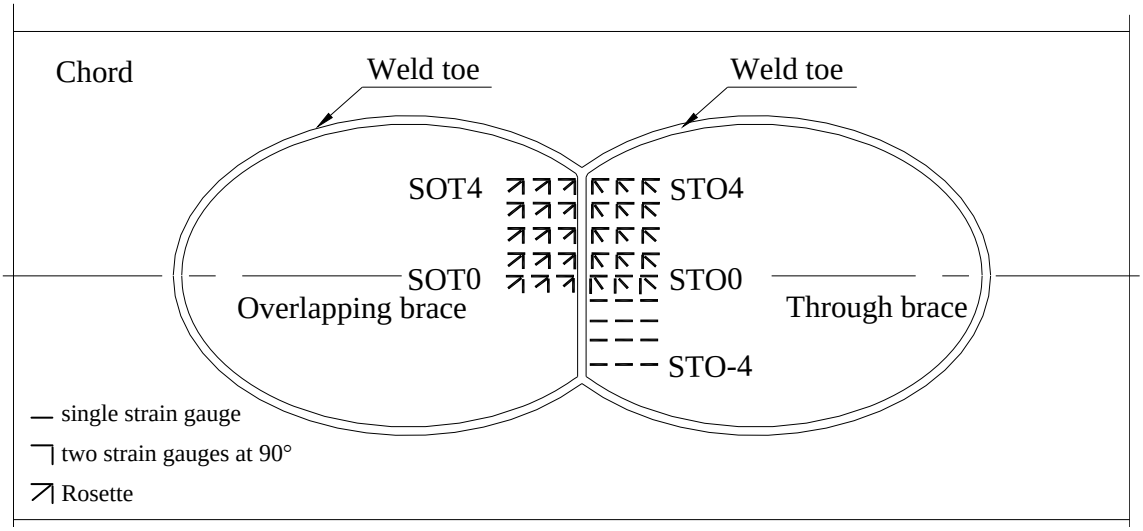

(e) Strain Gauges Locations on through and Overlapping Braces, SII

Figure 5. Strain Gauges Locations for Specimens

Table 3. Peak HSS for the Maximum Basic and Combined Cases Applied in the Test

Specimen	**Load cases**	**HSS (MPa)**	
		Chord	**Brace**
SI	AX (200kN)	20.5	20.81
	IPB (+45kN)	110.61	345.11
	IPB (-45kN)	253.60	111.19
	OPB (30kN)	89.93	127.00
	AX (200kN) + + IPB (+45kN)	178.89	364.67
	AX (200kN) + IPB (-45kN)	285.92	125.44
SII	AX (100kN)	14.75	7.87
	IPB (+12kN)	113.49	71.49
	IPB (-12kN)	116.24	72.11
	OPB (16kN)	109.58	80.10
	AX (100kN) + +IPB (+12kN)	121.9	95.44
	AX (100kN) + IPB (-12kN)	97.44	56.42

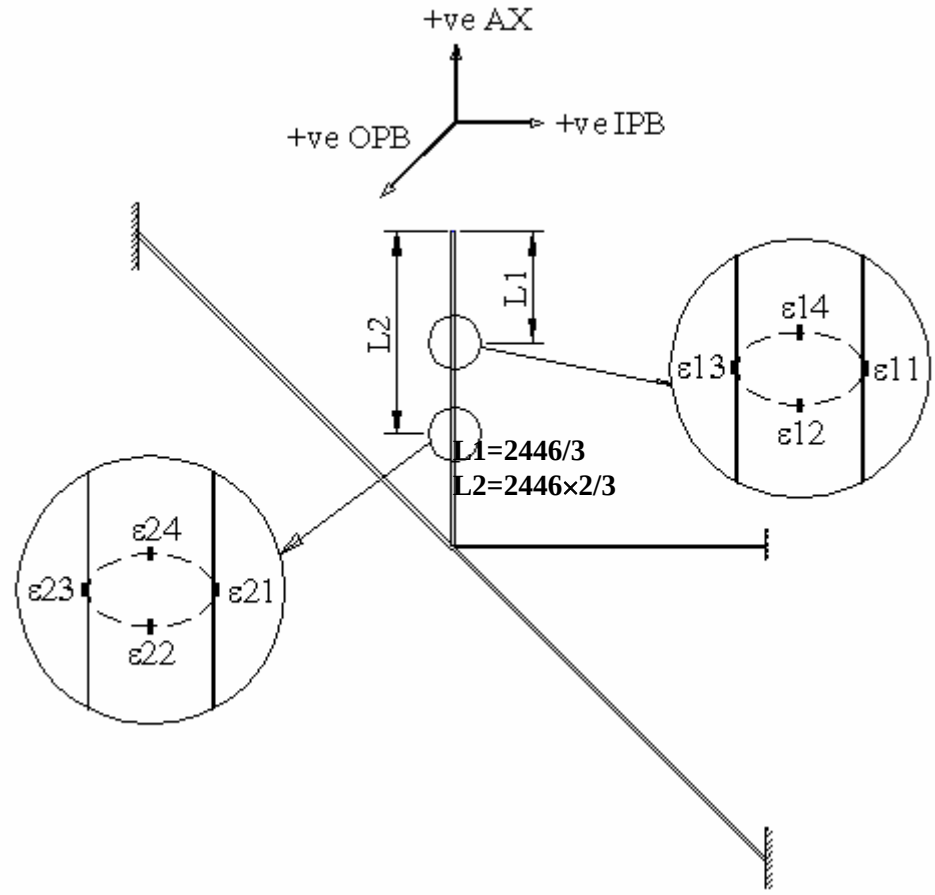

Figure 6. Eight Strain Gauges at the Midway of the through Brace

5. STATIC TEST PROCEDURE

In the static test, a series of basic loading cases and combinations of them were applied. The basic load cases were employed to obtain the SCF and the HSS distributions from the specimens and to validate the results against the published equations (Efthymiou and Durkin [1]). Prior to the actual test, the specimen was subjected to at least six loading and unloading sequences. This precaution shall test for the satisfactory performance of strain gauges and eliminated any drift of strain measurements due to the fabrication of the joints. In the actual test, each specimen was first subjected to an incremental static load on one axis, and the strains were checked against linearity and zero drift to indicate shakedown of residual stress. The eight strain gauges installed at the cross sections of the joint members were monitored by data logger to manage the applied loads in such a way that secondary loads would not be involved. The actuators were then ramped to the predetermined loads. During the static test, in order to ensure that the joint remained fully elastic, the maximum static load applied was carefully computed so that the peak HSS generated in all loading cases shall not exceed 85% of the corresponding material yield stress of the sections (Table 3). It should be mentioned that while only positive value of AX and OPB loadings were applied in the test, both positive and negative IPB loadings (Figure 3) were applied. During the tests, the actuators were ramped to the maximum load in at least six loading increments. At each step, the actuators were held in place and the strain readings were recorded. The loads were then increased to the next level and measurements were repeated. After reached the maximum load, the above steps were repeated by releasing the applied load in several increments to zero.

6. TEST RESULTS

SCF Computations

At locations where only the single strain gauge arrangement was used, the strain values measured were directly converted to the stress values by multiple them with the Young's modules and the stress-strain conversion factors (Lee et al. [17]). Quadratic extrapolation was then applied to obtain the stress at the weld toe for SCF computation. At locations where the two strain gauges arrangement was used, the corresponding *strain concentration factor* (*SNCF*) is first computed as

$$SNCF = \frac{HSSN}{SN_{nominal}} \tag{1}$$

where $SN_{nominal}$ is the nominal strain computed from the eight strain gauges readings at the center of brace sides. The SCF value is then computed using the following equation:

$$SCF = SNCF \frac{(1 + \nu\xi_{||}/\xi_{\perp})}{(1 - \nu^2)} \tag{2}$$

In Eq. 2 strains $\xi_{\perp}$ and $\xi_{||}$ are, respectively the perpendicular and the parallel strain components recorded by the strain gauges and ν=0.3 is the Poisson's ratio. Eventually, quadratic extrapolation was again employed to compute the *SCF* at the weld toe. At location where rosettes were deployed, the principal strain and stress could be directly computed and the SCF values at weld toe were then obtained by extrapolations.

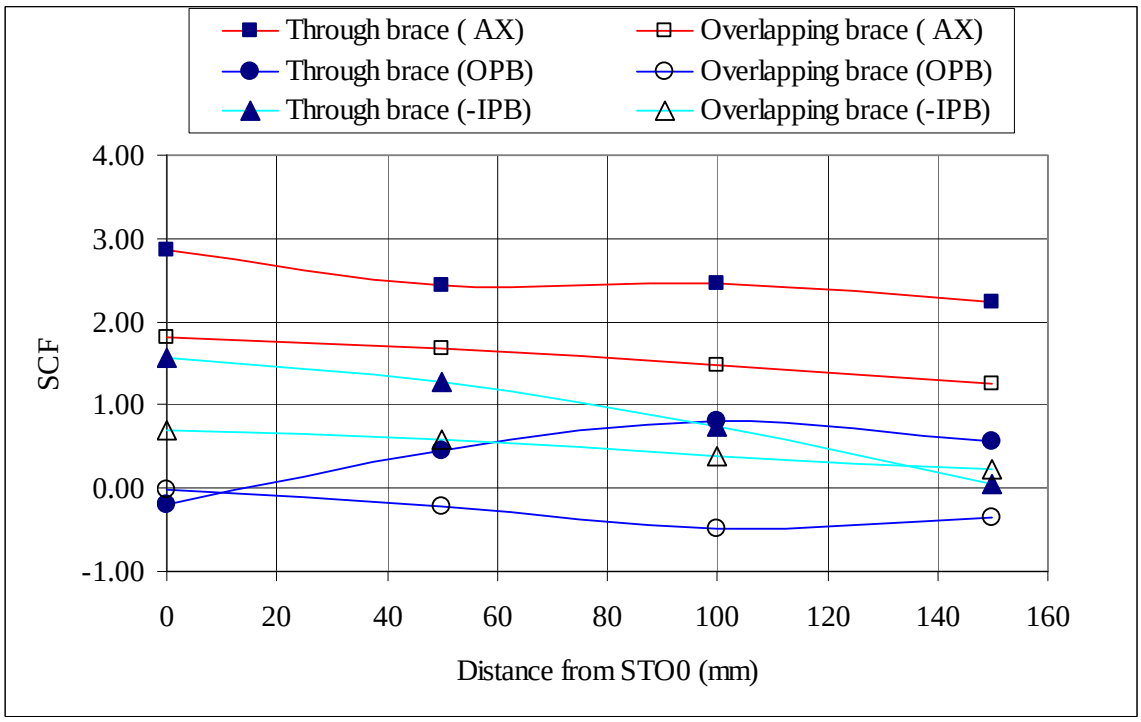

(a) Curve A

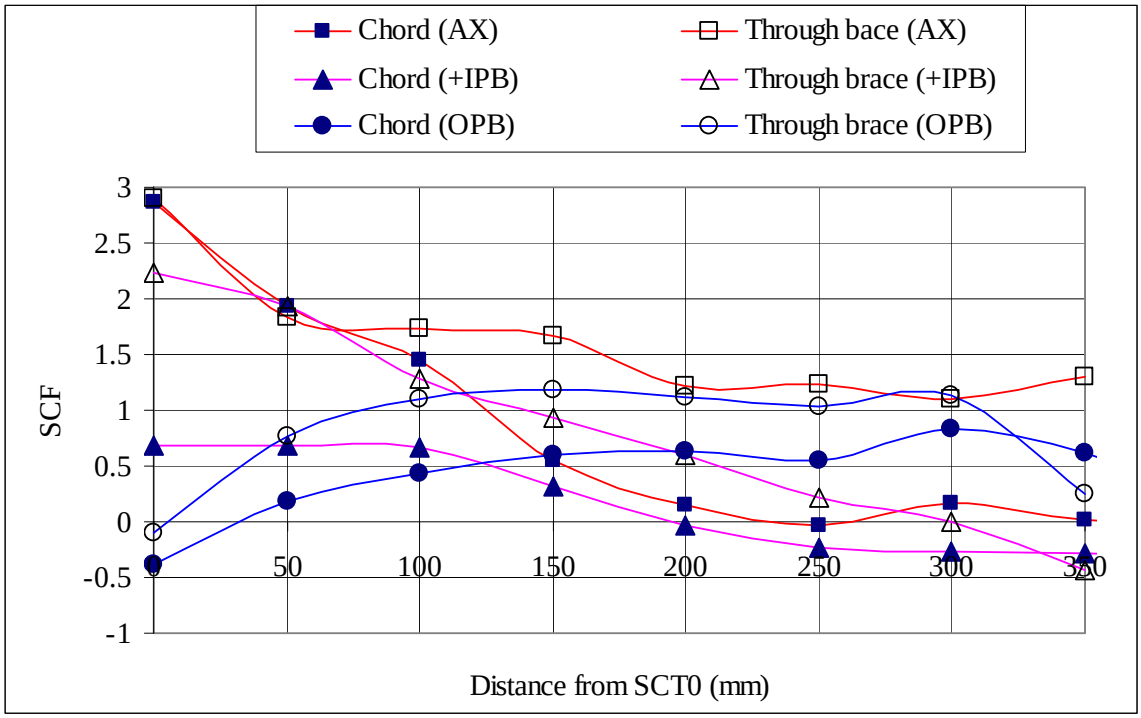

(b) Curve C

Figure 7. Variations of SCF along the Welding Curves A and C of SI

SCF Distributions

For Specimen I, it is found that critical SCF values were induced along Curve A and Curve B. In particular, a positive and a negative IPB loading induced high values of SCF along Curve C and Curve A, respectively. The SCF distributions along Curves A and C for Specimen I under different basic loading cases are shown in Figure 7(a) and 7(b), respectively. In Figure 7(a), the SCF distributions along both the through and the overlapping braces are plotted. From Figure 7(a), it can be seen that in general, the SCF distributions along the through brace are higher than that along the overlapping brace. For Curve C, as shown in Figure 7(b) for the SCF distributions along the chord and the through brace, the SCF distributions along the through brace are higher than that along the chord.

For Specimen II, similar plots for the SCF distributions are shown in Figure 8(a) and Figure 8(b) for Curve A and Curve C, respectively. From Figure 8(a), it is again observed that for Curve A under the same basic loadings, the SCF induced along the through brace are in general higher than that along the overlapping brace. However, for Curve C, it is found that the maximum SCF induced along the chord is higher than that along the through brace. Hence, it could be concluded that besides the magnitude, the *location* of maximum SCF could also be influenced by the geometrical parameters of the joint.

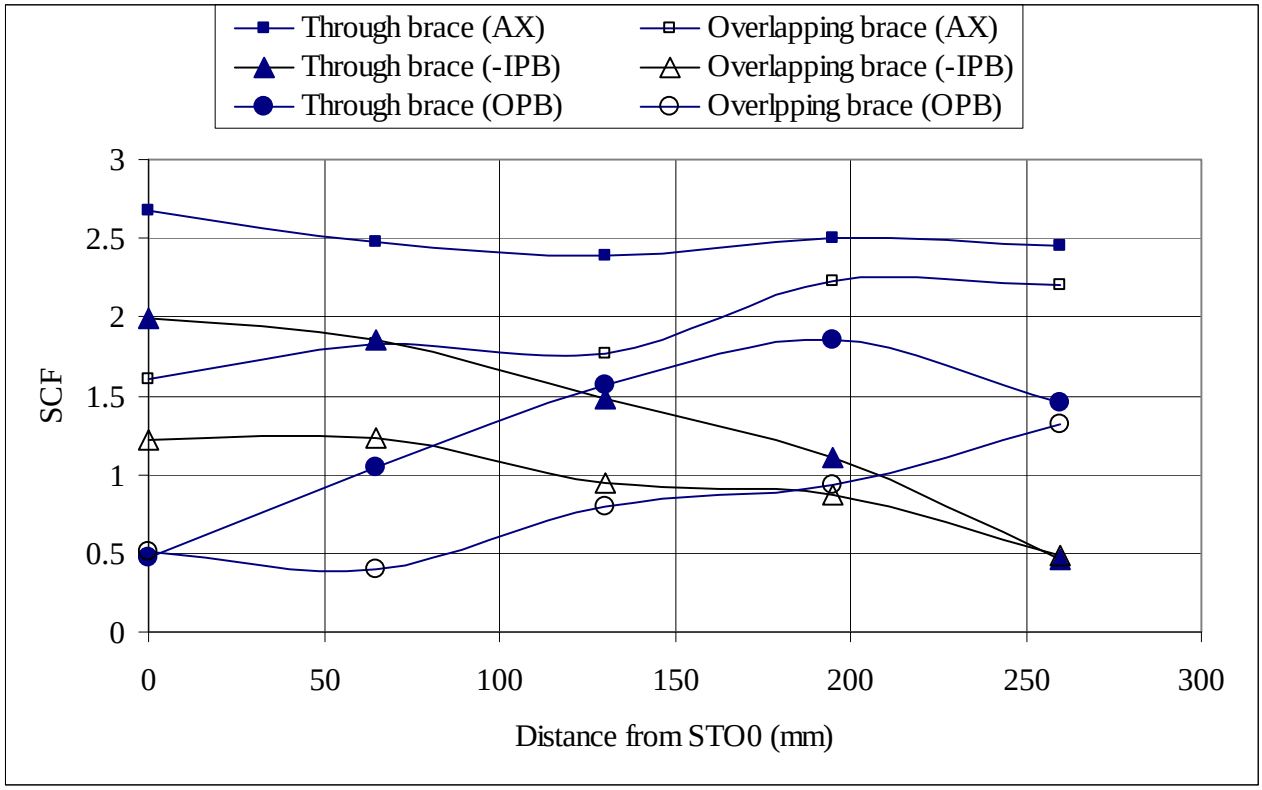

(a) Curve A

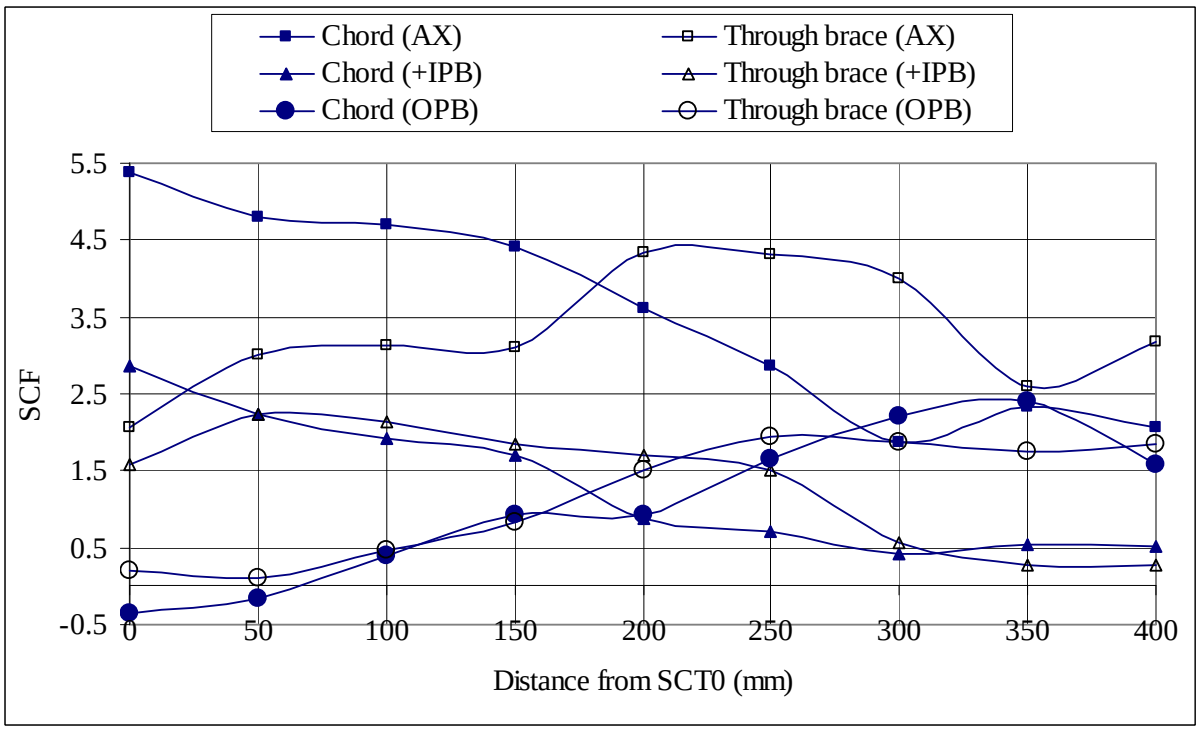

(b) Curve C

Figure 8. Variations of SCFs along the Welding Curves A and C of SII

HSS Distributions

In this study, three different approaches were employed to evaluate the HSS of the joints tested under combined loading conditions. Besides direct strain and stress measurements obtained during the experimental study, the standard superposition method (Zhao et al. [3]) was also employed to compute the HSS from the SCF values obtained from the basic load cases. When the superposition method is used, for the combined load cases, $\sigma(\boldsymbol{p})$, the stress at a given point $\boldsymbol{p}$ at the weld toe is calculated as

$$\sigma(\boldsymbol{p})=SCF_{AX}(\boldsymbol{p})\times\sigma_{n\text{-}AX} + SCF_{IPB}(\boldsymbol{p})\times\sigma_{n\text{-}IPB} + SCF_{OPB}(\boldsymbol{p})\times\sigma_{n\text{-}OPB} \quad (3)$$

where $SCF_{AX}(\boldsymbol{p})$, $SCF_{IPB}(\boldsymbol{p})$ and $SCF_{OPB}(\boldsymbol{p})$ are, respectively, the SCFs at point $\boldsymbol{p}$ for the AX, the IPB and the OPB loads. $\sigma_{n\text{-}AX}$, $\sigma_{n\text{-}IPB}$ and $\sigma_{n\text{-}OPB}$ are the corresponding nominal stresses. Finally, HSS values were also evaluated by carrying out a detailed finite element analysis using 3D solid elements model developed for fatigue performance study (Chiew et al. [18]). Figure 9 shows the 3D solid finite element meshes adopted in the numerical modelings. From Figure 9, it can be seen that high density of small elements were placed along the intersection part of the joint. Note that a similar quadratic extrapolation method was also adopted to extract the HSS values from the FE models. Hence, the HSS values obtained from numerical modeling could be directly compared with the corresponding results obtained from the experiments and the superposition method.

After some detail comparisons among all the results obtained, it is found that when the joints were subjected to combine AX and IPB loadings, peak HSS was induced along Curve C. Figure 10(a) and Figure 10(b) show the HSS distributions obtained by the three approaches along Curve C for Specimens I and II, respectively. For Specimen I, it can be seen that for all the three approaches used, HSS distributions along the *through brace* are higher than the corresponding distribution along the chord. Note that this observation is different from most results obtained in other T/Y and gapped K-joints studies in which the peak HSS location was almost all reported to be located along the chord side of the joint. For Specimen II, from Figure 10(b), it can be concluded that under the AX and IPB loading combination, the peak HSS is located along the chord side of the joint while the results obtained from all three different approaches show reasonable agreement. Hence, it can be concluded that when one would like to carry out fatigue assessment of an uncracked partially overlapped CHS K-joint, cares shall be paid on the locations of the peak HSS which could either be located along the chord side or the brace side of the joint.

Comparison with Efthymiou's Formulae

The maximum SCF values obtained from the tests under the AX and IPB load cases and the corresponding values obtained by using Efthymiou's formulae [1] along the Curve C are plotted in Figure 11 and Figure 12 for Specimens I and II, respectively. In addition, the maximum SCF values for all loading cases obtained from the test, from the FE models and from the Efthymiou's formulae are summarized in Table 4. Note that in Figures 11 and 12, the SCF values from Efthymiou's formulae were plotted as horizontal lines since the these formulae only give a single SCF value but not the distribution along the weld toe. Furthermore, since Efthymiou's formulae do not give any value for the load case of OPB, no comparison was made between the formulae and the experimental results. From Figures 11 and 12 and Table 4, it can be concluded that the Efthymiou's formulae is conservative for both specimens for the IPB loading case. However, they are not always conservative for the AX loading case (e.g. Specimen I, AX loading for both chord and brace side). Hence, the use of these formulae in practical applications may not be always able to yield conservative estimation of the fatigue life of a partially overlapped CHS K-joint.

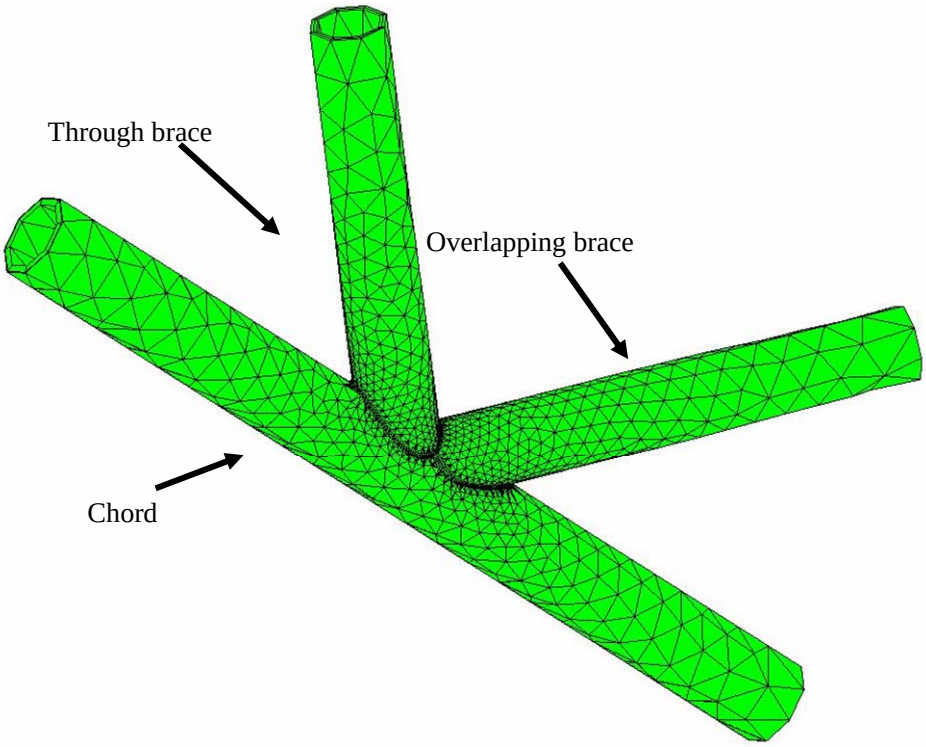

(a) Mesh for SI

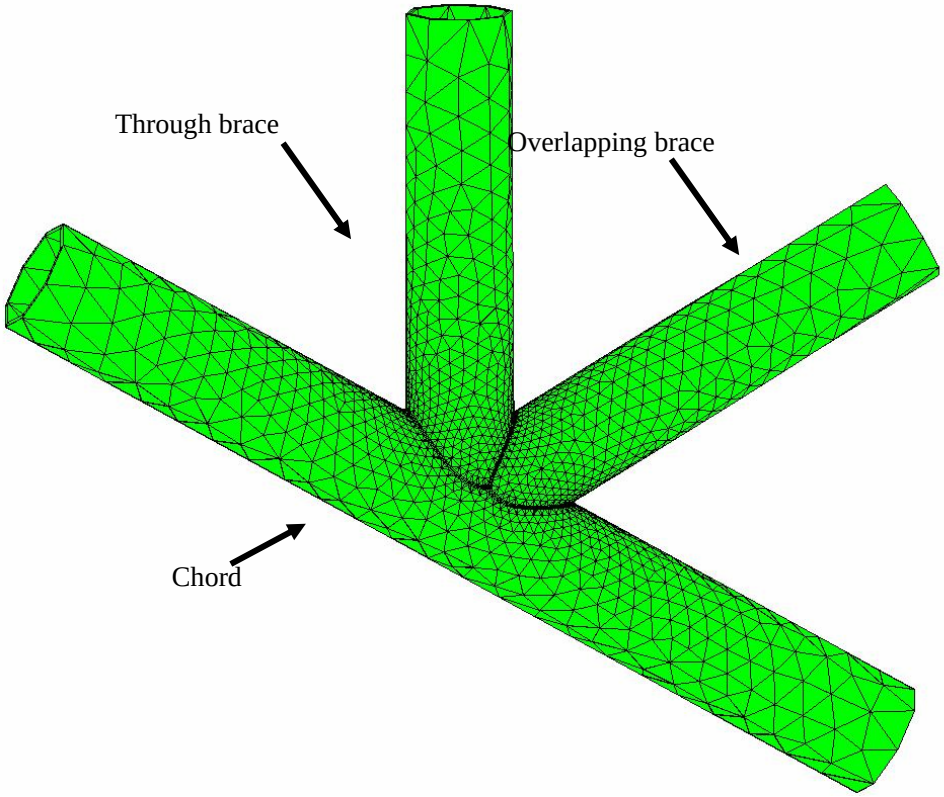

(b) Mesh for SII

Figure 9. Finite Element Meshes used in the Numerical Modeling of the Specimens

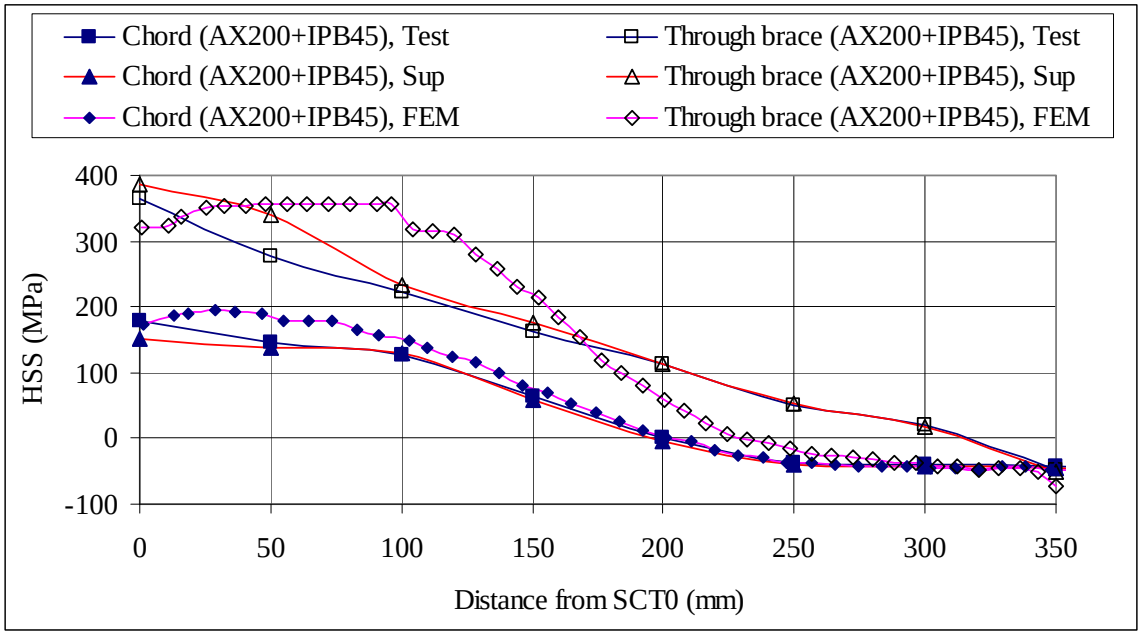

(a) Results for SI, Curve C

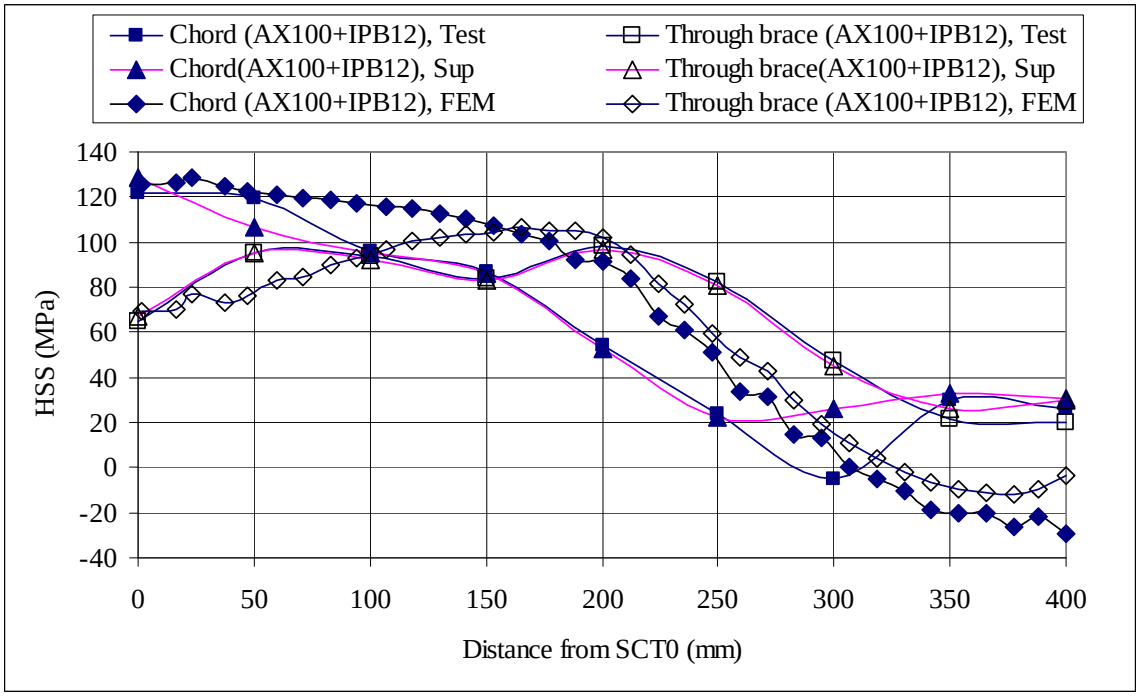

(b) Results for SII, Curve C

Figure 10. Comparison of HSS Obtained from Test, Superposition Method and FE Analyses

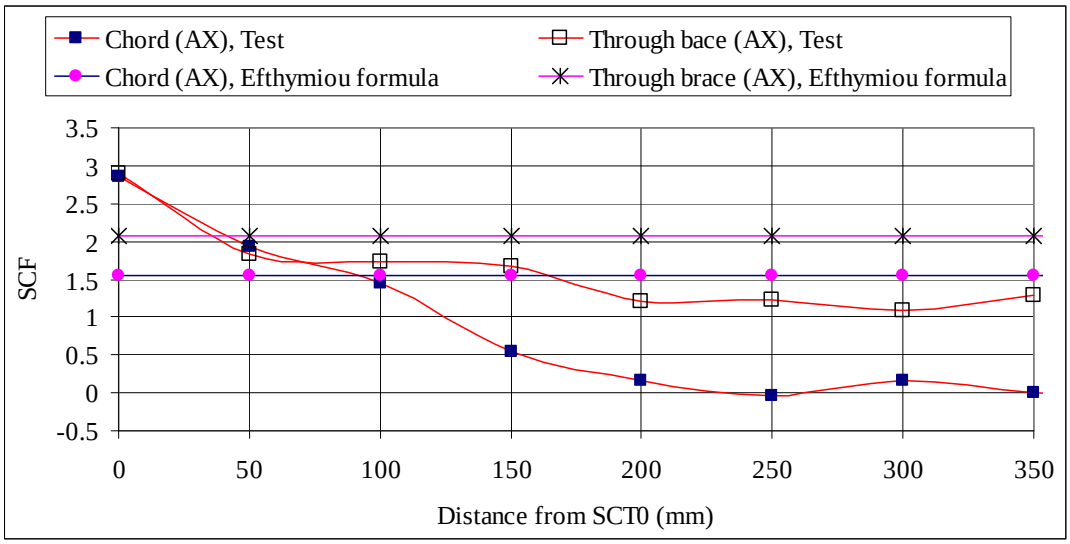

(a) Curve C, AX Loading

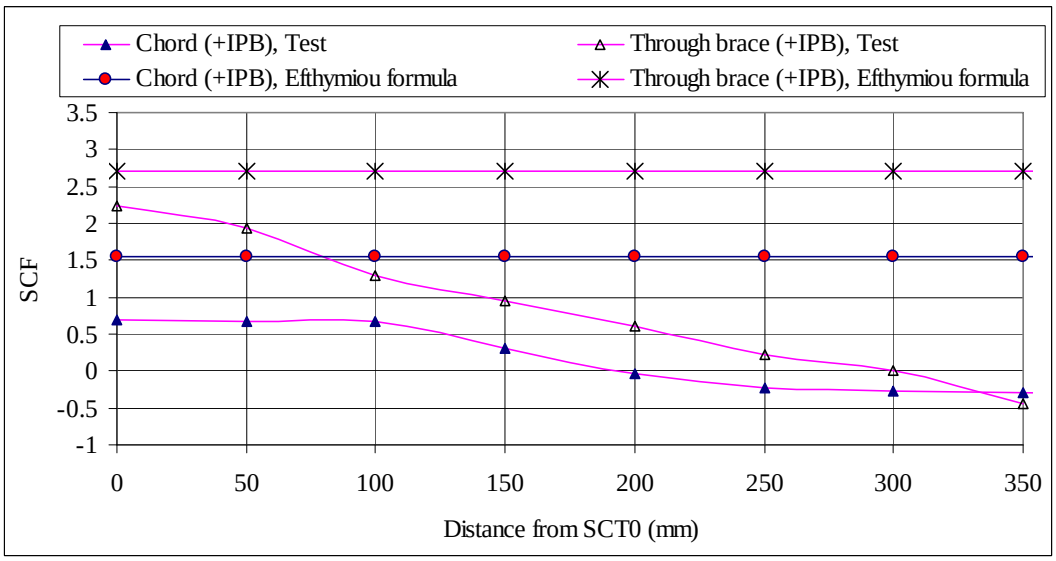

(b) Curve C, +IPB Loading

Figure 11. Comparison of SCF Variations Obtained from Test and Efthymiou's Formulae, SI.

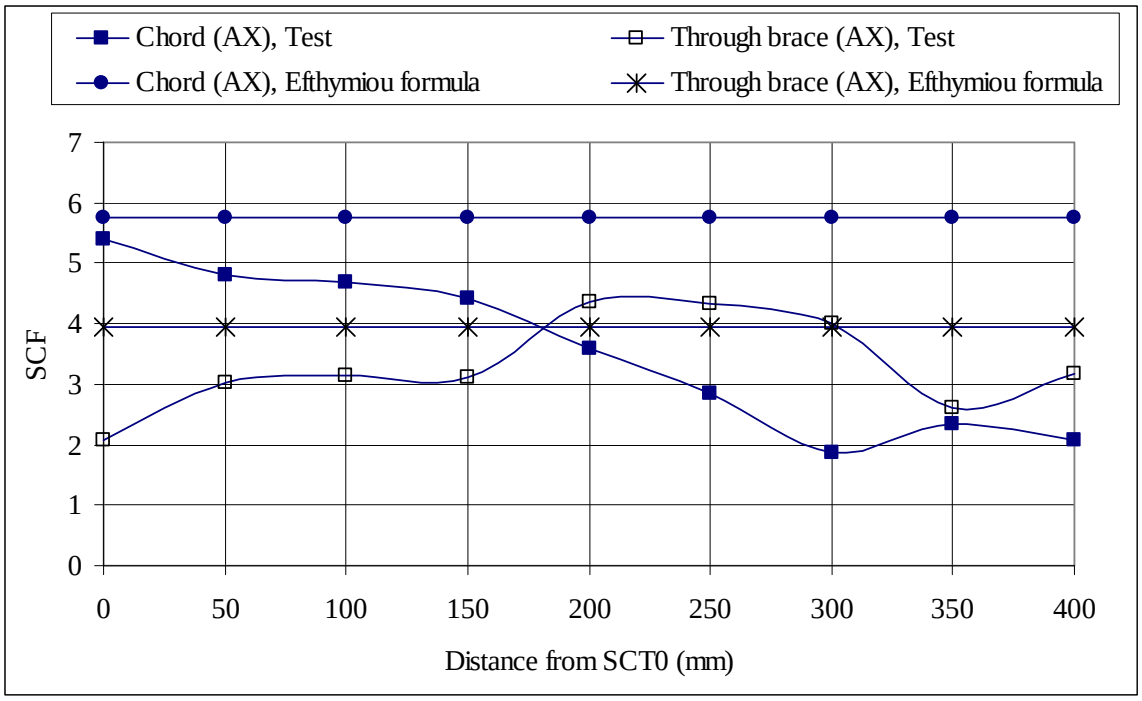

(a) Curve C, AX Loading

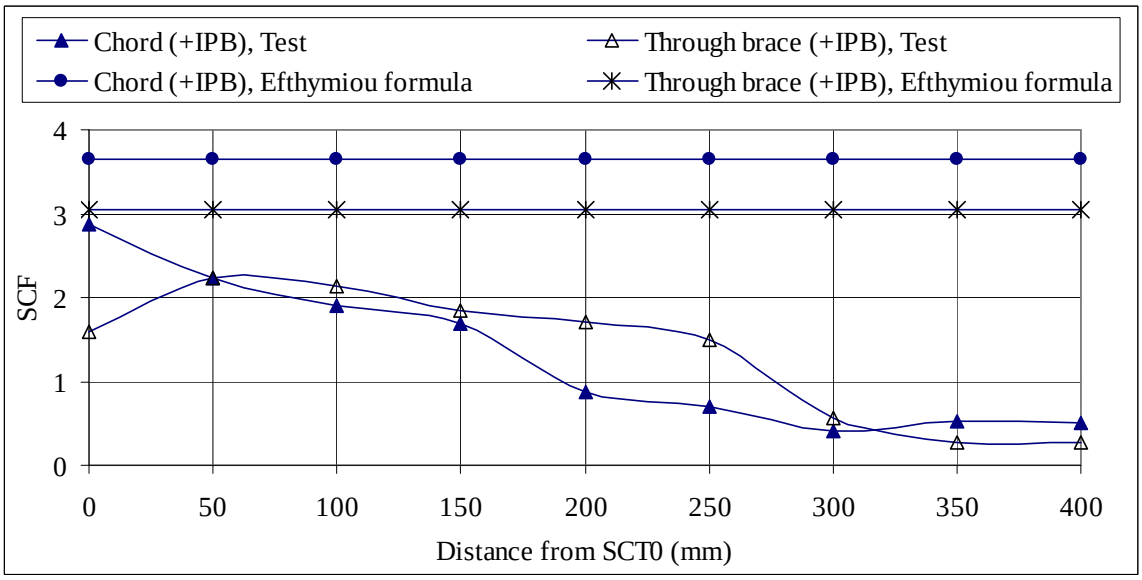

(b) Curve C, +IPB Loading

Figure 12. Comparison of SCF Variations Obtained from Test and Efthymiou's Formulae, SII

Table 4. Summary of SCF for Basic Loading Cases Obtained from Test, Efthymiou's Formulae and FE Analyses

Basic load cases	Methods	Specimen			
		SI		SII	
		Chord	Brace	Chord	Brace
AX	Test	2.86	2.9	5.38	4.32
	Efthymiou	1.55	2.08	5.75	3.94
	FEM	0.98	2.29	3.18	2.71
+IPB	Test	0.8	2.32	2.62	2.09
	Efthymiou	1.55	2.71	3.65	3.05
	FEM	1.61	2.87	3.92	3.38
-IPB	Test	1.56	0.68	1.99	1.23
	Efthymiou	-	-	-	-
	FEM	1.56	0.69	1.99	0.69
OPB	Test	0.72	0.99	2.40	1.94
	Efthymiou	-	-	-	-
	FEM	1.71	1.48	3.11	1.85

7. CONCLUSIONS

In this paper, a carefully planned experimental study was carried out to investigate the SCF and the HSS distributions along the joint intersection of two full scale partially overlapped CHS K-joints. The experimental results show that, depends on the geometrical parameters of the joint, the maximum SCF could locate on either the brace side or the chord side of the joint. This is different from the previous research findings on T-, Y and K-joints with gap in which the maximum SCF normally locates on the chord side only. In addition, the experimental results also shows that Ethymiou's formulae [1] are conservative only when the joints were subjected to IPB loading, but not for the case of AX loading. Hence, it is probably fair enough to say that the Efthymiou's formulae, which are currently the only formulae available in literature, may not be completely suitable for the design of partially overlapped CHS K-joints. Therefore, there is a need to develop a new design recommendation. Towards the end, the numerical examples given in this paper shown that reliable SCF values could be obtained from a carefully constructed FE model. Hence, further research works on both the experimental and parametric numerical studies could be conducted to obtain a more complete picture for the responses of this type of joints under different loading conditions.

NOTATIONS AND ABBREVIATIONS

L_C Length of Chord
D Outside chord diameter
d Outside brace diameter
e Eccentricity
T Chord wall thickness
t Brace wall thickness
O_V Percentage of overlapping
α Chord length parameter (2L/D)
β Brace-to-chord diameter ratio (d/D)
γ Chord radius-to-wall thickness ratio (D/2T)
θ_1 Angle between chord and through brace

θ_2	Angle between chord and overlapping brace
τ	Wall thickness ratio (t/T)
$\xi_{\perp}$	perpendicular strain component
$\xi_{\|\|}$	parallel strain component
$\sigma(\boldsymbol{p})$	stress at a given point ***p*** at the weld toe
$SN_{nominal}$	nominal strain
$SCF_{AX}(\boldsymbol{p})$	SCFs at point ***p*** for the AX load
$SCF_{IPB}(\boldsymbol{p})$	SCFs at point ***p*** for the IPB load
$SCF_{OPB}(\boldsymbol{p})$	SCFs at point ***p*** for the OPB load
$\sigma_{n\text{-}AX}$	nominal stress for the AX load
$\sigma_{n\text{-}IPB}$	nominal stress for the IPB load
$\sigma_{n\text{-}OPB}$	nominal stress for the OPB load
CHS	Circular hollow section
AX	Axial load
IPB	In-plane bending
OPB	Out-of-plane bending
HSS	Hot spot stress
SCF	Stress concentration factor
SNCF	strain concentration factor

REFERENCES

[1] Efthymiou, M. and Durkin, S., “Stress Concentrations in T/Y and Gap/Overlap K-Joints, Behavior of Offshore Structures”, Elsevier, Amsterdam, Netherlands, 1985, pp. 429-440.

[2] BOMEL, “Joint Industry Funded Program: Analytical and Experimental Investigation of the Behaviour of Tubular Frames”, Final Report, Maidenhead, UK, 1992.

[3] Zhao, X.L., Herion, S., Packer, J.A., Puthli, R., Sedlacek, G., Wardenier, J., Weynand, K., van Wingerde, A. and Yeomans, N., “Design Guide for Circular and Rectangular Hollow Section Joints under Fatigue Loading”, CIDECT Publication No. 8, TUV-Verlag, Germany, 2001.

[4] EC3, “Design of Steel Structures – Part 1.1: General Rules and Rules for Building”, ENV 1993-1-1, Eurocode 3, European Committee for Standardisation (CEN), 1992.

[5] Bouwkamp, J.G., “Research on Tubular Connections in Structural Work”, Welding Research Council Bulletin, USA, 1961.

[6] Bouwkamp, J.G., “Concept of Tubular-Joint Design”, Proceedings ASCE, Journal of Structural Division, USA, 1964.

[7] Healy, B.E. and Buitrago, J., “Extrapolation Procedures for Determining SCFs in Mid-Surface Tubular Joint Models”, Conference of Tubular Structures, 1994, Vol. VI, pp.651-659.

[8] Dexter, E.M. and Lee, M.M.K., “Static Strength of Axially Loaded Tubular K Joints. I: Behaviour”, Journal of Structural Engineering, Vol. 125, No. 2, pp. 194-201, 1999.

[9] Dexter, E.M. and Lee, M.M.K., “Static Strength of Axially Loaded Tubular K Joints. I: Ultimate Capacity”, Journal of Structural Engineering, 1999, Vol. 125, No. 2, pp. 202-210.

[10] Dexter, E.M., Lee, M.M.K. and Kirkwood, M.G., “POCHS K-Joints in Circular Hollow Sections under Axial Loading (An Investigation of the Factors Affecting the Static Strength Using Numerical Modelling), Journal of Offshore Mechanics and Artic Engineering, 1996, Vol. 118, pp. 53-61.

[11] Tizani, W.M.K., Yusurf, K.O., Davies, G. and Smith, N.K., “A Knowledge Based System to Support Joint Fabrication Decision Making at the Design Stage – Case Study for CHS Trusses”, Proceedings of the 7th International Symposium on tubular structures, Hungary, 1996, pp. 483-489.

[12] Fessler, H., Little, W.J.G. and Shellard, I.J., "Elastic Stress Due to Axial Loading of Tubular Joints with Overlap, BOSS'79, USA, 1979.
[13] Gibstein, M.B., "Stress Concentration in Tubular K-Joints with Diameter Ratio Equal to One", Steel in Marine Structures, Elsevier, Amsterdam, Netherlands, 1987, pp. 377-393.
[14] Dharmavasan, S. and Seneviratne, L.D., "Stress Analysis of POCHS K-Joints, Fatigue and Crack Growth in Offshore Structures", IMechE, 1986-2, pp. 17-30.
[15] Lee, C.K., Lie, S.T., Chiew, S.P., Sopha, T. and Nguyen, T.B.N., "An Experimental Study on the Fatigue Behaviour of Partially Overlapped CHS K-Joints", Proceeding of the 8th International Conference on Steel Space Composite Structures, Kuala Lumpur, Malaysia, 2006, pp. 273-279.
[16] American Welding Society (AWS), "Structural Welding Code-Steel, ANSI/AWS D1.1-2000", American Welding Society, Inc., Miami, 2000.
[17] Lee, C.K., Lie, S.T., Chiew, S.P. and Shao, Yongbo, "Numerical Models Verification of Cracked Tubular T, Y and K- Joints under Combined Loads", Engineering Fracture Mechanics, United States, 2005, Vol. 72, No. 7, pp 983 – 1009.
[18] Chiew, S.P., Lee, C.K., Lie, S.T., Nguyen, T.B.N. and Sopha, T., "Mesh Generation for Partially Overlapped Circular Hollow Section K-Joints under Fatigue Loadings", The 2nd International Maritime-Port Technology and Development Conference (MTEC 2007), 26-28 September 2007, Singapore.

TOTAL AND INCREMENTAL ITERATION FORCE RECOVERY PROCEDURE FOR THE NONLINEAR ANALYSIS OF FRAMED STRUCTURES

Fawu Wang [1,*] and Yaopeng Liu [2]

[1] *Department of Civil Engineering, Nanjing University of Aeronautics and Astronautics Yudao Street, Nanjing, China*
[2] *Department of Civil and Structural Engineering, The Hong Kong Polytechnic University Hunghom, Kowloon, Hong Kong*
**(Corresponding author: E-mail: fwwang@nuaa.edu.cn)*

Received: 22 May 2008; Revised: 6 August 2008; Accepted: 20 August 2008

ABSTRACT: Co-rotational formulation is suitable for the incremental-iterative nonlinear analysis of framed structure which can be divided into three stages: the predictor, corrector and error-checking phases. The corrector or force recovery procedure determines the accuracy of the solution while the predictor affects only the convergence speed and direction of iteration. This paper details the formulation of the incremental-iterative nonlinear analysis of framed structure with PEP element and reviews the present existing force recovery procedures. A new force recovery method is proposed and compared with total secant iteration method and pure incremental method. It is found through three numerical examples that this incremental iteration force recovery procedure has a convergence rate comparable to total secant iteration method and it is recommended for path-dependent analysis.

Keywords: Nonlinear analysis; framed structures; force recovery procedure; steel frame

1. INTRODUCTION

The nonlinear analysis of 3Dimensional framed structures has been extensively studied by various researchers. Geometric nonlinearity is an important nonlinear source because of the slenderness of most framed structure members. Plasticity and semi-rigid connections also play an important role for nonlinear analysis.. To obtain the nonlinear response of framed structure accurately, the incremental-iterative technique provides a unique solution under a prescribed load level. In practice the incremental and iterative solution strategy are employed to trace the load vs. deflection path of a structure.

The incremental-iterative nonlinear analysis of framed structure can be divided into three stages: the predictor, corrector and error-checking phases. The task of the predictor stage is to estimate the structural displacements under a given load increment. The corrector is concerned with recovery of the element forces for the obtaining element displacements and deformations. In the error-checking phase the unbalanced forces are computed by comparing the internal resistant forces with the applied loads. The predictor affects only the convergence and direction of iteration, while the corrector determines the accuracy of solution [1].

In this paper the recovery procedure of the element forces is investigated and three force recovery methods, namely as the total secant iteration, pure incremental and incremental secant iteration force recovery procedures are described. The advantages and limitations of these three force recovery methods are compared.

2. CO-ROTATIONAL FORMULATION

It is well known that three Lagrangian kinematic descriptions are available for the finite element analysis of geometrically nonlinear structures. Namely they are the total Lagrangian, the updated Lagrangian, and the co-rotational formulation. The reference configuration in the total Lagrangian formulation is the initial un-deformed configuration C_0, whereas in updated Lagrangian formulation is the last known deformed configuration C_1. In co-rotational formulation the motion is split into two components: rigid body motion and deformational motion. The rigid body motion is represented by a reference frame which is rigidly attached to the end of the element and continuously rotates with the element as shown in Figure 1. Consequently an important advantage of the co-rotational formulation is that the volume integrations are generally performed over the simple un-deformed shape of the element. This reference frame can be viewed as an intermediary co-rotated configuration C^R for clear physical meaning although from a mathematical standpoint the explicit presence of this co-rotated configuration between initial and deformed configuration is unnecessary. The motion can be measured between the deformed configuration and the co-rotated configuration C^R. The essence of the co-rotational formulation is that the deformational motion is relatively small so that simplified strain measurement such as engineering strain can be used to formulate the strain energy of the element. When this deformational motion is large such that more complicated strain measurements are needed, the co-rotational formulation has little advantage over the total Lagrangian formulation or the updated Lagrangian formulation.

The co-rotational formulation is especially useful in the formation for geometrically nonlinear analysis of frame structures as the reference frame of every element can be easily determined by the positions of two nodes of the element. The displacement of node **a** (**a** = 1, …, N) of the structures can be represented by a set $\mathbf{v}_a$ = s. In contract to the translational displacement $\mathbf{d}_a$ which can be represented by a vector and is always additive, the rotational displacement $\mathbf{R}_a$ does not transform as a vector when finite rotations are considered. The key operation of the co-rotational formulation is to extract the deformational components of the translations and rotations for each node when the incremental nodal displacement$\Delta\mathbf{v}_a$ is given by the predictor. The deformation extraction operation also involves the updating of element reference frame and nodal rotations. Several methods are available to deal with large rotations in different situations as listed in the next section.

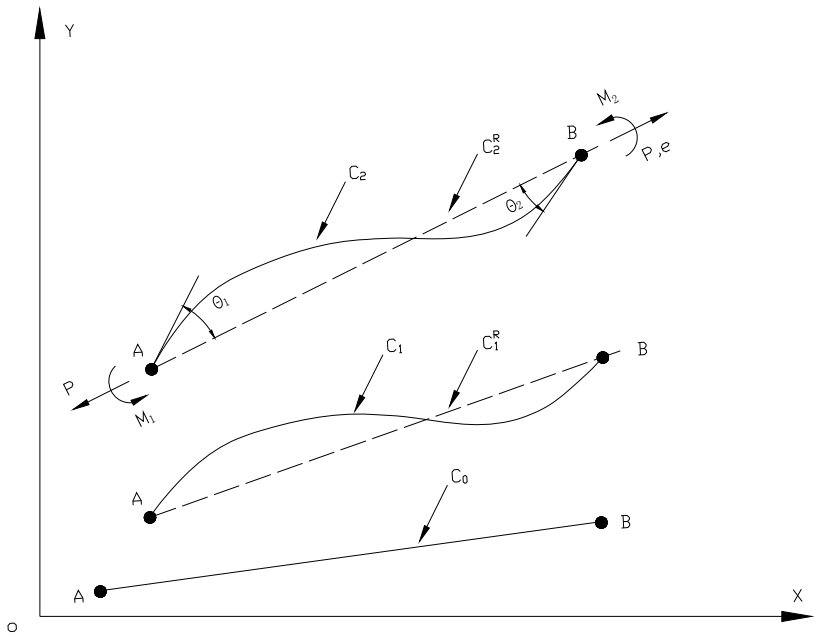

Figure 1. Co-rotational Formulation

3. LARGE ROTATION CONSIDERATION

Chan [2] compared three different methods considering large rotations and found that the joint orientation approach is a reliable formulation for genuinely large rotations in three-dimensional space while simplified methods can be used for small or moderately large rotations, which is the case of most practical engineering framed structures.

3.1 Large Rotations, Small but Finite Deformational Rotations

Strictly speaking, unit co-rotational triads which represents the directional matrix should be attached to each node and element to account for finite or large rotations. The nodal rotations $\mathbf{R}_a$ can be presented by the position of unit triads and should be updated through the incremental rotations with Rodrigues Formula. To this, several forms of rotation transformation matrix can be used. The deformational rotations can be determined by the angle of the rotation of nodal triads relative to the rigid rotation of the element. The rigid body rotation can be represented by the rotation of the element reference frame described by a set of Cartesian coordinate system where the *x* axis is chosen to pass through two end nodes of the element and *y* and *z* axes are chosen to be the principal directions of the cross section at the initial un-deformed state. This method was firstly used by Oran [3] and has been detailed by Izzuddin and Elnashai [4] and others. The mathematical deduction can refer to the paper by Felippa and Haugen [5].

3.2 Moderately Large Rotations, Small Deformational Rotations

With moderately large rotations but small deformational rotations, which is the case of most engineering structures in practice, the above method is applicable but a more concise method can be used. Instead of joint orientation triads, only the element orientation triad is used in element orientation method and the incremental local deformational displacements can be obtained through the incremental total displacements with incremental rigid body rotations eliminated. The total deformational rotations can be accumulated by every increment and so do the rigid body rotations. This approach has been used by many researchers [6-8] for its simplicity and easy implementation.

The rigid body rotations increments about local *y* and *z* axis can be obtained through the nodal incremental displacements $\mathbf{v}_l$ in local element coordinate system as,

$$\sin \Delta\Theta_z = (\Delta v_2 - \Delta v_1)/L \tag{1}$$

$$\sin \Delta\Theta_y = -(\Delta w_2 - \Delta w_1)/L \tag{2}$$

$$\Delta\Theta_x = (\Delta\alpha_2 + \Delta\alpha_1)/2 \tag{3}$$

Where *L* is the element chord length by

$$L = \sqrt{(X_E)^2 + (Y_E)^2 + (Z_E)^2} \tag{4}$$

Where X_E, Y_E, Z_E and X^0_E, Y^0_E, Z^0_E is the global coordinate difference between two nodes of the element in current and initial configuration and

$$X_E = X_E^0 + \Delta u_2 - \Delta u_1 \tag{5}$$

$$Y_E = Y_E^0 + \Delta v_2 - \Delta v_1 \tag{6}$$

$$Z_E = Z_E^0 + \Delta w_2 - \Delta w_1 \tag{7}$$

The incremental element nodal displacements $\Delta\mathbf{v}_g$ in Equation below can be obtained by a standard finite element procedure from the incremental structural nodal displacements $\Delta\mathbf{v}_a$ which is determined by an incremental-iterative predicting process. :

$$\Delta\mathbf{v}_g = \left\{\Delta u_1, \Delta v_1, \Delta w_1, \Delta\alpha_1, \Delta\beta_1, \Delta\gamma_1, \Delta u_2, \Delta v_2, \Delta w_2, \Delta\alpha_2, \Delta\beta_2, \Delta\gamma_2\right\}^T \tag{8}$$

Then the local incremental deformation $\Delta\mathbf{u}_l$ can be obtained by

$$\Delta\mathrm{u}_l = \left\{\Delta\theta_{1y}, \Delta\theta_{1z}, \Delta\theta_{1z}, \Delta\theta_{1z}, \Delta e, \Delta\theta_x\right\}^T \tag{9}$$

$$\Delta\theta_{1y} = \Delta\beta_1 - \Delta\Theta_y \tag{10}$$

$$\Delta\theta_{1z} = \Delta\gamma_1 - \Delta\Theta_z \tag{11}$$

$$\Delta\theta_{2y} = \Delta\beta_2 - \Delta\Theta_y \tag{12}$$

$$\Delta\theta_{2z} = \Delta\gamma_2 - \Delta\Theta_z \tag{13}$$

$$\Delta e = L_{i+1} - L_i \tag{14}$$

$$\Delta\theta_x = \Delta\alpha_2 - \Delta\alpha_1 \tag{15}$$

The member length L_i is calculated by

$$L_i = \sqrt{(X_E^i)^2 + (Y_E^i)^2 + (Z_E^i)^2} \tag{16}$$

It should be noted that the rigid body rotation increment is assumed to be finite and a rotation matrix is used to update the orientation of element local frame

$$
{}_rT = \begin{bmatrix}
\cos\Delta\Theta_n & \dfrac{-\cos\Delta\Theta_n \sin\Delta\Theta_y \cos\Delta\Theta_x - \sin\Delta\Theta_z \sin\Delta\Theta_x}{\cos\Delta\Theta_y} & \dfrac{\cos\Delta\Theta_n \sin\Delta\Theta_y \sin\Delta\Theta_x - \sin\Delta\Theta_z \cos\Delta\Theta_x}{\cos\Delta\Theta_y} \\
\sin\Delta\Theta_y & \cos\Delta\Theta_y \cos\Delta\Theta_x & -\cos\Delta\Theta_y \sin\Delta\Theta_x \\
\sin\Delta\Theta_z & \dfrac{-\sin\Delta\Theta_y \sin\Delta\Theta_z \cos\Delta\Theta_x + \sin\Delta\Theta_z \sin\Delta\Theta_x}{\cos\Delta\Theta_y} & \dfrac{\sin\Delta\Theta_y \sin\Delta\Theta_z \sin\Delta\Theta_x + \cos\Delta\Theta_n \cos\Delta\Theta_x}{\cos\Delta\Theta_y}
\end{bmatrix}
\tag{17}
$$

where $$\cos\Delta\Theta_n = \sqrt{1 - \sin\Delta\Theta_y \sin\Delta\Theta_y - \sin\Delta\Theta_z \sin\Delta\Theta_z} \tag{18}$$

The element orientation matrix **T** can be updated by incremental rigid body rotation in Eq. 17 such that moderately large rotation can be accounted for.

3.3 Small Rotations, Small Deformational Rotations

In this situation, the rotation can be represented by the rotational vector which is additive and the total nodal displacements can be written as,

$$\mathbf{v}_g = \{u_1, v_1, w_1, \alpha_1, \beta_1, \gamma_1, u_2, v_2, w_2, \alpha_2, \beta_2, \gamma_2\}^T \tag{19}$$

It can be updated by directly addition with the displacement increments

$$\mathbf{v}_g = \mathbf{v}_g^0 + \Delta\mathbf{v}_g \tag{20}$$

in which $\Delta\mathbf{v}_g$ is the incremental displacements obtained an incremental-iterative predictor.

The deformational rotations can be obtained directly through the total rotations eliminating the rigid body rotations. The total rigid body rotations can be cumulated by every incremental rigid body rotation through Eq. 1 to 3 or obtained directly by the total form of these equations. Then the total local deformation $\mathbf{u}_l$ can be obtained through total form of Eq. 10 to 15 in which the total global displacements and total rigid body rotation are used.

The component of the total element deformation is linked with the element internal forces in secant relationship in beam-column element and can be listed as:

$$\mathbf{u}_l = \{\theta_{1y}, \theta_{1z}, \theta_{2y}, \theta_{2z}, e, \theta_x\}^T \tag{21}$$

4. PEP ELEMENT FORMULATION REVIEWS

The PEP element proposed by Chan and Zhou [9] is derived in co-rotational formulation where only basic deformations and the corresponding basic forces are involved. Besides the compatibility conditions at the two end nodes, two additional constraints of equilibrium at the mid-span of an element are considered for the evaluation of the displacement function which is a fifth-order polynomial written as follows

$$v_n = (N_{1n}\ N_{2n})(L\theta_{1n}\ L\theta_{2n})^T \tag{22}$$

Where n = y, z is two principle direction of cross section, θ_{1n} and θ_{2n} = nodal rotations at two ends, N_{1n} and N_{2n} are shape functions which are given by

$$N_{1n} = A_n / H_{1n} + B_n / H_{2n} \tag{23}$$

$$N_{2n} = A_n / H_{1n} - B_n / H_{2n} \tag{24}$$

And

$$A_n = -20\frac{x}{L} + (80 - q_n)\left(\frac{x}{L}\right)^3 + 4q_n\left(\frac{x}{L}\right)^5 \tag{25}$$

$$B_n = 6 - (24 - \frac{q_n}{2})\left(\frac{x}{L}\right)^2 - 2q_n\left(\frac{x}{L}\right)^4 \tag{26}$$

$$q_n = PL^2/EI_n \tag{27}$$

$$H_{1n} = 80 + q_n \tag{28}$$

$$H_{2n} = 48 + q_n \tag{29}$$

The secant stiffness relationship can be formulated by the principle of stationary potential energy and is given as follows:

$$M_{1n} = \frac{EI_n}{L}\left[\left(c_{1n} + c_{2n}\right)\theta_{1n} + \left(c_{1n} - c_{2n}\right)\theta_{2n}\right] \tag{30}$$

$$M_{2n} = \frac{EI_n}{L}\left[\left(c_{1n} - c_{2n}\right)\theta_{1n} + \left(c_{1n} + c_{2n}\right)\theta_{2n}\right] \tag{31}$$

$$P = EA\left[\frac{e}{L} + \sum_{n=x,y} b_{1n}\left(\theta_{1n} + \theta_{2n}\right)^2 + b_{2n}\left(\theta_{1n} - \theta_{2n}\right)^2\right] \tag{32}$$

$$M_x = \frac{GJ + \mathrm{Pr}^2}{L}\theta_x \tag{33}$$

In which e = elongation of the element; $\mathbf{F}_l = \{M_{1y}, M_{2y}, M_{1z}, M_{2z}, P, M_x\}^T$ is local internal force vector; and E = elasticity modulus; I_n = moment of inertia; A = section area; L = length of the element; And c_{1n}, c_{2n} and b_{1n}, b_{2n} are axial force relating coefficients and can be given by

$$c_{1n} = \frac{3(80)^2 + 10(80)q_n + \frac{61}{7}q_n^2 + \frac{23}{1260}q_n^3}{H_{1n}^2} \tag{34}$$

$$c_{2n} = \frac{(48)^2 + 6(48)q_n + \frac{29}{5}q_n^2 + \frac{11}{420}q_n^3}{H_{2n}^2} \tag{35}$$

$$b_{1n} = \frac{2(80)^2 + \frac{26}{7}(80)q_n + \frac{46}{21}q_n^2 + \frac{23}{2520}q_n^3}{H_{1n}^3} \tag{36}$$

$$b_{2n} = \frac{2(48)^2 + \frac{14}{5}(48)q_n + \frac{66}{35}q_n^2 + \frac{11}{840}q_n^3}{H_{2n}^3} \tag{37}$$

It should be noted that this secant stiffness relationship can be considered as the exact solution of PEP element without rigid body rotation under the condition of small deformation.

The tangent stiffness matrix can be obtained by taking a variation of the secant stiffness with respect to the displacement degrees of freedom and the axial force due to which the second-order effect is considered. And the final expression of the incremental stiffness relationship can be written as:

$$ {}^{t}k_{ij} = \frac{\partial F_{li}^{T}}{\partial u_{lj}} + \frac{\partial F_{li}^{T}}{\partial q}\frac{\partial q}{\partial u_{lj}} \tag{38} $$

In which F_{li} and u_{li} are the six components of conjugate pair of local internal forces $\mathbf{F}_l$ and local deformation $\mathbf{u}_l$. The incremental stiffness can finally be determined by the tangent stiffness matrix as,

$$ \begin{bmatrix} \Delta M_{1y} \\ \Delta M_{2y} \\ \Delta M_{1z} \\ \Delta M_{2z} \\ \Delta P \\ \Delta M_{x} \end{bmatrix} = \frac{EI}{L} \begin{bmatrix} \zeta_y(c_{1y}+c_{2y})+\frac{G_{1y}^2}{H} & \zeta_y(c_{1y}-c_{2y})+\frac{G_{1y}G_{2y}}{H} & \frac{G_{1y}G_{1z}}{H} & \frac{G_{1y}G_{2z}}{H} & 0 & \frac{G_{1y}}{LH} \\ & \zeta_y(c_{1y}-c_{2y})+\frac{G_{2y}^2G_{2y}}{H} & \frac{G_{2y}G_{1z}}{H} & \frac{G_{2y}G_{2z}}{H} & 0 & \frac{G_{2y}}{LH} \\ & & \zeta_z(c_{1z}+c_{2z})+\frac{G_{1z}^2}{H} & \zeta_z(c_{1z}-c_{2z})+\frac{G_{1z}G_{2z}}{H} & 0 & \frac{G_{1z}}{LH} \\ & & & \zeta_z(c_{1z}+c_{2z})+\frac{G_{2z}^3}{H} & 0 & \frac{G_{2z}}{LH} \\ & & \textit{symmetrical} & & \eta & 0 \\ & & & & & \frac{1}{LH} \end{bmatrix} \tag{39} $$

in which G_{1n}, G_{2n} and H are parameters given by

$$ G_{1n} = 2b_{1n}\left(\theta_{1n}+\theta_{2n}\right) + 2b_{2n}\left(\theta_{1n}-\theta_{2n}\right) \tag{40} $$

$$ G_{2n} = 2b_{1n}\left(\theta_{1n}+\theta_{2n}\right) - 2b_{2n}\left(\theta_{1n}-\theta_{2n}\right) \tag{41} $$

$$ H = \frac{1}{\lambda^2} - \sum_{n=y,z} \frac{b'_{1n}\left(\theta_{1n}+\theta_{2n}\right)^2 + b'_{2n}\left(\theta_{1n}-\theta_{2n}\right)^2}{\zeta_n} \tag{42} $$

$$ \eta = \frac{GJ + \mathrm{Pr}^2}{EI} \tag{43} $$

where

$$ \lambda = \sqrt{\frac{AL^2}{I}} \tag{44} $$

$$ \zeta_n = \frac{I_n}{I} \tag{45} $$

5. FORCE RECOVERY PROCEDURE

When the corrector or force recovery procedure is exercised in the incremental iterative analysis, the element deformation ${}^0[u_l]$ in last configuration and the present deformation increments ${}^0[\Delta u_l]$ are extracted from the incremental displacement computed by the predictor equations through Eq. 10 to 15. The task of the force recovery procedure is to recover the element internal forces ${}^0[F_l]$ $+[\Delta F_l]$ at the current configuration. There are mainly three methods to complete this task.

5.1 Total Secant Iteration Method

Like other beam-column elements, the PEP element has explicit secant stiffness relationship. So in the corrector phase the element internal forces can be calculated directly by the secant stiffness in Eq. 30 to 32 with the present element deformation $[u_l]$ cumulated from the element deformation ${}^0[u_l]$ in last configuration and the present deformation increments ${}^0[\Delta u_l]$. It should be noted that c_{1n}, c_{2n} and b_{1n}, b_{2n} are axial force relating coefficients and is calculated based on the axial force of last iteration. Iteration must be used for more accurate results.

5.2 Force Incremental Method

The prevalent approach to calculate the element recovery forces at each incremental step in finite element method is cumulated from the force increments. In co-rotational method the displacement incrementsΔu can be decomposed into two parts: the rigid body displacementsΔu_r and the natural deformationsΔu_l. The effect of the rigid body displacementsΔu_r is to rotate the initial nodal forces from the last configuration to the present configuration without generation of internal forces. So the element force increments can be calculated by the natural deformations as,

$$\Delta f_l = k_n^e \Delta u_l \tag{46}$$

in which $\boldsymbol{k}^e_n$ is the element natural stiffness matrix. The accuracy of force increments is only used in the first order of the displacement increments so every load cycle step should be small enough to obtain a sufficiently accurate solution. The internal forces of the element can be updated by firstly adding the incremental internal nodal forces as,

$${}^{i+1}F_e = {}^iF_e + \Delta f_e \tag{47}$$

then the nodal forces from the last configuration are rotated to the present configuration through member orientation matrix.

Chan [2] proposed an incremental secant formulation based on UL formulation and Cubic element in which the same incremental stiffness is used as both the predictor and corrector. So actually it is same with this force incremental method. It is also pointed out that this incremental method is better than total secant formulation in dealing with non-vectorial rotations and has merits for use in the genuinely large rotation case.

5.3 Incremental Secant Iteration Method

The relationship between the element internal forces with the element deformations of last configuration in Eqs. 30-33 can be written in a simplified form as

$$F_l = \varphi(F_l, u_l) \tag{48}$$

Given the deformation increments ${}^{0}[\Delta u_l]$, the element internal forces cannot be calculated directly as the above functions are a set of implicit nonlinear functions of element internal forces $\mathbf{F}_l$. To solve this problem, the inverse form of the above equations can be written as

$$u_l = \psi(F_l, u_l) \tag{49}$$

These nonlinear equations can be solved readily by the Newton-Raphson procedure used in the analysis of nonlinear systems and the iterative procedure can be written as

$${}^{i}\left[\Delta F_l\right] = {}^{i}\left[\frac{\partial u_l}{\partial F_l}\right]^{-1} {}^{i}\left[\Delta u_l\right] = {}^{i}\left[\frac{\partial F_l}{\partial u_l}\right] {}^{i}\left[\Delta u_l\right] = {}^{i}[k]\,{}^{i}\left[\Delta u_l\right] \tag{50}$$

$${}^{i+1}\left[F_l\right] = {}^{i}\left[F_l\right] + {}^{i}\left[\Delta F_l\right] \tag{51}$$

$${}^{i+1}\left[\Delta u_l\right] = {}^{0}\left[u_l\right] + {}^{0}\left[\Delta u_l\right] - {}^{i}\left[u_l\right] \tag{52}$$

The iteration process of Eqs. 50-52 continues until the unbalanced deformation ${}^{i}[\Delta u_l]$ is sufficiently small. In this iteration the total deformation ${}^{i}[u_l]$ can be easily calculated by the reverse form of Eqs. 30-33. And it should be noted that the tangent matrix in Eq. 50 is simply the element tangent stiffness matrix and the incremental properties can be found from equation Eq. 51 and Eq. 52.

5.3 Comparison of Different Methods

Strictly speaking, the aforementioned force incremental method will introduce errors inevitable cause the element tangent stiffness instead of accurate secant stiffness is used to calculate recovery forces. As illustrated by Figure 2, the exact element forces that should be obtained in force recovery phase is point A but with force incremental method we can only get point B. According to our experience in numerical analysis, the stability and convergent speed of the total secant iteration method are better than that of the pure incremental iteration in the case of moderately large load step size. This is reasonable as the accuracy of force increments can only be ensured with sufficiently small step size while the secant stiffness is accurate so long as the deformation is not large and the accuracy becomes unrelated to the step size.

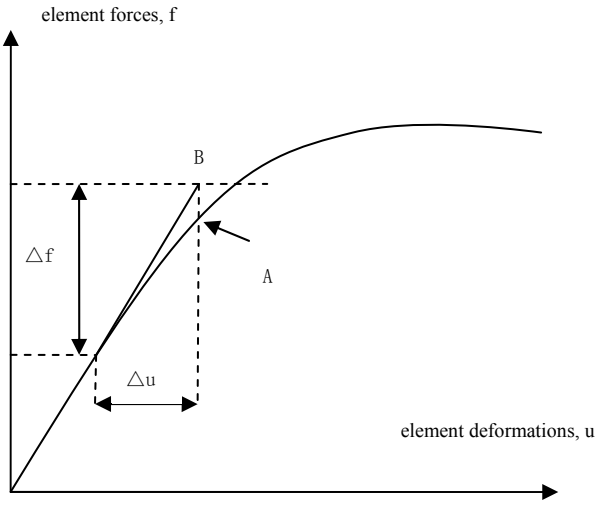

Figure 2. Illustration of Force Recovery Procedure

As far as material nonlinearity such as semi-rigid connection or plastic hinge analysis is concerned, the incremental force recovery method is more suitable as the material nonlinearity is incremental in nature. If plasticity is involved, the cross-section strength or yield state is determined by the de-composition of axial force and moments. A procedure is required to be adopted for bringing back a force point lying outside the full yield surface to this yield surface as the yield function cannot be violated with any point outside the surface is a non-defined state for the element. With ${}^{0}[F_l]$ and$[\Delta F_l]$, it can be easily concluded if the next force point is outside the full yield surface and the appropriate increment step can be adjusted to avoid a non-defined state. The total secant iteration method has better accuracy and faster convergent rate than force incremental method with moderately large step size but have defect in coping with plasticity as the force recovery procedure is not incremental. With the proposed incremental secant iteration method, the correct recovery forces are obtained and incremental manner is preserved which is crucial in the prediction of formation of plastic hinges in the solution process.

6. NUMERICAL EXAMPLES

6.1 A Simple Cantilever

A simple cantilever shown in Figure 3 is analyzed to illustrate the different convergence properties of the three force recovery methods. A horizontal compressive force is applied to the tip of the cantilever with a transverse disturbance load of 0.1%P to simulate imperfections. Only one element is used for the analysis of the cantilever.

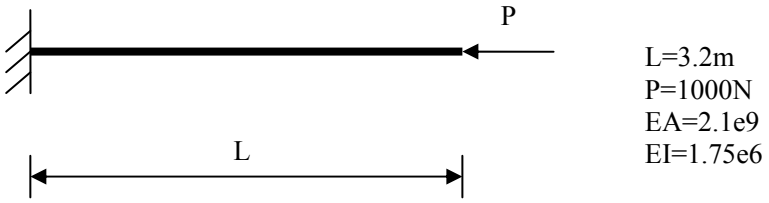

Figure 3. A Simple Cantilever

Figures 4 and 5 show the load deflection paths obtained by the three force recovery methods in conjunction with Newton-Raphson load control method and the load increments are 1 and 0.2 respectively. It can be found that the load deflection curves obtained by the total secant iteration and the incremental secant iteration methods are exactly same while the force incremental method haves apparent drift with that of the other two methods, especially when the load increments are large. And the drift occurs at mid segment of the curve where the stiffness of the structure is very small and a small load increment will lead to a large displacements. This is because the accuracy of force increments obtained by force incremental iteration method is only in the first order of the displacement increments so it is not load size but the displacements incremental size determines the accuracy of the solution. It is recommended that single displacement control or arc length control scheme be used with the force incremental iteration method. This can be confirmed in Figure 6 where very small arc length constraint needs to be specified for every step and nearly the same curves are obtained by three different recovery methods.

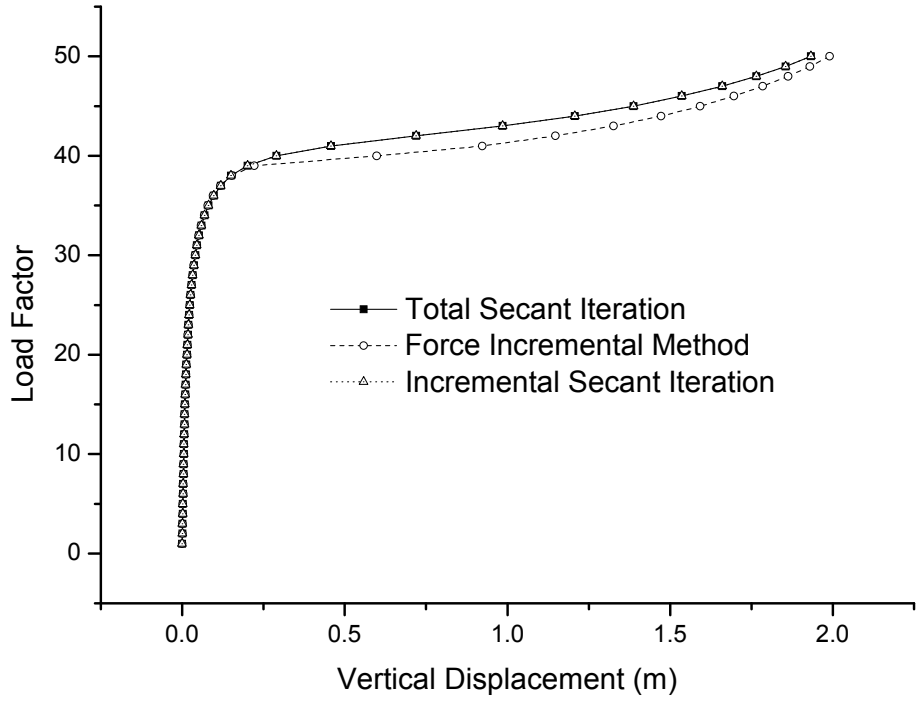

Figure 4. Load Displacement Path with Every Load Increment of 1

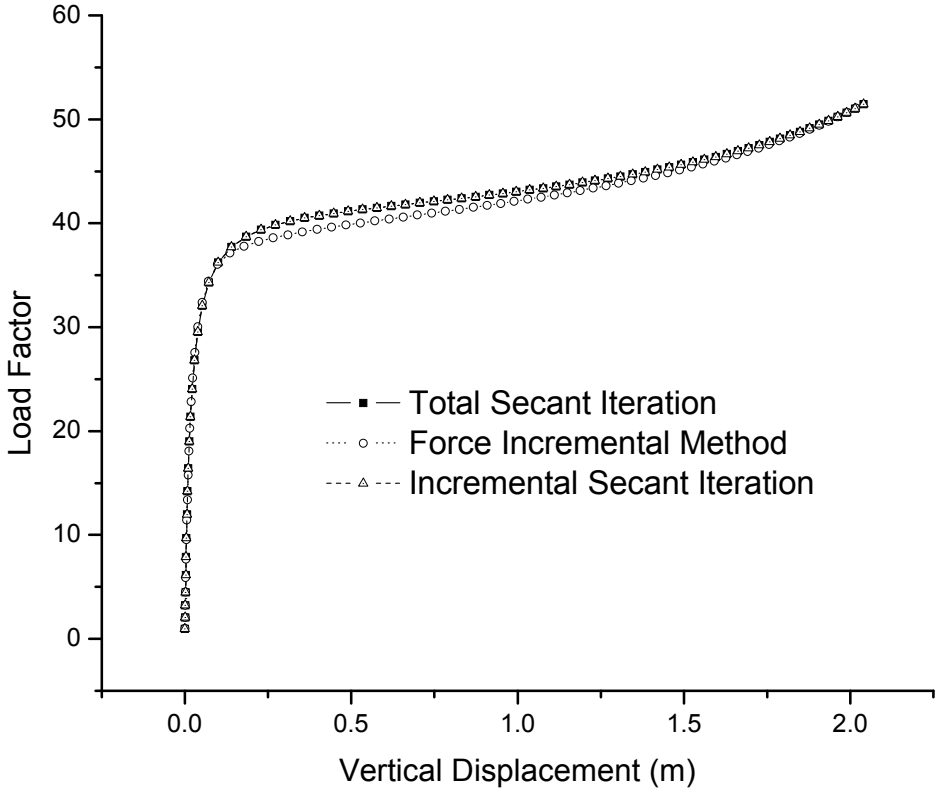

Figure 5. Load Displacement Path with Every Load Increment of 0.2

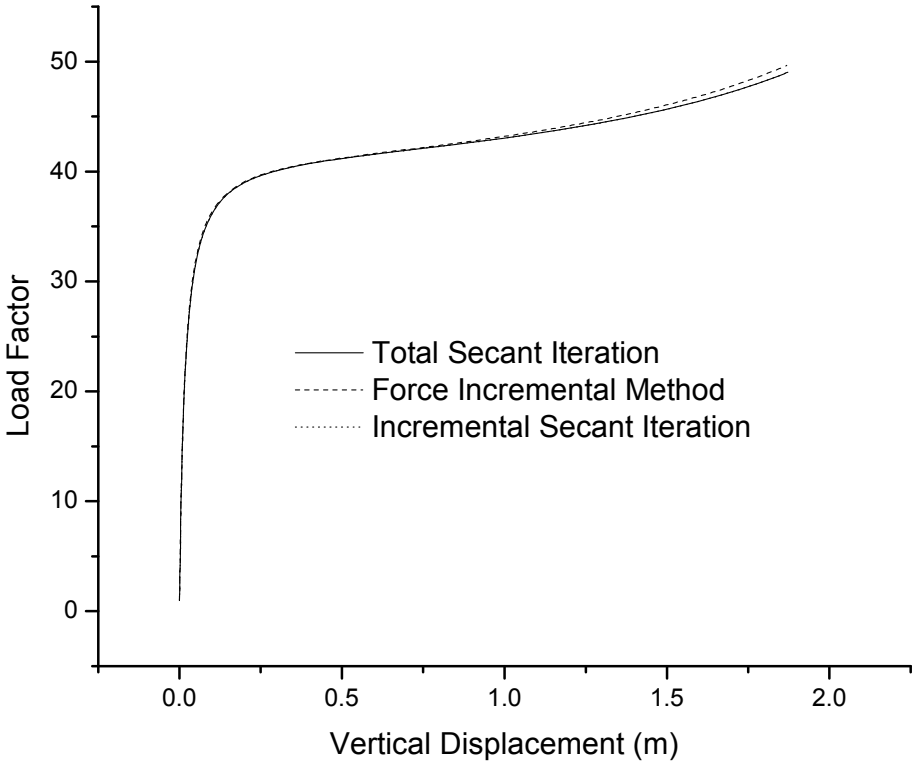

Figure 6. Load Displacement Path with Arc Length Method

6.2 William Toggle

Figure 7 shows the well-known William toggle frame which has been extensively used to investigate the snap-through buckling behavior. The Young's modulus of elasticity is 1.0×103 N/cm^2. The axial rigidity (EA) is 18550 N and the flexural rigidity (EI) is 9270Ncm^2. Only one element is used to model each inclined member and semi-rigid springs with flexural rigidity of 1/10 EI is attached to the two ends of elements. From Figure 8 it can be seen that almost same load deflection paths can be obtained by the three force recovery methods in conjunction with arc length method when the displacement is not large and there is significant differences between the force incremental method and the other two secant related methods at the latter portion of the curves where the deformations of members are large.

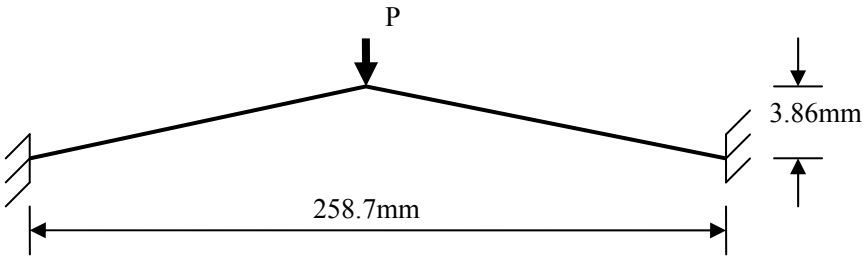

Figure 7. William Toggle

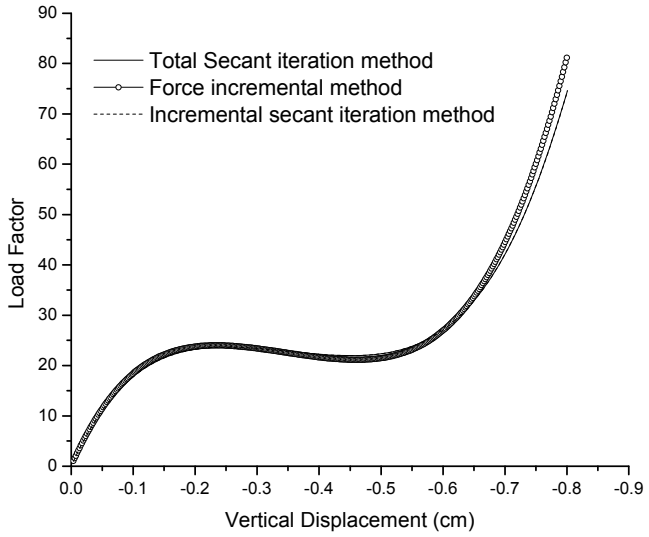

Figure 8. Load Displacement Path of Toggle Frame

6.3 90 Member 3-Dimensional Space Frame

An example of a 90-member hexagonal shallow dome with its dimensions and properties shown in Figure 9 is under a set of downward forces of 100N each acting on the non-supporting nodes. Only one single PEP element is used to model a member and member initial imperfection of magnitude equal to $1/1000^{th}$ of member length is assumed for every curved PEP element. Members of a shallow dome are typically under high axial forces because of the arch action and such an arrangement for large nodal displacement and rotation is useful to validate the performance of the proposed force recovery method.

Figures 10 and 11 show the load displacement path of vertical and lateral deflection respectively. Almost the same curves are obtained by the three force recovery methods with minimum residual displacement method in used with small step size .

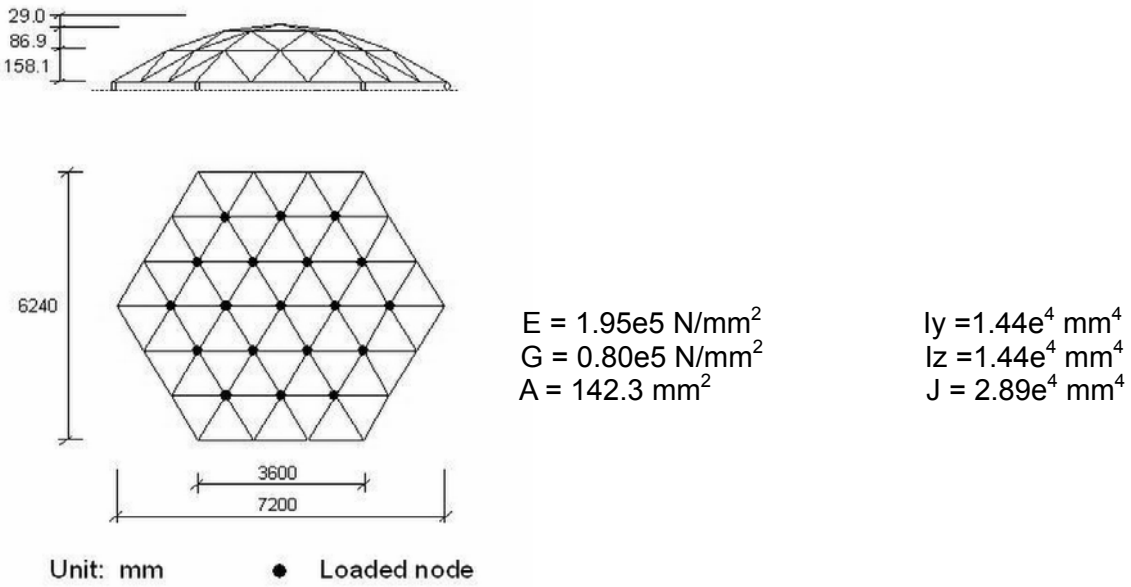

Figure 9. Hexagonal Shallow frame

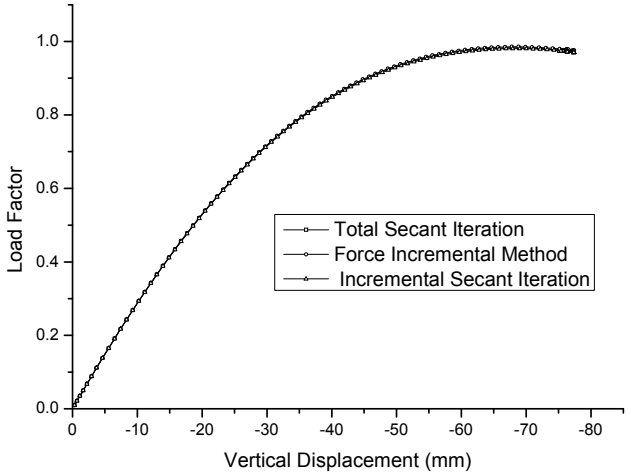

Figure 10. Load-Vertical Displacement Path of Hexagonal Shallow Frame

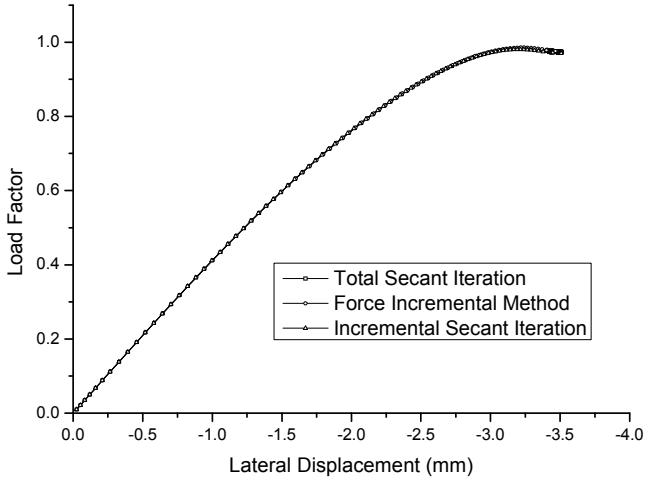

Figure 11. Load-Lateral Displacement Path of Hexagonal Shallow Frame

7. CONCLUSION

In this paper the recovery procedure of the element forces is investigated and three force recovery methods, namely as the total secant iteration, force incremental and the incremental secant iteration force recovery procedures are detailed and numerical results by these three force recovery methods are compared. It is found that the three force recovery methods can get almost the same result if we make the increments sufficiently small. And the total secant iteration and the incremental secant iteration can always get the same result irrespective of the step size used. The force incremental method has a considerable drift with that of the other two methods when the step size is large and the difference is minimized when small load/displacement step size is used. The incremental characteristic of force recovery procedure is important to forecast the formation of a plastic hinge and thus engineer should be aware of the limitation of various formulations. The proposed incremental secant iteration method can compute the internal forces in an explicit incremental manner and has the same convergence characteristics identical to the total secant iteration. The application of the proposed method in semi-rigid connection and plastic hinge analysis will be illustrated after further investigation.

REFERENCES

[1] Yang, Y.B., Lin, S.P. and Leu, L.J., "Solution Strategy and Rigid Element for Nonlinear Analysis of Elastically Structures Based on Updated Lagrangian Formulation", Engineering Structures, 2007, Vol. 29, pp. 1189-1200.

[2] Chan, S.L., "Large Deflection Kinematic Formulations for Three-Dimensional Framed Structures", Computer Methods in Applied Mechanics and Engineering, 1992, Vol. 95, pp. 17-36.

[3] Oran, C., "Tangent Stiffness in Space Frames" , 1973, Vol. 99, pp. 987-1001.

[4] Izzuddin, B.A. and Elnashai, A.S., "Eulerian Formulation for Large-Displacement Analysis of Space Frames", Journal of Engineering Mechanics, 1993, Vol. 119, pp. 549-569.

[5] Felippa, C.A. and Haugen, B., "A Unified Formulation of Small-Strain Co-Rotational Finite Elements: I. Theory", Computer Methods in Applied Mechanics and Engineering, 2005, Vol. 194, pp. 2285-335.

[6] Chan, S.L. and Kitipornchai, S., "Geometric Nonlinear Analysis of Asymmetric Thin-Walled Beam-Columns", 1987, Vol. 9, pp. 243-254.

[7] Papadrakakis, M., "Post-Buckling Analysis of Spatial Structures by Vector Iteration Methods", Computers and Structures, 1981, Vol. 14, pp. 393-403.

[8] Chin, C.K., Al-Bermani, F.G.A. and Kitipornchai, S., "Non-Linear Analysis of Thin-Walled Structures Using Plate Elements", International Journal for Numerical Methods in Engineering, 1994, Vol. 37, pp. 1697-1711.

[9] Chan, S.L. and Zhou, Z.H., "Pointwise Equilibrating Polynomial Element for Nonlinear Analysis of Frames", Journal of Structural Engineering, 1994, Vol. 120, pp. 1703-1717.